INVOLVEMENT OF THE MEDIAL COLUMN LIGAMENTS IN BIOMECHANICALLY SIMULATED ADULT ACQUIRED FLATFOOT DEFORMITY

A Thesis Presented

by

ARJUN SIVAKUMAR

Supervisor: Associate Professor John Costi

Co-Supervisors: Dr. Peter Stavrou and Mr. David Hobbs

Submitted to the College of Science and Engineering of Flinders University

in partial fulfilment of the requirements of the degree of

Bachelor of Engineering (Biomedical) (Honours) / Master of Engineering (Biomedical)

October 2017

College of Science and Engineering

Declaration

I certify that the work presented in this thesis does not contain or incorporate any material, previously submitted to an academic institution, unless specified through acknowledgement. To the best of my knowledge, this work does not contain any material previously published or written by any other individual, except where reference is made.

…….

Arjun Sivakumar

Abstract

Background: Adult acquired flatfoot deformity (AAFD) is one of the most common etiologies, estimated to affect approximately 8% of adults (aged 21 and over) in the U.S. (NPD Group for the Institute for Preventive Foot Health, National Foot Health Assessment 2012). This corresponds to approximately 19 million people (U.S. Census Bureau, 2017).

Classification systems describing the symptoms of AAFD are widely used in the clinical assessment and treatment of the condition ('Stage I – IV Flatfoot') and recognize the spring ligament as the most contributing stabilizing structure of the medial ankle during all stages of the condition, with the deltoid ligament described to only experience substantial deterioration at the end stage of the condition (Stage IV flatfoot). In spite of this, the biomechanical involvement of these ligaments as the physical deformity progresses has not been established.

Objectives: The aim of this study was to better understand the biomechanical contribution of the primary static stabilizing ligaments of the medial column (spring ligament, deltoid ligament, talocalcaneal interosseous, cuneonavicular ligaments) during the physical progression of AAFD.

Methods: 9 unmatched Fresh-frozen cadaveric feet specimens were used. The age of the specimens ranged from 44 to 84 years and the cause of death was not related to the foot. Except for the posterior tibial tendon (dynamic stabilizer), all other structures were kept intact. Small tantalum beads were carefully implanted at the attachment sites of the deltoid, talocalcaneal, navicular cuneiform and spring ligaments (superomedial calcaneonavicular and inferior calcaneonavicular).

A characteristic physical deformity anatomically similar to AAFD was progressively produced in the cadaveric feet using a novel six degree of freedom (6DOF) Hexapod Robot. This was produced under load control through applying 10 degrees of dorsiflexion, followed by a series of 5 incremental loads (100N, 230N, 460N, 690N, 920N) with the foot fully unconstrained. Left and right stereo-radiographs were taken of the foot in its unloaded state, as well as at each of the loadsteps. Radiostereometric Analysis (RSA) was then used to, digitize and track the displacement of the tantalum markers in 3D space and calculate the strain within each of the ligaments at each progressive loadstep.

Results: The strains for each of the 11 ligaments at 5 progressive loads were calculated, from which the sequence of recruitment of the ligaments could be observed at each stage through the interacting elongations and subsequent contractions of the stabilizing ligaments at progressive loads. The tibiocalcaneal portion of the deltoid ligament exhibited the highest strain at each loading condition.

Conclusion: Under the tested conditions, the biomechanical contribution of the static stabilizing of the medial column as the physical deformity progresses was evaluated. The deltoid ligament was found to experience higher strains than the other ligaments at each stage of the condition. An understanding of the contribution of the ligaments during the onset of AAFD is essential for optimizing the management of symptomatic AAFD. From this study, it is suggested that more attention be given to the deltoid ligament at all stages of AAFD.

Acknowledgements

I would like to take this opportunity to express my gratitude to everyone who supported me throughout the course of my master's project.

Firstly, I would like to thank my family and friends. My parents, Sasi and Siva, and my brother, Avi, for their continuous support, encouragement and understanding as I completed my thesis. I also extend my thanks and appreciation to my close friends: Sohrab Elahi, Shayan Jalali, Arian Motalabi and Stefan Rossi for their support and motivation. I would also like to thank Aline Kunnel for her advice in the statistical analysis of the data obtained.

I appreciate the mentorship provided by Dr Peter Slattery and his team at the Rehabilitation Engineering Centre of the Royal Brisbane and Women's Hospital in Brisbane, Queensland. Both Dr. Slattery and his team provided the initial momentum to clinical practical experience in biomedical engineering.

I thank Mr. Richard Stanley and Mr. Scott Manley for their advice and assistance in the preparation for the experiments involved in this thesis. I also extend my thanks to I also thank the radiographers at the Flinders Medical Centre, Linda Gibson, Charlotte Tyte and Susan Bui for their assistance with taking the x-rays captured as part of this thesis.

I thank Ms. Dhara Amin for sharing her knowledgeable insight into biomechanical testing & research, training me on the control of the hexapod robot as well as her assistance in taking the radiographs captured during this thesis.

I would like to thank Dr. Peter Stavrou and Dr. David Mora, for providing me with the opportunity to work on such an exciting biomedical project. Their continuous support throughout the project was paramount, and their guidance with their medical & clinical expertise was instrumental to the successful operation of the project.

Importantly, I extend my gratitude to Associate Professor John Costi and Mr. David Hobbs for their continuous support, guidance, encouragement and mentorship throughout my learning, without which, this project would not be possible. Through sharing their knowledge and expertise in the field, they have guided me in my academic, professional and personal learning. This has expanded my practical expertise, knowledge, repertoire of skills and understanding of the medical, engineering and professional fields, which I am grateful for.

TABLE OF CONTENTS

List of Figures

List of Tables

Chapter 1: Introduction

1.1 The importance of the Foot & Ankle

Mobility is one of the most important and primal functions of the human body. It is an essential part of everyday life and provides us with the freedom to independently access the world around us. From an early age, an infant's first steps are considered a remarkably significant milestone in the eyes of a parent and this ability to freely move around is exercised throughout our lives. When we think of our childhood, vibrant and exciting memories often come to mind of playful laughter and games involving running, hiding, jumping and climbing. As we age and grow more independent, this ability to utilize the strength, motor control and balance of our lower limbs becomes more of a necessity in order to fully interact with the world around us. In that sense, mobility of the lower limbs not only provides us with the ability to walk, but to also experience, learn, grow, and share experiences through actively and independently interacting with the built environment.

At the end of the lower limb, the foot and ankle comprise one of the most fascinating and complex area of human anatomy. With its anatomically dense arrangement involving an intricate network of joints, ligaments and muscles, the foot and ankle truly are extraordinary examples of complex human engineering. Through the complex collective interaction of the numerous individual structures, the foot and ankle are capable of producing extremely finely tuned movements. From rapidly transforming from a mobile adapter to a rigid adapter, supporting body weight, providing balance, transferring ground reaction forces and providing shock absorption, these precise movements of the comprising structures contribute to numerous essential functions of the foot. These functions are imperative to effective coordinated mobility of the musculoskeletal system as well as function of the human body as a whole.

As we age, our muscles and other soft tissue structures within our body deteriorate. As the foot is such an anatomically dense structure, where collective interaction of the interrelated system of bones, muscles and joints is critical for adequate function, deterioration of any anatomical structure within the foot, generally leads to a compensatory bearing on other nearby interrelated structures, thus impacting the function of the foot.

As function of the foot and ankle is decreased, this leads to further ramifications for joints above the foot and ankle as the body attempts to adequately redistribute ground reaction forces to balance the body. As this occurs, the ability to engage with our surroundings becomes more difficult. When the ability to be physically mobile is decreased or lost, this also presents a significant threat to the mental and social well-being of an individual.

1.2 Pes Planus (Flatfoot)

Pes Planus is the term used to describe the loss of the medial longitudinal arch of the foot, resulting in a flattening of the plantar surface of the foot and can either be congenital or acquired (Carr et al. 2016).

Congenital Pes Planus is quite common amongst infants and small children and is considered a physiological deformity at young ages due to the laxity of the developing ligaments and lack of neuromuscular control (Raj & Bhimji 2017). In most cases, this condition in children is resolved as the body grows and a normal arch develops (Halabchi et al. 2013).

In contrast to this, Acquired Pes Planus or *Adult Acquired Flatfoot Deformity* is a progressive flattening of the arch of the foot. This is most commonly secondary to dysfunction of the posterior tibial tendon, however can also occur as a result of injury to the ligaments of the foot, or mechanical overuse, such as in people who participate in repetitive high impact sports, such as running and basketball (Raj & Bhimji 2017).

1.3 Adult Acquired Flatfoot Deformity (AAFD)

Adult Acquired Flatfoot Deformity (AAFD) is a symptomatic, progressive deformity currently defined by the *American Orthopedic Foot and Ankle Society* as "A progressive flattening of the arch of the foot that occurs as the Posterior Tibial Tendon becomes insufficient" (American Orthopaedic Foot & Ankle Society, n.d.). It exists as one of the most common etiologies and affects approximately 19 million adults, aged 21 and over in the U.S. (NPD Group: National Foot Health Assessment 2012) (US Census Bureau 2017).

The posterior tibial tendon (PTT), is an important stabilizer of the medial longitudinal arch of the foot during dynamic movement (dynamic stabilizer) and acts under tension within the body to invert the hindfoot, thus locking the transverse tarsal joints (Figure 1), preventing

collapse of the medial arch (Trnka 2004). This allows the calf muscle (gastrocnemius) to act most efficiently provide balance and movement during gait (Kohls-Gatzoulis et al. 2004).

[Figure has been removed due to copyright restrictions]

Figure 1: Bones of the Foot

Although AAFD was originally described as 'posterior tibial dysfunction' (PTTD), the progressive condition is now recognized to involve numerous other structures and can also be caused by injuries to the ligaments in the foot that the joints falling out of alignment (Raj & Bhimji 2017). Of these structures, the static stabilizers of the medial column recognized to undergo attenuation during AAFD most commonly include the spring ligament in early stages of the condition, and the deltoid ligament as the condition progresses further (Smyth et al, 2017). Other ligaments of the medial column contributing to arch stability, which have been described to experience deterioration during the progression of AAFD include the talocalcaneal interosseous and cuneonavicular ligaments.

1.4 Clinical Relevance

Despite extensive research over the past 30 years, the classification system most commonly relied upon in the clinical assessment and treatment of AAFD, was proposed by Johnson & Strom in 1989 and assumed that the level of deformity is based purely on the extent of rupture/function of the posterior tibial tendon (Yeap et al. 2001; Richie 2007). A major limitation of these systems is that it fails to include all other anatomic aspects of AAFD by "missing the importance of the spring ligament, deltoid ligament, naviculocuneform joint and tarsometatarsal joints" all of which have been shown to be involved (Abousayed et al. 2016).

With various clinical findings, questions have been raised regarding the contribution of the static stabilizers of the medial ankle to AAFD. Although the stabilizing ligaments of the medial column involved in AAFD are known, the sequence of involvement of these structures

causing the arch to progressively collapse remains unclear (Abousayed et al. 2016; Van Gestel et al. 2015; Neville et al. 2010).

1.5 Research Objective

The objective of this dissertation was to investigate the 'sequential recruitment patterns of the medial column ligaments during simulation of Adult Acquired Flatfoot Deformity'.

To elicit the data required to address this objective, the first component of the project was to design and develop the methods and experimental system to allow the strain of the primary medial column ligaments to be simultaneously measured as physical characteristics of an anatomic adult acquired flatfoot deformity (i.e. collapse of the longitudinal arch, valgus of the hindfoot, abduction of the forefoot were progressively simulated.

Following this, the second component of the project was to implement the developed system and protocols to address the objective of the dissertation.
This is outlined in more detail in Chapter 2, Project Aims and Rationale.

Chapter 2: Project Aims and Rationale

The objective of this dissertation was to investigate the 'sequential recruitment patterns of the medial column ligaments during simulation of Adult Acquired Flatfoot Deformity'. To achieve this, the first broad aim was to develop a method to progressively simulate the physical characteristics of an anatomic adult flatfoot deformity in cadaveric models using a novel six degree of freedom (6DOF) hexapod robot. The second broad aim was to investigate the strain recruitment patterns of the primary medial support ligaments by measuring strain as the deformity progresses.

A method utilizing Radiostereometric Analysis (RSA) was used to calculate the displacement and strains of the ankle's medial column ligaments in three dimensional space. The simulation of the physical characteristics of an anatomical AAFD in intact cadaveric models will allow for the further understanding of foot and ankle biomechanics and AAFD with possible insights into the effectiveness of current clinical assessment and treatments of the deformity.

2.1 Project Aims and Objectives

The specific aims of this Masters project include:

1. Design and validation of a Radiosterometric calibration cage system, to allow the position of the ligaments of the medial ankle to be monitored while simulating simple movements of the foot and ankle.
2. Develop a hexapod robot control protocol to progressively simulate the physical characteristics of an anatomic adult acquired flatfoot deformity (AAFD).
3. Conduct pilot testing using a sawbone model to investigate the feasibility of simulating the physical characteristics of AAFD using a 6DOF hexapod robot.
4. Develop and validate protocols for measuring ligament strains using the RSA technique combined with testing in cadaveric human feet.
5. Conduct the primary experimental testing on cadaveric human feet using the developed protocols.

6. Implement Radiostereometric Analysis to calculate the displacement and strain of the medial column ligaments in three dimensional spaces during progression of the deformity.
7. Calculate strain within the medial column ligaments during progression of the deformity.
8. Investigate the association between the strain responses of the medial column ligaments with the progression of the physical deformity.

Chapter 3: Literature Review

3.1 Mobility

Mobility is one of the most important functions of the human body as without it, we wouldn't be able to freely move our body around space. Walking is one of the most primal movements of the human body which is both beneficial to our health and an essential activity. As we walk, almost all of our tissues and muscles are recruited to produce movement, including the intestinal tract, where regulating bowel movements are vital for optimum health of the digestive system (Knight 2015). Additionally, our metabolism is stimulated as we walk, burning calories as well as promoting the body's ability to absorb nutrients and water. As the various muscles in our body are repeatedly contracting, producing the required propulsion, more blood and oxygen is circulated throughout the body. This also increases the production of lymphatic fluids, which is of paramount importance for the immune system, as it is the body's first line of defense against disease (Liao & Padera 2013). Furthermore, as the feet we walk on are bearing the body's weight, regular walking allows for the maintenance and development of the bones in the lower limb (Woolston 2017). In addition, as bones are loaded through weight bearing, Wolff's law (Wolff 1986), theorizes that repetitive loading of bone will cause adaptive responses enabling the bone to better cope with these loads (Teichtahl et al. 2015). As the bones in the foot are repeatedly loaded during walking, the natural bone remodeling process is optimized to increase bone density in areas where the bones are loaded (Frost 1994; Shanb & Youssef 2014). This thus strengthens the bones within the foot, which is essential for the prevention of conditions such as osteoporosis (Denise et al. 2014).

3.2 Anatomy of the Foot and Ankle Complex

The 'ankle joint' (Figure 2) is a hinged synovial joint, comprised of the tibia and talus, with the distal portion of the fibula articulating with the lateral side of the talus (Hodler et al. 2017; Brockett & Chapman 2016).

[Figure has been removed due to copyright restrictions]

Figure 2: Talocrural Joint of the Ankle

This joint provides plantarflexion and dorsiflexion. The foot also consists of a subtalar joint, which is located within the inter-tarsal group, between the talus and the calcaneus. This is the joint which allows for inversion and eversion of the ankle. Due to the mobility of the joints of the foot, many stabilizing ligaments are required to provide strong stability of the constituent bones within the system of the foot (Hodler et al. 2017).

The foot and ankle are relatively complex anatomical structures, consisting of 28 bones, 33 joints, and 112 ligaments, which are controlled by 13 extrinsic and 21 intrinsic muscles (Houglum & Bertoli 2012; Fraser et al. 2016).

These numerous structures comprising the foot and ankle (Figure 3) collectively work together to allow the ankle to provide several important functions, such as adequately supporting body weight, providing balance, transferring ground reaction forces, providing shock absorption and compensating for any proximal malalignment of the structures and joints above the foot (Houglum & Bertoli 2012).

[Figure has been removed due to copyright restrictions]

Figure 3: Talocrural Joint of the Ankle

The ankle is anatomically subdivided into the rearfoot, midfoot and forefoot, which provide the foot with the capacity to rapidly transform from a flexible mobile adapter to a rigid adapter when required in order to most effectively generate movement (Jarvis 2014). This is essential to efficiently allow for propulsion of the body during the normal physiological gait cycle (Aquino & Payne 2001), particularly during the stance phase of gait, which entails weight bearing and propulsion of the body (Novacheck 1998).

3.3 Gait Cycle

The gait cycle of human movement (Figure 4) consists of two phases, the stance and the swing phase (Bonnefoy-Mazure & Armand 2015). The stance phase describes the movement of the lower limb as the foot is in contact with the ground, generating propulsion, while the swing phase describes the motion of the lower limb without ground contact (foot leaving the ground, swinging forward and decelerating prior to heel contact with the ground) (Bonnefoy-Mazure & Armand 2015; Marasovič et al. 2009).

[Figure has been removed due to copyright restrictions]

Figure 4: Gait Cycle: Stance and Swing Phase

3.3.1 Stance Phase: Support & Propulsion

As depicted in Figure 5 the stance phase of the gait cycle is broken into 3 stages - the 1st, 2nd and 3rd rocker.

[Figure has been removed due to copyright restrictions]

Figure 5: The Three Rockers of Stance Phase

The 1st rocker begins when the heel makes contact with the ground(Bonnefoy-Mazure & Armand 2015). At this point, a ground reaction force pushing up on the heel is generated (Marasovič et al. 2009), which causes the ankle to plantarflex, as well as change from slightly supinated to pronated (Refer to Figures 6 & 7 below). This allows the foot to become flexible, adapt to the shape of the ground and absorb the impact of the step.

[Figure has been removed due to copyright restrictions]

Figure 6: Dorsiflexion and Plantarflexion

[Figure has been removed due to copyright restrictions]

Figure 7: Pronation and Supination of the Foot

As the forefoot makes contact with the ground, the 2nd rocker begins (Bonnefoy-Mazure & Armand 2015). In this stage, the tibia continues to move forward, causing the ankle to dorsiflex (Perry 2002), as illustrated in figure 6. As this occurs, the hip naturally begins to internally rotate, which causes the foot to externally rotate. This results in the foot changing from a pronated position, to a supinated position, allowing the foot to act as a flexed rigid lever (Bonnefoy-Mazure & Armand 2015).

The ankle continues to dorsiflex until a maximum range of motion is reached at approximately 10 degrees. At this point, the heel begins to lift from the ground with the forefoot still in contact, resulting in dorsiflexion of the metatarsal joints of the foot (Perry 2002). This stage describes the 3rd rocker of the stance phase of gait and involves extension of the knee and internal rotation of the hip to allow for an increase length of stride on the opposite leg. As the metatarsal joints are dorsiflexed, the plantar fascia is tightly recruited through a dynamic mechanical interaction of the structures within the foot and ankle known as the windlass mechanism (Bolgla & Malone 2004). This tightening of the plantar fascia flexes the arch of the foot, bringing the foot into supination, allowing stability of the foot as the foot begins to 'toe off'(Bonnefoy-Mazure & Armand 2015).

As there are minor anatomical and physiological differences that occur across every individual, the constituent structures of the leg and foot, such as the bones, tightness (or laxity) of the ligaments, and the relative strengths of antagonistic muscle groups within the foot, all work to produce a 'posture' (height and shape of the medial longitudinal arch) which is unique to each individual (Kreighbaum & Barthels 1981).

In spite of this, sufficient mobility of the ankle is essential in order for the foot to move into all the positions of the gait cycle effectively, whilst maintaining adequate mobility and stability (Novacheck 1998; Bonnefoy-Mazure & Armand 2015). Too great of a mobility reduces the stability of the foot. Due to the ankle being such an anatomically dense, complex structure, where the comprising anatomical components activate collectively to maintain stability and proper function of the foot, degradation of primary support structures within the foot has

further ramifications for other associated structures within the ankle (Chinn & Hertel 2010). In addition, as the foot and ankle play a vital role in compensating for proximal alignment, inadequate function of the foot through deterioration of the anatomical structures generally leads to incorrect alignment of the foot (Rao et al. 2013). This resultantly leads to the proximal joints being affected in order to compensate for this malalignment (Kulig et al. 2011; Rao et al. 2013)

3.4 Ligaments

Ligaments are parallel-fibred collagenous tissues, consisting of elastin and collagen fibers. These structures attach one articulating bone to another, across a joint, providing resistive forces and hence stability to the joints by restricting excessive movement (Brockett & Chapman 2016). These soft tissue structures are viscoelastic materials, meaning their mechanical behaviors are time dependent, where the stress within the material is strain rate dependent. When these tissues are stressed beyond their 'normal range', which can occur through trauma, excessive strain or mechanical overuse over time (cyclic loading) damage can occur to these ligaments. (Robi et al. 2013). As the structures within the foot are interdependent on one another, damage to one structure can also impact neighboring structures, impacting the form and function of the foot (Rao et al. 2013).

3.5 Ligaments in the Foot

In the foot, ligaments are responsible for holding the tendons in place, as well as stabilizing the joints. This allows the medial longitudinal arch of the foot to curve and flatten, providing the optimum balance of mobility and stability, therefore providing the foot with the strength to propel the body by stretching and contracting (Gillen 2014; Bonnefoy-Mazure & Armand 2015).

3.5.1 Structures of the Medial Longitudinal Arch

The shape and height of the medial arch of the foot (Figure 8) varies from individual to individual, however, due to the high number of components it contains (Table 1), it is a highly resilient structure (Scott & Winter 1993; Ren et al. 2008).

[Figure has been removed due to copyright restrictions]

Figure 8: Medial Longitudinal Arch of the Foot

Table 1: Structures of the Medial Longitudinal Arch

Factor	Structures	
Bones	Bones: • Calcaneus • Talus • Navicular • 3 Cuneiforms • 1st, 2nd, 3rd metatarsals	
Maintained by	Muscles: ▪ Tibialis anterior ▪ Tibialis posterior ▪ Flexor digitorum longus ▪ Flexor hallucis longus ▪ Abductor hallucis ▪ Flexor digitorum brevis Ligaments: ▪ Long plantar ligaments ▪ Short plantar ligaments ▪ Spring ligaments ▪ Interosseous ligament ▪ Deltoid ligament ▪ Plantar fascia (plantar aponeurosis)	Tendons: ▪ Tendon of Tibialis Anterior ▪ Tendon of Tibialis Posterior (Posterior tibial tendon)

Adapted from Snell, R.S. (2011), Clinical Anatomy by Regions, 9th ed., Lippincott Williams & Wilkins, Baltimore

3.6 Pes Planus (Flatfoot)

Pes Planus is the term used to describe the loss of the medial longitudinal arch of the foot, resulting in a flattening of the plantar surface of the foot and can either be congenital or acquired (Carr et al. 2016).

Congenital Pes Planus is quite common amongst infants and small children and is considered a physiological deformity at young ages due to the laxity of the developing ligaments and lack

of neuromuscular control (Raj & Bhimji 2017). In most cases, this condition in children is resolved as the body grows and a normal arch develops (Halabchi et al. 2013).

In contrast to this, Acquired Pes Planus or Adult Acquired Flatfoot Deformity is a progressive flattening of the arch of the foot. This is most commonly secondary to dysfunction of the Posterior Tibial Tendon (Figure 9 – described in paragraph 2 of Section 3.7), however can also occur as a result of injury to the ligaments of the foot, or mechanical overuse, such as in people who participate in repetitive high impact sports, such as running and basketball (Raj & Bhimji 2017).

3.7 Adult Acquired Flatfoot Deformity (AAFD)

Adult acquired flatfoot deformity is a symptomatic, progressive deformity, described by the American Orthopedic Foot and Ankle Society as; *A progressive flattening of the arch of the foot that occurs as the posterial tibial tendon (PTT) becomes insufficient* (American Orthopaedic Foot & Ankle Society, n.d.). The condition is characterized by a progressive collapse of the medial longitudinal arch of the foot, which results in attenuation of the supporting ligaments of the foot and ankle as the physical deformity is established (Pinney & Lin 2006). AAFD exists as one of the most common etiologies (Abousayed et al. 2016) and affects approximately 19 million adults (aged 21 and over) in the U.S. (NPD Group: National Foot Health Assessment 2012; US Census Bureau 2017).

The PTT is one of the major structures within the foot, functioning as both a plantarflexor, and invertor of the foot (Kohls-Gatzoulis et al. 2004). The origin of the PTT is from the posterior interosseous membrane, tibia and fibula. It then runs behind the medial malleolus, to insert onto the navicular tuberosity, cuneiform and metatarsals (Lhoste-Trouilloud 2012).

[Figure has been removed due to copyright restrictions]

Figure 9: Posterior Tibial Tendon of the Foot

The PTT is an important stabilizer of the longitudinal arch of the foot during dynamic movement (Erol et al. 2015)and acts under tension during gait to invert the hindfoot, locking the transverse tarsal joints, and thus preventing collapse of the medial arch(Trnka 2004). This allows the gastrocnemius (calf muscle) to act most efficiently in providing balance, stability and propulsion during the stance phase of gait (Kohls-Gatzoulis et al. 2004)(see Figure 9).

AAFD is described as a part of a spectrum of pathologies that can be associated with the dysfunction of the PTT.As the posterior tibial tendon deteriorates, functional degradation is experienced, which causes several physical changes to the foot (Figure 10) (Geideman 2000). However, although AAFD was originally described as 'posterior tibial dysfunction' (PTTD), the condition is now recognized to involve numerous other structures (Smyth et al. 2017). It is also understood that secondary to dysfunction of the PTT, the physical deformity can also occur as a result of injury to the ligaments of the foot (Vulcano et al. 2013)through trauma or mechanical overuse, such as in people who participate in repetitive high impact sports, such as running and basketball (Raj & Bhimji 2017).

As a progressive deformity with a spectrum of pathologies, the symptoms of the condition vary and correspond with the stage of the condition. In the earlier stages, pain and tenderness along the posterior tibial tendon are experienced (Carmody et al. 2015).

As the condition progresses, a physical deformity of the ankle is clinically recognized (DiGiovanni & Greisberg 2007; Smyth et al. 2017). This is observed through the;

1. Progressive collapse of the longitudinal arch of the foot
2. Rotation of the heel of the hindfoot, such that the hindfoot is no longer aligned centrally underneath the rest of the leg. resulting in a valgus of the hindfoot
3. Abduction of the forefoot.

[Figure has been removed due to copyright restrictions]

Figure 10: Physical characteristics of adult acquired flatfoot deformity

As the deformity progresses, the foot overpronates. This alters the alignment and position of the foot, which cause the joints located proximally to ankle to compensate for these changes (Figure 11). As a result of this overpronation, the tibial shaft internally rotates (Resende et al. 2015). This causes malalignment of the knees as the knee hyperextends. This tends to cause the meniscus within the knee to grind together, leading to arthritis. The internal rotation of the leg is also accompanied with an internal rotation of the hips. Furthermore, this is also

compensated for by an anterior pelvic tilt (Khamis & Yizhar 2007; Betsch et al. 2011; Yi 2016).

[Figure has been removed due to copyright restrictions]

Figure 11: Compensation Effects of Foot Misalignment

In regards to the symptomatology, the stages of the disorder (Table 2) has been traditionally categorized into 4 stages (Deland et al. 2006; DiGiovanni & Greisberg 2007).

Table 2: Symptoms of Adult Acquired Flatfoot Deformity at Different Clinical Stages

Stage	Symptoms
1	Medial ankle pain and inflammation, may be aggravated by activity. Normal Arch remains.
2	Flexible arch collapse with some deformity observed. Pain is experienced, generally medially over the PTT. As the deformity develops, impingement pain may occur laterally, under the tip of the fibula. A slight valgus of the hindfoot is noted.
3	The deformity progresses, leading to osteoarthritis of the hindfoot joints. Pain which is aggravated further by activity is noted, most commonly occurring laterally, simultaneously with the persisting medial pain.
4	The deformity includes the tibiotalar joint. A severe valgus of the hindfoot is observed, with a lateral tilt of the talus within the ankle joint (mortise). This results in increasing medial pain and arthritis. Stress fractures may occur as a result of the severity of the deformity.

Adapted from Deland JT. Posterior Tibial Tendon Insufficiency results at different stages, 2006

The diagnosis of AAFD is primarily based on a clinical physical examination and radiographic evaluation in conjunction with 'AFFD classification systems' commonly referred to. In the initial stages, plain film x-rays are used to assess the position of the navicular bone (Lotke et al. 2008). In the later stages of the condition, MRI can be used in conjunction with traditional film x-rays in order to determine the pathology of tissue surrounding the PTT (Carmody et al.

2015). MRI techniques are also particularly useful in assessing the degree of arthritic changes occurring within the bones of the hindfoot as a result of the deformity(Vulcano et al. 2013; Toullec 2015). Diagnostic ultrasound has also been used in the assessment of the PTT and in a comparative study between MRI and ultrasound in evaluating the pathology of the tendon, the two techniques were in agreement 77% of the time (Nallamshetty et al. 2005).

As the condition is described as the progressive flattening of the arch of the foot, and the ankle is such an anatomically dense structure, the numerous structures of the foot all play interrelated roles in providing adequate stability and function to the foot and ankle (Bonnel et al. 2010). As the arch progressively collapses, there are numerous soft tissue structures that are involved in the stability of the arch that resultantly are compromised during the flattening of the arch (Richie 2007; Deland et al. 2005). These involve both static and dynamic stabilizers of the foot (Guelfi et al. 2017; Smyth et al. 2017).

The bones and ligaments supporting the arch are referred to as the static stabilizers maintaining the form of the arch, while the dynamic components include muscles and their functions that act during gait to most effectively align the foot for optimum movement (Donatelli 1985).

3.8 Current Clinical Solutions & Treatments

In the early stages of the condition, where deterioration of the posterior tibial tendon occurs, rest and immobilization is recommended to reduce inflammation. Additionally, orthotics and braces are prescribed, alongside physical therapy in order to prevent further progression of the deformity (Vulcano et al. 2013).If the condition progresses to later stages of the condition, which tends to occur through natural loading of the foot over time, the anatomy, positon and function of the foot are compromised (Richie 2007). As a result of this, chronic pain is generally experienced at these later stages and surgical intervention is required (Smyth et al. 2017).

As the symptoms and degree of the condition vary from patient to patient and correlate with the stage of the condition, the specifics of the type of brace or surgical procedure conducted depends on the patient (Snell 2011). The degree of deformity, stage of the condition, function of the foot and goals of the patient are all significant factors to consider during the assessment

of the patient (Table 3) in order to determine the most effective surgical procedure to be conducted (Smyth et al. 2017).

The aim of these surgical procedures is to correct the physical characteristics of the deformity through methods which include; ligament and muscle lengthening, removal of the inflamed tendon lining, tendon transfers, cutting of the bones and placement of implants to realign the bones, joint fusions and ligament augmentation procedures (Van Gestel et al. 2015)to restore the natural arch positon of the foot in an attempt to restore natural functions of the foot (Vulcano et al. 2013).

Table 3: Non-Operative and Operative Treatments for AAFD

Stage	Non-Operative	Operative
1	▪ Rest & immobilization suggested. ▪ Customized orthotics and short articulating Ankle-Foot Orthoses (AFO) prescribed (with either fixed or articulated ankle)	Surgical intervention only required if the patient fails a 3+ month non-operative treatment plan. • Surgical tenosynovectomy • Tendon transfer using the flexor digitorum longus (FDL) tendon to augment the PTT is considered.
2	▪ Customized moulded AFO prescribed (with either fixed or articulating ankle).	Surgical intervention only required if the patient fails a 3+ month non-operative treatment plan. ▪ FDL tendon transfer combined with medializing calcaneal osteotomy (Stage 2a) And/or ▪ Cuneiform osteotomy And/or ▪ Lateral column lengthening calcaneal osteotomy And/or ▪ Spring ligament reconstruction
3	• Customized moulded AFO prescribed (with either fixed or articulating ankle – fixed recommended).	Surgical intervention considered after failed non-operative treatment. ▪ Triple arthrodesis of the hindfoot
4	• Customized moulded AFO prescribed (fixed ankle highly recommended).	▪ Triple arthrodesis to correct the deformity of the foot. Deformity of the ankle can be addressed with: ▪ Deltoid ligament reconstruction ▪ Ankle joint fusion ▪ Total ankle replacement

Adapted from Snell, R.S. (2011), Clinical Anatomy by Regions, 9th ed., Lippincott Williams & Wilkins, Baltimore

3.9 Ligament Damage in AAFD

Adult acquired flatfoot deformity (AAFD) has been recognized as being primarily caused by the dysfunction of the tibialis posterior tendon (Johnson & Strom 1989), injury or overuse of the stabilizing ligaments of the medial column. However, prior to the early 1980s, Adult Acquired Flatfoot Deformity (AAFD) was rarely reported in medical literature (Smyth et al. 2017).

It has been clinically recognized that as the deformity progresses to its end stages and the arch completely flattens, a forefoot abduction and a hindfoot valgus observed (DiGiovanni & Greisberg 2007; Smyth et al. 2017).

This was supported through a previous biomechanics study conducted by Kido et al (2013), whereby the bone rotation during weight bearing was compared between participants with healthy feet and those with flatfoot deformity through 3D models reconstructed from CT images (Kido et al. 2013), it was found that a flatfoot dorsiflexed more in the 1st metatarsal joint (lowering of the medial longitudinal arch), and everted more in the talocalcaneal joint (hindfoot valgus).

Additionally, in a study conducted by Levinger et al (2010), the differences in foot kinematics between normal feet and flatfeet was analyzed using a 3-dimensional motion analysis system incorporating a multi-segment foot model (Vicon Oxford Foot Model). From this study, it was found that participants with flatfeet demonstrated a greater degree of forefoot plantar flexion (-13.7°± 5.6° vs. -6.5°± 3.7°), indicating a collapse of the arch, greater forefoot abduction (-12.9°± 6.9° vs. -1.8°± 6.3°), greater internal rotation of the rearfoot (-10.6°± 7.5° vs. -0.2°± 9.9°) as well as an increased eversion of the hindfoot (hindfoot valgus) (-5.8°± 4.4° vs. -2.5°± 2.6°) (Levinger et al. 2010).

As this physical change occurs, the primary ligaments supporting the joints of the foot are strained as the positions of the bones are displaced (Richie 2007; Deland et al. 2005).

3.10 Classification of AAFD

Despite extensive research, the classification system still clinically relied upon today was one proposed by Johnson and Strom in 1989 (Table 4), which assumes that the level of flatfoot deformity is fundamentally based on the extent of rupture and function of the posterior tibial tendon (Richie 2007).

Table 4: Johnson and Strom Classification (1989)

[Table has been removed due to copyright restrictions]

Retrieved from Johnson KA, Strom DE. Tibialis posterior tendon dysfunction. ClinOrthop 1989;239:197

From this original system, numerous medical and biomechanical studies involving the foot and ankle have been conducted in the attempt to better understand the biomechanics of the foot during the progression of AAFD. Through this, numerous other structures involved have become known (Huang et al. 1993; Braito et al. 2016; Lin et al. 2015; Zhang et al. 2015; Jennings & Christensen 2008; Williams et al. 2014).

Flattening of the arch of the foot has been observed in numerous clinical cases involving patients with either released, or ruptured plantar fascias (Acevedo & Beskin 1998; Sellman 1994). Moreover, cadaveric studies have been conducted to investigate the anatomical results which occur as a result of attenuating primary structures of the foot and ankle complex.

In a study conducted by Cray et al (2013) the effect of releasing the plantar fascia on the strain in the spring and long plantar ligaments was investigated using cadaveric feet. In this study, strain gauges were placed on the spring and long plantar ligaments of 11 cadaveric feet. Axial and cyclic loads were then applied down the tibial shaft of the feet in their natural position both before and after release of the plantar fascia. After the plantar fascia was released, the average strain in the spring ligament increased by 52%. In the long plantar ligaments, there was an observed increase in strain of 94% with plantar fascia release (Crary et al. 2003).

From these more recent findings into the contributions of the foot's structures on the structure and stability of the arch, several authors have formulated their own classification system (Table 5) based on the original system proposed by Johnson & Strom in an attempt to include some of the other structures involved (Smith & Bluman 2012; Raikin et al. 2012).

3.10.1 Bluman Classification System:

Table 5: Bluman et al Classification (2007)

[Table has been removed due to copyright restrictions]

Retrieved from Bluman EM, Myerson MS. Stage IV posterior tibial tendon rupture. Foot Ankle Clin. 2007;12:341–362, viii.

In a later cadaveric study by Lin et al (2014), the ligaments thought to be involved were studied through evaluation of the structural degradation of the ligaments of the foot via MRI in a collection of age matched groups of patients diagnosed with AAFD, compared with control groups of individuals without AAFD.

From this study, the associated structures that experienced any deterioration in patients with AAFD were found to be; the posterior tibial tendon, the spring ligament complex (superomedial & inferomedial components), talocalcaneal interosseous ligament, long and short plantar ligaments, plantar fascia, deltoid ligament, plantar naviculocuneform ligament and the tarsometatarsal ligaments (Lin et al. 2015).

While these ligaments were all found to be involved, the sequential failure of the static support ligaments of the arch of the foot has been identified as the most important event which leads to the eventual complete collapse of the arch at end stage AAFD (Richie 2007; Williams et al. 2014; Oh et al. 2016). At this stage, the most important contributing factor to the end stage of the condition (Stage IV AAF) has been traditionally documented to be the failure of the spring ligament complex (Richie 2007). In clinical practice, this is the structure which is most commonly addressed (Van Gestel et al. 2015; Smyth et al. 2017).

After the spring ligament complex, it has been documented that the other medial column ligament that also experience degradation at the end stages of AAFD (Stage IV), were the talocalcaneal interosseous ligament and the deltoid ligament (Lever & Hennessy 2016; Pinney & Lin 2006).

As such, it has been recognized that the primary stabilizing structures involved in the progression of this condition are the, spring ligament, talocalcaneal interosseous ligament and the deltoid ligament (Lever & Hennessy 2016).

3.10.2 RAM classification System:

The RAM classification system (Table 6) (Raikin et al. 2012) presents the most recent amended version from the original classification system proposed by Johnson and suggests that in contrast to previous understanding, not only in the end stages of the condition does the deltoid ligament begin to stretch and experience mechanical and functional insufficiencies, but earlier on, from stage II of this condition. This insufficiency of the deltoid ligament is included in this system as early as stage II of AAFD on the bases that as the characteristic valgus of the hindfoot is produced, this is associated with the recruitment of the deltoid ligament based on anatomic location of the ligament (Abousayed et al. 2016).

Table 6: Raikin et al Classification (2012)

[Table has been removed due to copyright restrictions]

Retrieved from Raikin SM, Winters BS, Daniel JN. The RAM classification: a novel, systematic approach to the adult-acquired flatfoot. Foot Ankle Clin. 2012;17:169–181.

As suggested in a recent review of AAFD and its classification systems, the main limitation of the original Johnson and Strom classification system for AAFD, is that it is based upon the original assumption that the level of deformity is fundamentally based on the extent of rupture & function of the PTT (PTTD), hence it's "failure in including all other anatomic aspects of the condition" (Abousayed et al. 2016). As a result of this, the importance of other stabilizing structures known to be involved in the stability of the ankle as the condition progresses, namely, the spring ligament, deltoid ligament, naviculocuneiform joint and tarsometatarsal joints (Deland et al. 2006; Pinney & Lin 2006; Lever & Hennessy 2016) have been missed (Abousayed et al. 2016; Lin et al. 2015; Lever & Hennessy 2016).

With the formulation of improved classification systems still based upon the original foundation and structure of Johnson & Strom's system, the validity and reliability of these evolved systems have also not been studied either(Abousayed et al. 2016).

Due to the wide spectrum of presentations in patients within each stage of the condition, Raikin (2012) proposed a suggested treatment plan which fit each patient individually (Raikin et al. 2012). Depicted in the diagram below (figure 12) is the current suggested clinical management plan (Smyth et al. 2017).

[Figure has been removed due to copyright restrictions]

Figure 12: Suggested Clinical Management Plan (2017)
Adapted from Smyth, N.A. et al., 2017. Adult-acquired flatfoot deformity. European Journal of Orthopaedic Surgery and Traumatology, 27(4), pp.433–439.

As shown in the above clinical management plan (Figure 12), the spring ligament is traditionally addressed as early as stage II of AAFD, while the deltoid ligament is not commonly addressed until stage IV AAFD (Hiller & Pinney 2003).

3.11 Current Understanding of AAFD

Through a study conducted by Kido et al (2013), whereby the bone rotation during weight bearing was compared between participants with healthy feet and those with flatfoot deformity through 3D models reconstructed from CT images (Kido et al. 2013). It was found that a flatfoot dorsiflexed more in the 1st tarsometatarsal joint (lowering of the medial longitudinal arch), and everted more in the talocalcaneal joint (hindfoot valgus), which raises questions regarding specific roles of each ligament of the medial column during progression of AAFD.

Moreover, in a study conducted by Baxter et al (2015), the efficiency of various ligament reconstruction techniques in correcting the deformity was evaluated in cadaveric models. It was found that a reconstruction of the tibionavicular portion of the deltoid ligament corrected the hindfoot deformities to a greater extent compared to the reconstruction of the anatomic spring ligament and talonavicular reconstructions alone (Baxter et al. 2015). The authors further state “these findings suggest that other ligamentous structures of the medial arch are critical in supporting the midfoot” (Baxter et al. 2015).

Furthermore, through a study conducted by Williamson et al (2014), it was shown via radiography that a strong linear relationship existed between the hindfoot moment arm (clinical radiographic measurement of hindfoot valgus in stage II AAFD) and the hindfoot alignment angle (hindfoot valgus) (Williamson et al. 2014). This relationship suggests the importance of the deltoid ligament and medial collateral complex during these early stages

(Resnick et al. 1995; Bluman & Myerson 2007). In spite of this, the deltoid ligament is still clinically regarded as a structure involved in stage IV AAFD, which experiences insufficiencies associated with the severe hindfoot valgus tilt (Hiller & Pinney 2003; Raikin et al. 2012; Van Gestel et al. 2015).

Through extensive research, although the stabilizing ligaments of the medial column involved in AAFD are known (Lin et al. 2015; Lever & Hennessy 2016), the sequence of involvement of these structures causing the arch to progressively collapse remains unclear (Gestel et al, 2015; Abousayed, 2016). With various clinical findings, questions have been raised regarding the contribution of the static stabilizers of the medial column to AAFD, particular when the deltoid ligament complex is involved in progression of the physical acquired flatfoot model.

3.12 Human Body & Degrees of Freedom

The human body is quite a complex system, capable of producing a diverse range of physical motions and physiological movements. A degree of freedom (DOF) refers to the number of variables required to determine the position of a mechanism in space, thus describing how the body or system moves in space (Özkaya et al. 2012). For an ordinary body in a 3 dimensional space, there are a maximum of 6 degrees of freedom – 2 per axis. These are translations along each axis (x, y, z), as well as rotations around each of them (Figure 13).

[Figure has been removed due to copyright restrictions]

Figure 13: The Six Degrees of Freedom

3.13 Mechanical Testing

Traditionally, unidirectional and bidirectional testing machines have been used extensively in mechanical and biomechanical research (Sharir et al. 2008; Griffin et al. 2016) as these systems are more readily available for generalized mechanical testing applications. Many traditional testing machines are commercially produced for a range of mechanical testing applications (Figure 14). These testing systems have been used comprehensively for the biomechanical testing of cadaveric specimens to quantify physical and material properties of specimens being tested(Griffin et al. 2016). For more complex and specific application driven

testing, custom built testing machines are often utilized, particularly to conduct biomechanical testing as a result of ethical reasons(Ding et al. 2011).

[Figure has been removed due to copyright restrictions]

Figure 14: Instron Universal Mechanical testing machine

In the human body, the musculoskeletal system of the human body is designed to transmit forces and moments in 6 degrees of freedom (6DOF). The major limitations of commercially available testing systems widely used in biomechanics testing is that they restrict the degrees of freedom and thus are not able to accurately simulate the three dimensional physiological movement of joints and structures (Goldsmith et al. 2015). In order to accurately simulate anatomic movements of the human body and analyze their behavior, 6DOF testing is of paramount importance and value.

In order to simulate joint kinematics in 6DOF, the anatomy of the joint to be studied must be properly understood, as well as the kinematics of that body, in order to accurately reproduce the desired motions (Bates et al. 2015).

3.14 Stewart Platforms - Hexapod Robots

The Stewart Platform (Figure 15) is a mechanical design typically used for position control. Originally designed as a flight simulator, the design consists of several computer controlled serial chains to control a single top plate (end effector) (Ding 2014). The top plate is connected to a fixed base platform via six independent kinematic legs, which can be varied in length. Through the movement of the independent legs, complex physical movements can be simulated (Ding 2014).

[Figure has been removed due to copyright restrictions]

Figure 15: Instron Universal Mechanical testing machine

Stewart Platforms (or Hexapod Robots) are used in many applications where precise six degree of freedom (6DOF) position and motion control are required. Steward Platforms have been used in several specialized industries including; aerospace, automation and nautical industries where they have used to simulate flight, model lunar rovers, position satellite communication dishes and aid in the design of crane hoist mechanisms (Xin 2014).

3.15 Flinders 6DOF Hexapod Robot Testing Machine

With advances in engineering and technology, 6DOF hexapod robot testing systems, originally proposed as a flight simulator mechanism (Dasgupta & Mruthyunjaya 2000), have been increasingly used in testing applications where 6-DOF mobility, large load capacity, and high stiffness and positioning accuracy are required from the testing machine (Ding 2014). Previous custom built 6DOF systems suffered numerous limitations arising from the mechanical structure and control system of these robotic test systems (Ding et al. 2011). Through identification of these issues, a high precision hexapod robotic testing system specialized for simulating complex joint motion through 6DOF biomechanical testing was built (Figure 16) by the biomedical engineering team at Flinders University in collaboration with Adelaide University, South Australia (Ding et al. 2011).

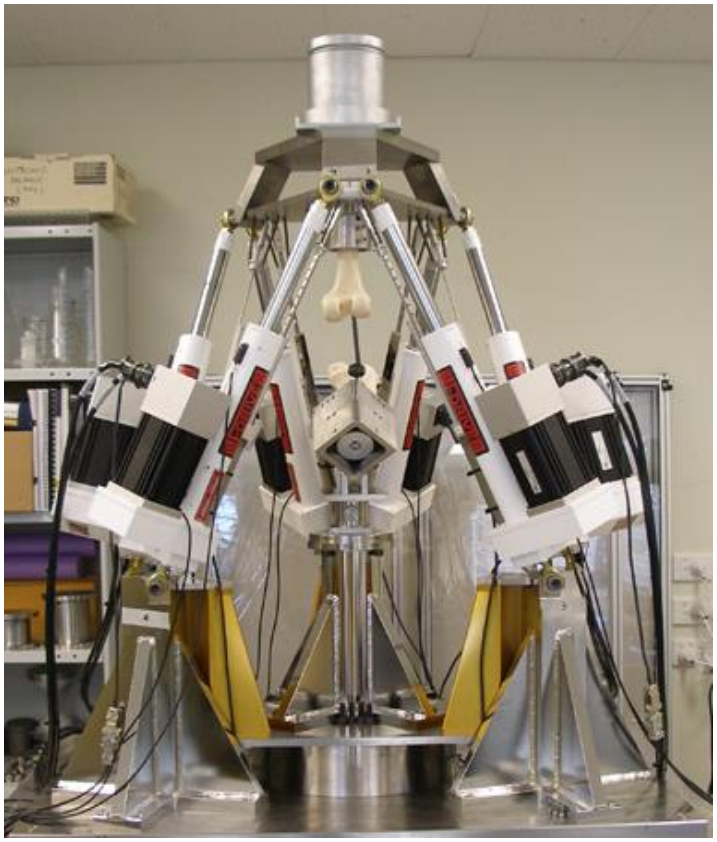

Figure 16: Flinders Hexapod Robot 6DOF Testing

3.16 Ligament Damage: Tears & 'Failure'

It is important to note that in the medical field, ligament "*failure*" is describes the disruption of a ligament (tear), which may be partial (microtears within the fibrous structure) or complete(Petersen et al. 2013). The degrees of ligament tears are graded from 1 to 3, from least, to most severe.

A grade 1 tear corresponds to a stretched ligament with some resulting microtears within the ligament, however the integrity of the structure remains intact and the mechanical structure of the joint is not affected (Provenzano et al. 2002; Petersen et al. 2013).

A grade 2 tear is slightly more severe and involves partial deterioration of the ligament through increased damage to the microstructure of the fibrous tissue. This is attributed with slight laxity due to the further stretching of the structure. This results in moderate instability of the joint (Provenzano et al. 2002; Petersen et al. 2013).

A grade 3 tear is the most severe and is defined as the complete tear (rupture) of a ligament. This results in significant instability of the joint (Provenzano et al. 2002; Petersen et al. 2013).

3.17 Biomechanics of Soft Tissue and Ligaments

The mechanical loading of soft tissue within the body is essential for the healthy maintenance and management of connective tissue structures. These connective tissues (ligaments and tendons) are made up of a diverse group of proteins that form tiny elongated *fibrils* that bundled to form *fibres* (primarily *collagen* fibres) (Hammer 2007).

Hammer et al (2007) stated that "In general, a fibril bundle (fibre) may either fail through an excessively high force, through load-dependent tearing, whereby the collagen fibrils begin to tear as the tensile strength of the soft tissue is surpassed, or by time dependent creep, whereby the collagen fibrils slide past one another and the tissue they form disintegrates" (Hammer 2007).

The effects of mechanical load of connective soft tissue have been studied by mechanical testing to elongate soft tissue structures to the point of rupture (Robi et al. 2013). From this, the overall tissue response of collagen when applied mechanical loads is well understood in soft tissue biomechanics and can be expressed through the non-linear stress strain curves that are typical of these soft tissue structures (Hammer 2007). The stress strain curve for ligaments and tendons shown below (figure 17) highlights the basic ranges of the curve (toe, elastic and plastic regions).

[Figure has been removed due to copyright restrictions]

Figure 17: Normal Stress Strain Curve for Ligament and Tendons
Retrieved from Hammer, W., 2007. The Effect of Mechanical Load on Soft Connective Tissues. In Functional Soft-tissue Examination and Treatment by Manual Methods. Massachusetts, USA: Jones & Bartlett Learning, pp. 16–20.

The **Toe Region** of the stress strain curve describes the behavior of ligaments when subjected to small loads, resulting in a strain between 1.2% - 1.5% ($0.012 < \varepsilon < 0.015$) (Robi et al. 2013). During this range, there is a preliminary and temporary straightening of the 'normally crimped' collaged fibers. Within this range, upon release of the loads, the length of the tissue

is restored and the natural 'crimp' of the individual fibrils comprising the collagen fibers are regained, thus highlighting the elasticity properties of the soft tissue structures within this range. It is hypothesized that this region defines the normal functional range that ligaments within the body act within (Hammer 2007).

The **Linear Region** of the curve describes the behavior of ligament structures from the point where the collagen fibrils have been slightly elongated to the point where they have lost their natural crimp (Robi et al. 2013). In the earlier phase of the linear region ($\varepsilon\% < 4\%$; $\varepsilon < 0.04$), the extension of the ligament is still within the physiological range and upon release of loading, the structure of the tissue is recovered. Upon exceeding 4% strain, the natural crimp of the collagen fibers is permanently lost as the fibrils begin to slide past one another, denaturing the crosslinks between fibrils (Hammer 2007). As the strain of the ligaments collagen fibers is increased between the range of 4%-8% ($0.04 < \varepsilon < 0.08$) (Robi et al. 2013), the collagen fibers begin to slide past one another and the cross links existing between the fibers begin to fail, resulting in micro tears (microscopic failure) within the ligament (Hammer 2007). Within this linear elastic range, the denatured fibrils can still stretch; allowing the gross tissue structure to continue to elongate and recover is length upon removal of the load. The natural crimp of the ligament fibrils however will still be lost and this can be observed ultrasonically (Hammer 2007).

The higher end of the linear region of the curve (strains exceeding 8% ($\varepsilon > 0.08$)) (Robi et al. 2013) can be further distinguished as a "**progressive failure**" region, where internal micro-failure of the collagen fibers begins to occur, but the appearance of the ligament at the gross level remains intact. At this point, unrecoverable elongation of the ligament begins to occur (Hammer 2007).

Upon further strain of the ligament (strains exceeding ~11% ($\varepsilon > 0.11$) (Hammer 2007), the behavior of the ligament enters the **Plastic Region** of the curve. This region can further be distinguished as "**Major failure**" and "**Complete failure"** regions. As the ligament is increasingly strained at this region, the collage tissue of the gross ligament itself begins to fail(Robi et al. 2013). This point is identified as the *yield point* of the stress strain curve. As further stress is applied and the strain within the ligament increases further, complete failure of the ligament occurs rapidly, which is exhibited as a rupture of the gross (Hammer 2007; Robi et al. 2013).

3.17.1 Characteristic Tissue Responses of Biological Soft Tissues

Biological soft tissue are viscoelastic materials that possess characteristic properties of stress relaxation and creep, which are typical responses of the tissue when subjected to strains and stresses, respectively.

Stress relaxation is a phenomenon which occurs in soft tissue that is strained at a constant strain (i.e stretched and held at a distinct static length). When this occurs, the stress experienced within the tissue declines over time. As a viscoelastic material, the characteristic stress relaxation property is dependent on the strain rate. At higher strain rates, the stresses within the tissue are higher, and the succeeding force relaxation magnitude is greater. (for details, refer to The University of Auckland 2015).

Creep is a phenomenon that occurs within soft tissue when a constant stress is applied to the material. When subjected to the constant stress, there is an initial instantaneous increase in the strain of the tissue, followed by an increasing strain over time. This increasing strain occurs with a decreasing strain rate, such that eventually a steady state of strain is reached.

When the loads are removed, elastic strain is immediately recovered, after which there is an anelastic strain recovery, whereby strain in recovered over time. (for details, refer to The University of Auckland 2015).

In an in vitro cadaveric experiment, these typical responses of viscoelastic materials are exhibited by the biological soft tissue and experiments must be designed with this in mind. Without doing so, the results obtained from the experiment may be unreliable.

3.18 Strain Measurement of Soft Tissue

When a ligament or tendon is loaded, it undergoes strain. The strain experienced by the soft tissue is dependent on both the stresses applied, as well as the material properties of the tissue (Fleming & Beynnon 2004).

The strains (ε) within a ligament can be calculated from the measurements of displacement (L) using the engineering formula for strain(Fleming & Beynnon 2004):

(×100%)

$$\varepsilon = \frac{L - L_0}{L_0}$$

where L_0 and L refer to the original and displaced lengths, respectively. As shown by the equation, L_0 is used to normalize the displacement response.

In biomechanics studies, it is necessary to take accurate and precise measurements of the mechanical function of soft tissue, including strain within ligaments *in situ*. This is essential from the clinical perspective in order to gain an insight into injury mechanisms, improving prevention strategies and hence develop better treatment options that better optimize healing (Arms et al. 1984).

For measurements in biomechanics, the complex structure and loading conditions of soft tissues within the body make in vivo measurements challenging to obtain (Fleming & Beynnon 2004).

For measuring strain *in situ,* two approaches have been documented (Fleming & Beynnon 2004);

1. displacement measurements between insertion sites of the ligament
2. displacement measurements between known points within the mid-substance of the ligament itself

Within the body, the strain tends to increase closer to the insertion sites of the ligament (Butler et al. 1992). As the distribution of strain is not consistent along the length of the ligament, the first approach provides an average strain response across the entire length of the ligament.

Current techniques of measuring strain involve devices which are directly attached to the soft tissue itself (i.e. strain gauges, differential variable reluctance transducers and hooked extensometer) (Fleming & Beynnon 2004). With emerging technology and advances in the engineering field, non-invasive methods using optical techniques (i.e. magnetic resonance imaging (MRI)) have shown to be promising.

3.18.1 Hooked Extensometer

Henning et al. (1985) performed the first attempt of measuring strain response of the anterior cruciate ligament (ACL) with the knee i*n vivo* in 1985. The technique consists of securing a hooked wire probe to the ligament such that displacements within the wire, relative to the tibial attachment could be measured via an elongation gauge (Henning et al. 1985). Figure 18 illustrates the placement of the wire probe and elongation gauge within the knee as used by Henning to measure the ACL strain response.

As an early method of measuring the strain response with a ligament, arbitrary units for the change in wire position were used to quantify the displacement response of the ACL. This same scale was used across a range of different movements. As the stress and strain distributions across ligaments within the bod (particularly the ACL) depend on the loading conditions and vary along the dimensions of the ligament, this posed many limitations to the implantation of this technique (Fleming & Beynnon 2004). In addition, the implementation of the hooked extensometer was physically invasive, intricate, and obstructive when attempting to measure the displacement of more than one ligament.

[Figure has been removed due to copyright restrictions]

Figure 18: Hooked Extensometer Measuring ACL Strain
Retrieved from Henning, C.E., Lynch, M. A. & Glick, K.R., 1985. An in vivo strain gage study of elongation of the anterior cruciate ligament. The American journal of sports medicine, 13, pp.22–26.

3.18.2 Differential Variable Reluctance Transducer (DVRT)

DVRTs are small displacement sensors directly attached to a ligament (Figure 19) and have been used to measure the displacement of various ligaments and tendons (Fleming & Beynnon 2004).

In studies measuring the strain response of the ACL, a small, highly compliant DVRT is used. This instrument is approximately 5mm long and is capable of a monotonic sensing range of approximately 1.75mm (strain range of 35%) (Fleming & Beynnon 2004).

For insertion, an incision is made into the specimen in line with the fibers of the ligament, and an arthroscope is used to view the ligament and place the DVRT along the fibers of the ligament (Fleming & Beynnon 2004). This is illustrated below in figure 19.

The DVRT has exhibited good biocompatibility and is easily calibrated. Furthermore, due to its design, minimal movement artifacts are introduced to the sensors reading(Fleming & Beynnon 2004). In contrast to this, although the DVRT is a small sensor, when placed in confined spaces due to physical anatomic features or the presence of dense structures, the range of motion of joints can be restricted. This is observed when a DVRT is placed on the ACL of the knee. In this application, upon extension of the knee, the sensor impinges on an anatomical feature of the femur (intercondylar notch) and restricts the range of motion (Fleming & Beynnon 2004). Due to this consideration, when measuring the strain response of a ligament(s) within anatomically dense spaces, where flexible physiological movement of the joint is essential (i.e. the foot and ankle), the use of DVRT's is not preferred.

In addition to this, as the DVRT is placed on the mid-substance of a ligament, its output is related to the relative change in the mid-substance displacement between the two barbs of the sensor (Fleming & Beynnon 2004).

[Figure has been removed due to copyright restrictions]

Figure 19: DVRT Measuring ACL Strain
Retrieved from Fleming, B.C. & Beynnon, B.D., 2004. In vivo measurement of ligament/tendon strains and forces: A review. Annals of Biomedical Engineering, 32(3), pp.318–328.

3.18.3 Radiostereometric Analysis (RSA)

Radiostereometric Analysis (RSA) is an imagine technique that is capable of capturing the positions and displacements of points in a 3 dimensional space using X rays (Bottner et al. 2005). This technique involves the capture of 2 simultaneous radiographs, after which digital transformation of these images combine the radiographs to produce a spatial reconstruction of the body in 3D space (Figure 20).

RSA was first clinically used for the monitoring of the motion of the spine, as well as overserving the displacement of facial bones and extremities with age. Now, RSA is most

commonly used in the application of monitoring the migration of implants, whereby the amount of micro motion which occurs between the implant and interface can be observed (Bragdon et al. 2003), such as to predict the clinical loosening of implants, which is of significant importance to the development of future implants and prolonging revision procedures (Kärrholm et al. 2006).

The setup for RSA involves a calibration cage, where there are a number of small tantalum beads, evenly spaced from another in specifically defined positions. These act as reference points for each axis that define a 3D coordinate system. Pairs of left and right x-rays (stereoradiographs) are captured and the 3D spatial environment is generated through the mathematical transformations of the 2 radiographs (Bragdon et al. 2003; Kärrholm et al. 2006) (see Figure 20).

With this defined reference coordinate system in a digital 3D space, tantalum beads that are placed within the reference cage (implanted within specimens) can also be captured by the dual radiographs, producing a 3D spatial reconstruction of the marked landmarks within the frame with their coordinate positions relative to the configured coordinate axis known (Bragdon et al. 2003).

As an optical technique, the RSA measurement system can be used in conjunction with multiaxial biomechanics testing machines without severely constraining the physical setup. This allows for the position of the specimen to be easily manipulated without being affected through obstruction of the measurement instrument.

In addition to measuring strain, the RSA technique also enables radiographic visualization of the internal structures of the foot and ankle. Through the digitization of captured stereoradiographs, the digitized 3 dimensional data can then be integrated with computer software and thus be further manipulated in post processing.

[Figure has been removed due to copyright restrictions]

Figure 20: Radiostereometric Analysis setup illustrating calibration cage and dual x-rays *Retrieved from Lauge-Pedersen, H., Hagglund, G. and Johnsson, R. (2006). Radiostereometric analysis for monitoring percutaneous physiodesis: A Preliminary Study. Journal of Bone and Joint Surgery - British Volume, 88-B(11), pp.1502-1507.*

Any displacement that occurs to the tantalum beads within the cage can then be tracked and analyzed through the comparison of sequential reconstructed images. The accuracy of this tracking depends on the resolution of the radiographs captured, however with most modern RSA systems, the X rays are capable of distinguishing the position to a resolution of between ±10-250 microns (±10-250 μm) (Tashman & Anderst 2003).

Due to the foots anatomically dense structure, with many ligaments that cross over and overlap one another, with several different constituent component to each ligament that lie at different depths to one another (superior, inferior, plantar, dorsal components) (Hodler et al. 2017; Houglum & Bertoli 2012; Fraser et al. 2016), implementing strain gauges and hooked extensometers to simultaneously measure strain several ligaments of the ankle while maintaining natural range of motion may be difficult (Fleming & Beynnon 2004). Moreover, complexities regarding physically placing several of these strain gauges on the numerous ligaments to be analyzed are introduced.

In a biomechanics study conducted by Bass (2014), the RSA technique was implemented to investigate the strain in the ACL of sheep's knees under basic movement (simple flexion of up to 20°)(Bass 2014). In this study, an RSA calibration cage was designed for use with sheep knees, allowing successful integration of the RSA technique with the Flinders hexapod robot.

In a future study (Garcia 2015), the RSA technique was again implemented to investigate the strain in the ACL of sheep knees during complex movements. In this study, the Bass's RSA calibration frame design was used to track the positions of tantalum beads placed along the ACL, MCL, LCL and PCL. Upon comparing ligament displacements, the strain within the ligaments could be measured.

Chapter 4: Development of Experiment

Several authors have created various flatfoot models cadavers by sectioning the stabilizers of the medial arch (Chu et al. 2001; Huang et al. 1993; Imhauser et al. 2002; Patterson et al. 2003; Baxter et al. 2015). With the sequential involvement of the stabilizing structures leading to the progressive collapse of the arch remaining unclear (Van Gestel et al. 2015; Abousayed et al. 2016), there are clear limitations to how closely the flatfoot models (via resection of ligaments) resemble the clinical deformity (Zhou et al. 2017). "We admit that there are several limitations to our study. First, the created flatfoot model differed to some extent from clinical flatfoot deformities. It was difficult to simulate severe adult-acquired stage II B flatfoot deformity completely,"(Zhou et al. 2017).

With advances in technology and engineering, biomechanical testing simulations are now possible in 6 degrees of freedom (6DOF), thus there is an important need to develop an experimental procedure to simulate the physical characteristics of AAFD while leaving as many of the soft tissue structures intact. In doing so, the relationships between the ligaments of the medial column and the progression of the physical deformity can be better understood.

This study is innovates the use of a novel 6DOF hexapod robot to simulate the physical characteristics of the deformity and the design of a RadioStereometric analysis system, allowing the static stabilizing ligaments of the medial column to be simultaneously observed. This chapter presents the technical considerations and experimental design required to simulate the physical deformity and elicit data from the experiment.

Numerous components of the experimental design were developed individually and then combined to validate the system, prior to both pilot, and specimen testing.

Firstly, the loading conditions subjected to the foot specimen to produce the required characteristics of adult acquired flatfoot deformity (AAFD) were developed. Following this, the RSA calibration frame was designed and fabricated, through which a MATLAB software was programmed to operate with. This system was then tested and calibrated using a digitally designed mock foot with carefully placed markers in known locations.

The anatomy of the foot and ankle was then studied, from which the bead implantation protocol could be developed and validated. Following this, the test specimens were implanted with the trackable tantalum markers to be detected by the designed RSA system.

Succeeding this, the fixation method of the foot specimens were developed, along with the method of applying tension to the Achilles tendon.

4.1 The Hexapod Robot 6DOF Testing Machine

The Hexapod Robot Testing System is a custom designed and built 6DOF testing machine based on the concept of the Stewart Platform, purpose driven to enable complex 6DOF testing of bones, joints, soft tissues and accurate simulation of entire limb biomechanics. The robotic system consists of a fixed base and a mobile top plate, controlled by six servo-controlled ball screw driven actuators that allow the precise positioning of the top plate relative to the base of the hexapod. Each leg of the hexapod contains six linear optical incremental encoders, each capable of measuring displacements and rotations with a resolution of 0.5μm (Ding et al. 2011). The hexapod is uniquely designed with these encoders positioned independently of the loading frame and load cell, thus eliminating many of the issues arising from system compliance of the load cell from the measurements of specimen behavior. Common to most other mechanisms for material testing (Ding et al. 2011), a six axis load cell is positioned above the top plate and measures forces and moments with a maximum compressive axial force of 4,400N and axial torque of 110Nm. As previously validated by the National Associated of Testing Authorities Standards (NATA), The Hexapod Robot measures compressive force to an accuracy of ±9N, axial torque to an accuracy of ±0.2N, and displacement and rotation angle to an accuracy of 0.01m (Ding 2014). Additionally, high bandwidth control of the hexapod is implemented through a combination of LabVIEW system running real time on a floating point Intel Processor. Through the unique mechanical design, and independent control system, highly accurate control and simulation of complex physiological movements in 6DOF can be achieved, the specifications of which match or exceed other currently existing testing systems (Ding et al. 2011).

As the state of the art biomechanical testing system was readily available, the simulation of an accurate anatomical adult flatfoot would be accurately produced in a cadaveric model using the hexapod robot 6DOF testing system.

4.2 Basic Ankle Kinematic Control with the Hexapod

As no biomechanical testing of the human foot and ankle joint had previously been conducted with the hexapod 6DOF robot, along with the fact that the kinematic and biomechanical behavior of the ankle joint is quite different and relatively complex in comparison to other joints previously tested within the hexapod (Spine and knee biomechanical testing), the resulting behavior of the foot under basic loading conditions applied by the hexapod needed to be explored. This is primary due to the fact that under normal physiological conditions, when the foot is subjected to loads and movements, complex mechanisms occur within the foot, resulting in significant laxity and movement of the joints and soft tissue structures as a means of shock absorbing and evenly redistributing weight (Houglum & Bertoli 2012; Fraser et al. 2016). When replicating physiological ankle kinematics within the hexapod, a laxity of the foot would occur (Barber Foss et al. 2009; Mitchell et al. 2008; Kovaleski et al. 2008), and how the hexapod would react to this under externally applied loads needed to be tested. In addition to this, prior to attempt simulating of specific position movements within the hexapod (simulating characteristics of AAFD), it was important to begin by producing basic anatomic movements of the ankle under control of the hexapod robot (flexion and extension).

In order to do this, a rigid sawbone foot model with a flexible ankle joint was fixated to a top cup via bolts which held the tibia and fibula in place, centrally aligned with the center of the cup. Poly methyl methacrylate (PMMA) was then poured into the cup, fixating the tibia & fibula to the cup. At this point, the center of rotation of the model ankles talocrural joint (Axis of Rotation - AoR) was identified through visual and physical examination, verified by an orthopaedic foot and ankle specialist and both the X and Z offsets (coordinate axis offsets from AoR to the top of the fixation cup) measured from the central point at the top of the fixation cup. As the talocrural joint was centrally aligned with the center of the top cup during fixation through careful positioning by an orthopaedic foot and ankle specialist, the Y offset was recorded as ~0.

The top cup was then secured to the top of the hexapod Specimen Coupling Plate using 4 M6 countersunk screws. The Specimen Coupling Plate was then bolted to the Load Cell Plate via 4 M8 socket head screws. The bottom of the foot was not fixated to the base plate to allow normal physiological freedom in movement of the joints and structures in response to externally applied load and position controls applied to the distal tibia.

Once the sawbone model was mounted to the hexapod robot, the initial offset values for the talocrural joint were entered. The hexapod robot then created a floating point around the measured joint center, and through initial movement, the anatomical center of rotation of the ankle joint was automatically honed in by the robots feedback control system.

A light axial compressive load of 100N was then applied to the ankle joint through the fixated tibia & fibula. It was noted that the foot splayed out slightly, and the hexapod maintained its position and control, with force and position feedback data displayed on the real-time control system graph.

In combination with the applied axial load, repeated cyclic flexion &extension of the ankle joint was then successfully simulated in the hexapod's *position control* mode. Through this, the model foot reacted anatomically and the hexapod behaved well under simulated control of the robotic system.

Figure 21: Hexapod Robot simulating basic flexion and extension of a sawbone model foot (Dorsiflexion and Plantarflexion)

4.3 Producing an anatomical flatfoot position

In order to simulate a position that closely resembles that of an anatomical flatfoot, such as to analyze the behavior of the stabilizing ligaments, the anatomical alignment abnormalities in a symptomatic adult flatfoot needed to be established.

As clinically recognized, a symptomatic flatfoot is commonly physically identified through;

1. A collapse of the longitudinal arch of the foot
2. Forefoot Abduction
3. Hindfoot Valgus (talocalcaneal angle)

This was supported through Levinger et al (2010), where a 3-dimensional motion analysis system (Vicon Oxford Foot Model) was used to analyze the differences in foot kinematics between normal feet and flatfeet. From this study, it was found that participants with flatfeet demonstrated a greater degree of forefoot plantar flexion (-13.7°± 5.6° vs. -6.5°± 3.7°), indicating a collapse of the arch, greater forefoot abduction (-12.9°± 6.9° vs. -1.8°± 6.3°), greater internal rotation of the rearfoot (-10.6°± 7.5° vs. -0.2°± 9.9°) as well as an increased eversion of the hindfoot (hindfoot valgus) (-5.8°± 4.4° vs. -2.5°± 2.6°) (Levinger et al. 2010). This kinematic data from the literature was essential in highlighting the physical characteristics of the deformity as clinically observed, as well as the range of anatomical change present in the individuals.

3D bone rotation data upon weight bearing for individuals with normal and flatfeet (Kido et al. 2013) supported Levinger's findings which were in line with the physical changes associated with the deformity (i.e. collapse of the longitudinal arch, valgus of the hindfoot, abduction of the forefoot) (DiGiovanni & Greisberg 2007; Smyth et al. 2017). This provided a foundation for the physical characteristics of AAFD to be simulated within the hexapod to replicate the deformity.

To externally produce the required anatomic abnormalities through the application of forces and moments to the foot, an understanding of basic mechanic principles and biomechanics was central in understanding the behavior of bodies when subjected to forces and moments whilst considering the mechanics of the human body, physiological movement of the foot and its inherent structures, as well as how biological soft tissue will behave in response to applied loading conditions(Bates et al. 2015). Moreover, significant physiological and anatomical

understanding of the foot, ankle and biological soft tissue was critical. In addition, significant medical & clinical knowledge and experience was required, hence why the involvement of two orthopaedic surgeons specializing in the foot and ankle was paramount to the project. To biomechanically produce the physical changes highlighted by Kido et al (2013) and Levinger (2010) in normal feet, the required loading conditions were conceptualized, and then tested under control of the hexapod robot with a sawbone model. Following this, testing was also conducted with a normal cadaveric foot specimen, under the observation of an orthopaedic foot and ankle specialist.

To simulate this anatomical abnormality in intact normal feet (no indication of ailments relating to the foot), without sectioning any static stabilizers, two loading condition application methods were proposed to produce similar physical characteristics of flatfoot as found from Levinger's study(Levinger et al. 2010). To initially theorize the loading conditions, a physical movable sawbone foot model was used conceptualize the three dimensional anatomic arrangement of the foot and how the structures would physically react under different loading conditions.

1. Applying a compressive axial load vertically down the tibial shaft, combined with an internal axial rotation applied to the tibia.

[Figure has been removed due to copyright restrictions]

Figure 22: Internal rotation of the Tibia + compression through tibial shaft
Adapted from https://www.cl3ver.com/blog/cl3ver-for-medical-presentations-anatomy-of-the-foot-and-ankle/

2. Applying dorsiflexion to tibia, simulating the stance phase of gait, where the body is aligned over stationary foot. A vertical compressive load is then applied through the tibial shaft, as the tibia is lined approximately over the talonavicular joint.

[Figure has been removed due to copyright restrictions]

Figure 23: Dorsiflexion + Compression
Adapted from https://www.cl3ver.com/blog/cl3ver-for-medical-presentations-anatomy-of-the-foot-and-ankle/

Through these two conceptualized methods and the visual and physical aid of a 3D sawbone model, it was hypothesized that through the application of these external forces, physical anatomical changes would resultantly occur to the structures within the foot, thus producing the physical characteristics of a clinical flatfoot deformity based on the alignment abnormalities (of a flatfoot) documented by Levinger (Levinger et al. 2010).

Taking the biomechanics of the body and natural loading conditions of the foot and ankle into consideration, the two methods of loading application were reconsidered. Method 1, which involved applying an axial internal rotation about the tibia was less favorable due to the fact that the loading condition of the tibial rotation to produce the deformity does not naturally occur in the human body, thus, the 'flatfoot' model which would be produced (hindfoot valgus, forefoot abduction, collapse of longitudinal arch), would not be produced under physiological conditions.

In contrast to this, Method 2 involved bringing the foot into a slight dorsiflexion (~10 degrees – maximum physiological dorsiflexion of the foot), hence simulating the natural stance phase of gait. In this position, the body is naturally aligned above the stationary foot. Through applying a compressive load through the tibia in this position (approximately above the talonavicular joint - medial ankle), the 'flatfoot' model produced would be under natural physiological conditions.

Upon discussion with several orthopaedic foot and ankle specialists, the importance of the natural loading conditions experienced by the human body was highlighted as being an important factor to take into account. Thus, the characteristics of AAFD were to be induced by dorsiflexing the foot such that a compressive load could be applied approximately through the talonavicular joint (loaded through tibial shaft).

4.3.1 Simulating Flatfoot position in Flexible Sawbone Model with the Hexapod Robot

To first validate whether the proposed loading condition would produce the required anatomic alignment abnormalities to be replicated (flatfoot model), a flexible sawbone foot model with elastic ligaments between the joints of the ankle was mounted to the hexapod robot with the rest of the foot unconstrained to allow for subsequent movement of the joints within the foot.

The proximal tibia was aligned centrally within a top cup and fixated with PMMA, similar to the potting method used previously when initially testing basic ankle kinematic control within the hexapod. The center of rotation of the ankle joint was aligned centrally with the top cup, such that the Y offset relative to the center of the hexapod was 0. The X and Z offsets of the specimens' axis of rotation (talocrural joint) were measured and input into the hexapod's control settings. The foot model was then placed in dorsiflexion through translation of tibia, such that the proximal end of the tibia lined approximately over the talonavicular joint. This was recorded by the real-time position feedback system as approximately 10 degrees of dorsiflexion, simulating the natural stance phase of gait (Johanson et al. 2006). In this position, a compressive load of 100N was then applied through the tibia. Under these loading conditions, a resulting collapse of the medial longitudinal arch, an eversion of the rearfoot (i.e. hindfoot valgus), and a subsequent abduction of the forefoot was established. After examination of the deformity produced in sawbone model by an orthopaedic foot and ankle surgeon, it was agreed that the physical characteristics of a clinical flatfoot deformity had been induced.

Figure 24: Hexapod Robot Simulating physical characteristics of flatfoot in sawbone model

4.3.2 Development of Hexapod Operation Load Control Protocol

In a biomechanical study conducted at the Mayo Clinic, Rochester, Minnesota, an evaluation of the various static stabilizers on the overall stability of the longitudinal arch was conducted through the sequential sectioning of the spring ligament, plantar fascia and plantar ligaments in cadaveric specimens while subjected to vertically compressive loads through the tibial axis of 230N, 460N and 690N via an instron uniaxial testing machine (Huang et al. 1993). From this study, the changes in vertical and horizontal dimensions of the medial arch were measured. Based upon the mean resting arch height in intact feet (57.42 ± 2.7mm) and resulting mean arch height displacements in intact feet under these loadsteps (230N: 2.14 ± 0.9mm; 460N: 2.83 ± 0.9mm; 690: 3.32 ± 1.2mm), the loading conditions applied by Huang et al (1993) formed the basis for the incremental loadsteps implemented in this study as it provided an indication into the degree of flattening of the arch as external loads were applied. To produce greater reduction in arch height, as typically seen in patients with stage IV flatfoot deformity, an additional load step of 920N was included in this study. Additionally, in order to observe preliminary displacement of the joints under a preliminary light load, an initial load step of 100N was included. These loading conditions were to be applied under load control of the hexapod robot in order to progressively flatten the longitudinal arch and induce the desired hindfoot valgus and forefoot abduction in the cadaveric feet.

These loading conditions were then documented as control inputs for the hexapod robot. A full protocol for operation, input and control of the hexapod robot to simulate the required position was developed (**Refer to Appendix F**).

4.4 RadioStereometric Analysis (RSA)

As the deformity is simulated under control of the hexapod robot, the internal biomechanics of the primary static stabilizing ligaments needed to be monitored. For this study, a method of RadioStereometric Analysis (RSA) was used to capture the internal biomechanics of the ligaments in three dimensions as the deformity was progressively produced. To do so, a base plate to sit the ankle upon, which also served as a calibration cage (containing reference rods to configure the reference digital coordinate system from the Stereoradiographs)(Bragdon et

al. 2003; Kärrholm et al. 2006), needed to be designed and fabricated, making it possible to track the position of markers lying within the cage (i.e. within the foot & ankle).

4.4.1 Design of Base Plate RSA Calibration Frame

In a previous study conducted at Flinders University, the RSA technique was implemented to analyze strain within the ligaments of a sheep's knee during complex everyday movements (Bass 2014; Garcia, 2015). These studies both involved the implementation of an RSA calibration cage which fit within the physical constrains of the hexapod and allowed for the mounting of a sheep knee specimen with the calibration cage.

Figure 25: RSA Calibration frame for measuring ACL strain in Sheep knees
Retrieved from Garcia, M., 2015. Identification of ACL strain during complex movements. Flinders University, South Australia.

This calibration cage, served as a foundation for the design of the foot base plate calibration cage, allowing the RSA technique to be utilized in the biomechanical analysis of the human foot and ankle under simulated control of the hexapod robot 6DOF testing machine. The

design and configuration of this foot base plate/calibration frame was developed with the intent for it to be easily adapted to future foot and ankle biomechanical studies utilizing the hexapod robot to simulate ankle kinematics.

4.4.2 Objectives of Design

The base pillar needed to provide support for the base of the foot, while fitting within the physical constraints of the hexapod robot. Additionally, 4 evenly distributed 'calibration pillars' were to be secured to the base plate in evenly spaced positions. These calibration pillars were paramount to the design as the tantalum markers on these calibration pillars allowed for the initialization and calibration of the digital reference 3D coordinate system when the Stereoradiographs are fed into the 3D reconstruction MATLAB script.

With this in mind, the design requirements for the Hexapod Foot Base Plate/RSA Calibration plate were:

1. Fit a range of different sized foot specimens
2. Be compatible with the Hexapod Robot and easily adapt to the base adaptor of the 6DOF testing machine.
3. Fit within the physical constrains of the hexapod
4. Be constructed out of a radiopaque material for X-Rays to pass through it with minimum attenuation

4.4.3 CAD Design

CAD Software Autodesk Inventor was used to draw up a model of the base plate. (Refer to Figure26)

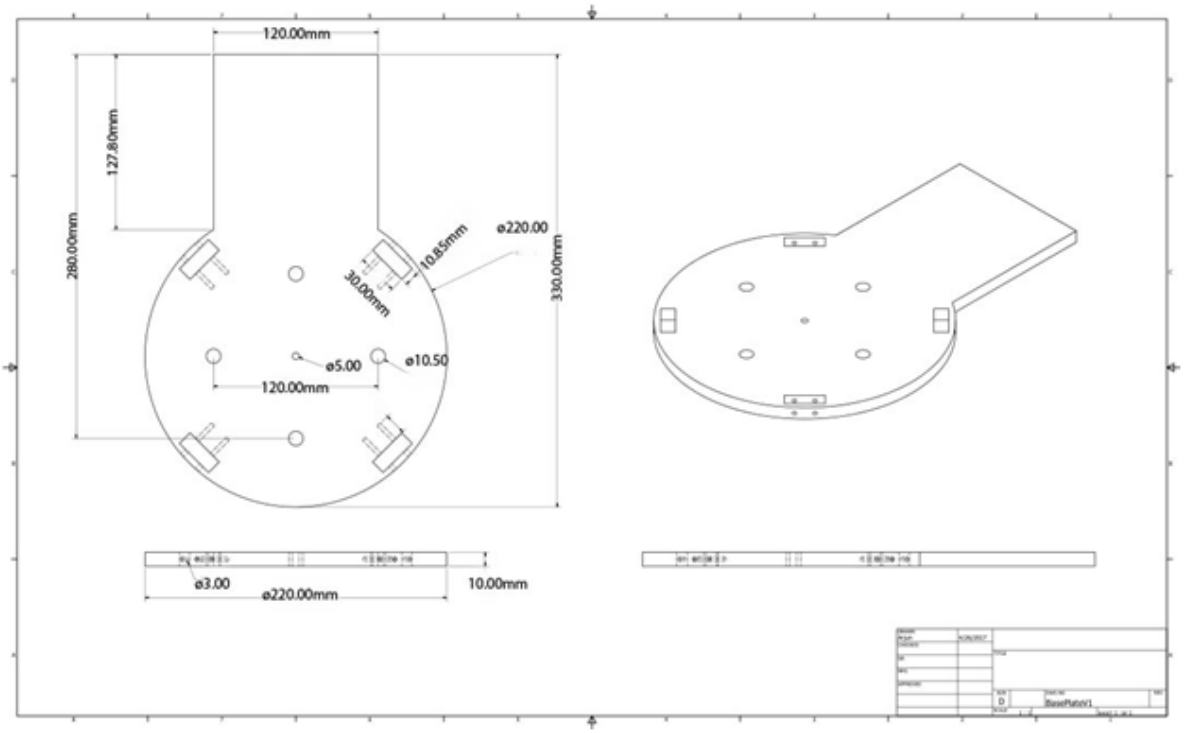

Figure 26: Concept base plate calibration cage design for foot and ankle testing

The model was then 3D printed and used in the 1st kinematic pilot study (simulating basic ankle flexion & extension) within the hexapod using the sawbone model as described above in Section 4.2, (Basic Ankle Kinematic Control with the Hexapod Robot).

The RSA Calibration Rods were digitally designed in CAD software Autodesk inventor, with the positons of the reference beads placed at measured location of the digital design itself. These calibration rods were then laser cut in acrylic for accuracy. Tantalum beads were placed into the extruded holes within the thickness of the rod at the laser cut positions and pushed in until the bead lay at the full depth of the extrusion. The beads were then glued in place to restrict motion.

Figure 27: Concept base plate calibration cage design with sawbone foot model

4.4.4 Redesign of Base Plate Calibration Frame

From the initial test of the prototype to check for compatibility and function, it was noted that the orientation of the baseplate did not allow for effective control of the mounted foot specimen as the base plate, and hence foot was not in line with the coordinate axis of the hexapod robot system. Resultantly, an additional design requirement to orientate the base plate and calibration pillars with the primary coordinate axis of the hexapod was added. This modification was required to allow for the effective control of the potted foot specimens via the hexapod. This change also reduced the added complexity of implementing 'coordinate axis transformations' into the stereo X-Ray digital transformation MATLAB script.

In addition to this, another problem was noted where amendments needed to be made to the design. As most of the tantalum markers to be captured were to be implanted primarily on the plantar side of the foot, it was critical to be able to capture these markers on the X-Ray images. With the Steel base pillar which was is normally fixated to the hexapod robot to allow for the most effective range of motion of the testing machine, the markers on the bottom of the foot were not able to be identified on the X-Rays due to the steel base pillar under the base plate obstructing the view of the radiographs.

As such, two additional Design Requirements needed to be made

1. Base plate &RSA Calibration pillars must maintain positions orientated with the primary axes of the hexapod
2. Design a radiopaque base pillar which adapts to both the Hexapod robot, and the existing Foot Base Plate/calibration frame.
3. Design a x-ray cassette mounting bar to attach to the base pillar that adapts to previously designed x-ray cassette holders (allowing consistency of captured radiographs)

To re-orientate the base plate efficiently, the position of the slots for the reference calibration pillars were rotated so that they were in line with the hexapod's coordinate system (i.e. 2 calibration pillars placed laterally on either side of the foot, as well as anterior/ posterior to the foot on the base plate – See Figure 28).

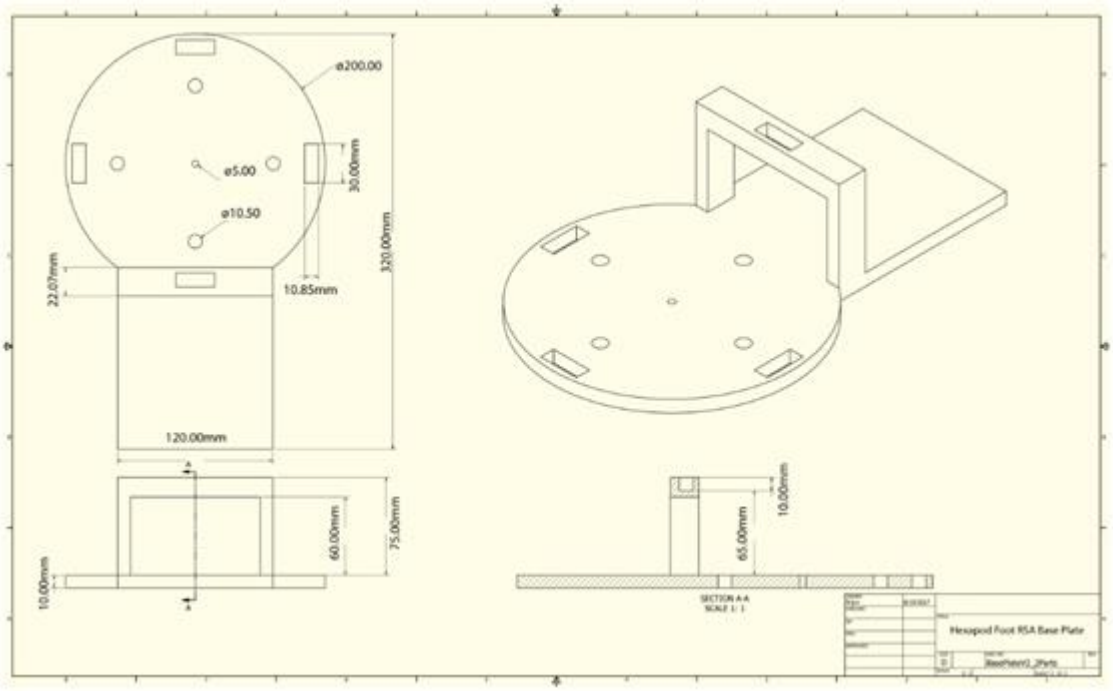

Figure 28: Base Plate Calibration Cage Design Modifications I

For the radiopaque spacer/base pillar, one option was to fabricate this as a separate component which bolts to the hexapod robot, as well as to the current base plate calibration frame. As this would result in unwanted compliance between the two parts as movements of the specimen are

simulated within the hexapod. As such, this spacer component was adapted to the existing design such that the final calibration frame and spacer could be fabricated as one part.

During the re-design of the full calibration frame with the attached spacer (Figure 29-32), it was decided that the height of the front arch of the base plate, holding the front RSA calibration pillar should be increased in height to allow bigger feet to fit on the top plate as well. As the tantalum markers on the reference rods had to line up in order to form the reference 3 dimensional coordinate system upon digitization of the stereo-radiographs, as the height of the front arch was increased, the length of the front calibration rod was reduced to keep the positons of the reference markers at the same geometric positions.

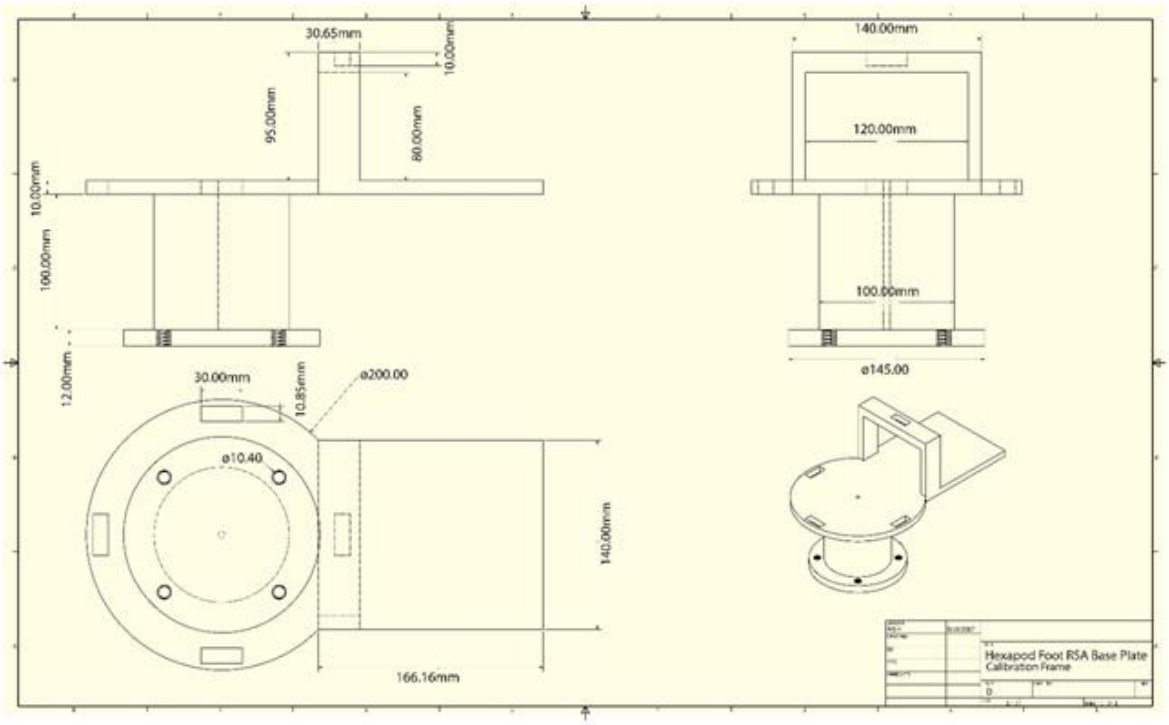

Figure 29: Final Base Plate Calibration Cage Design

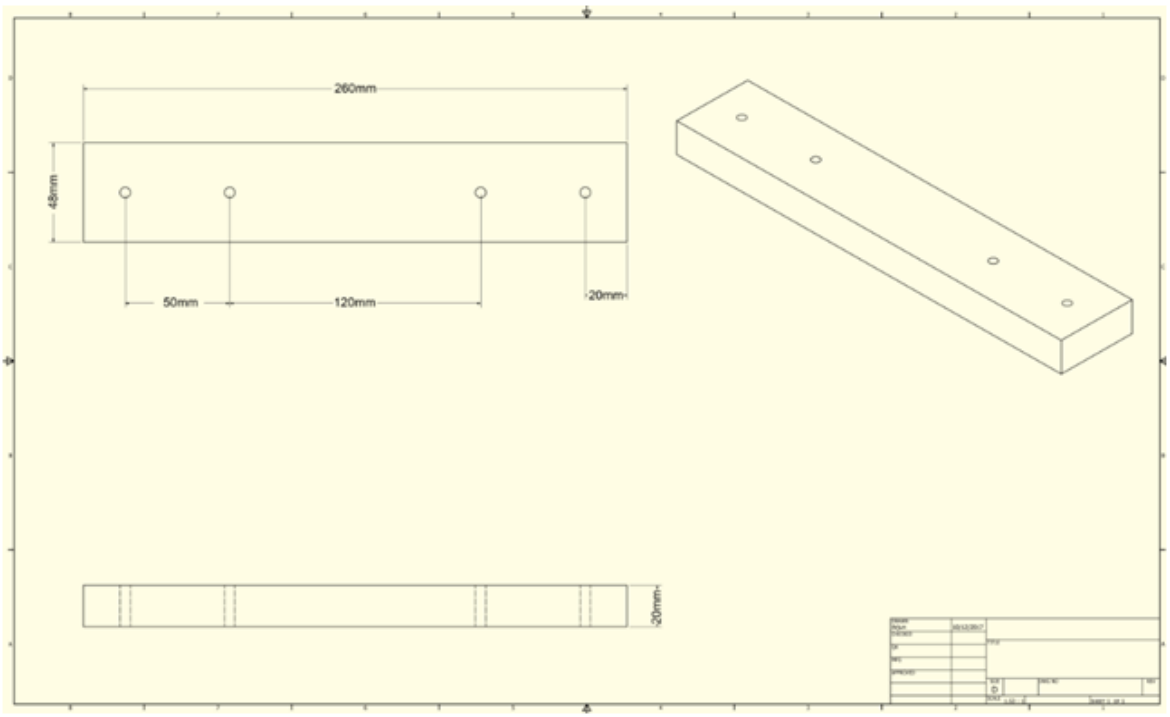

Figure 30: Final Base Plate Calibration Cage Design: x-ray cassette holder mounting bar

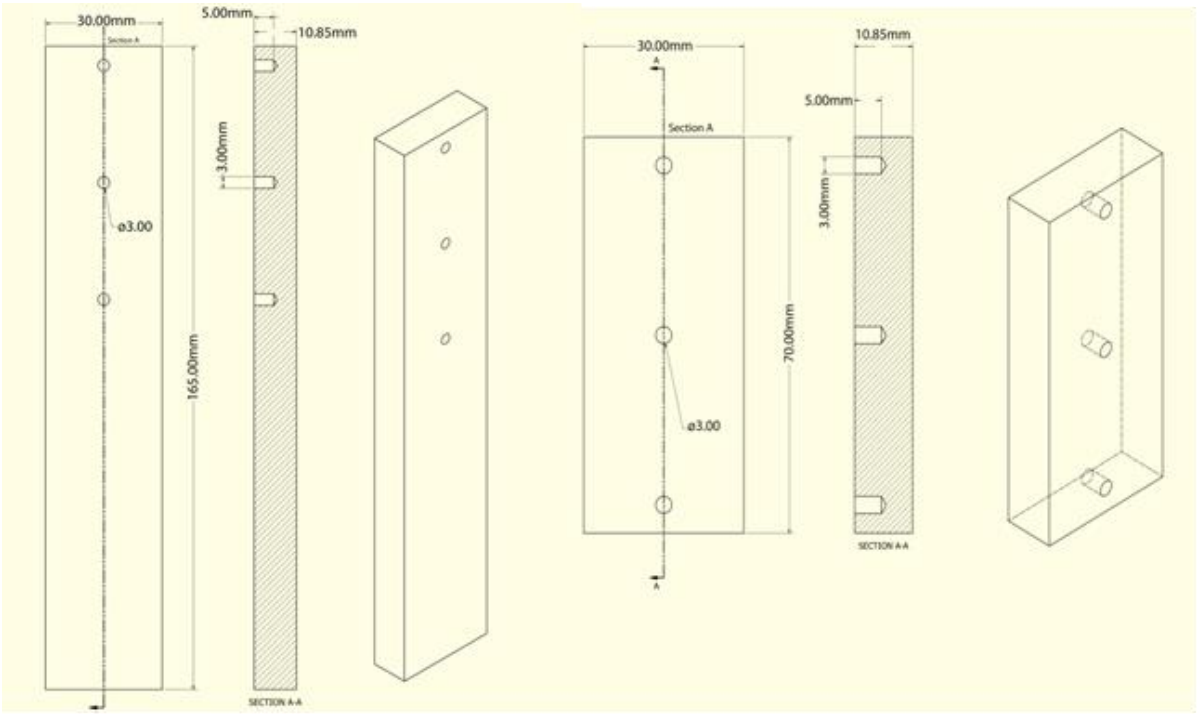

Figure 31: Final Base Plate Calibration Cage Design: Calibration Rods

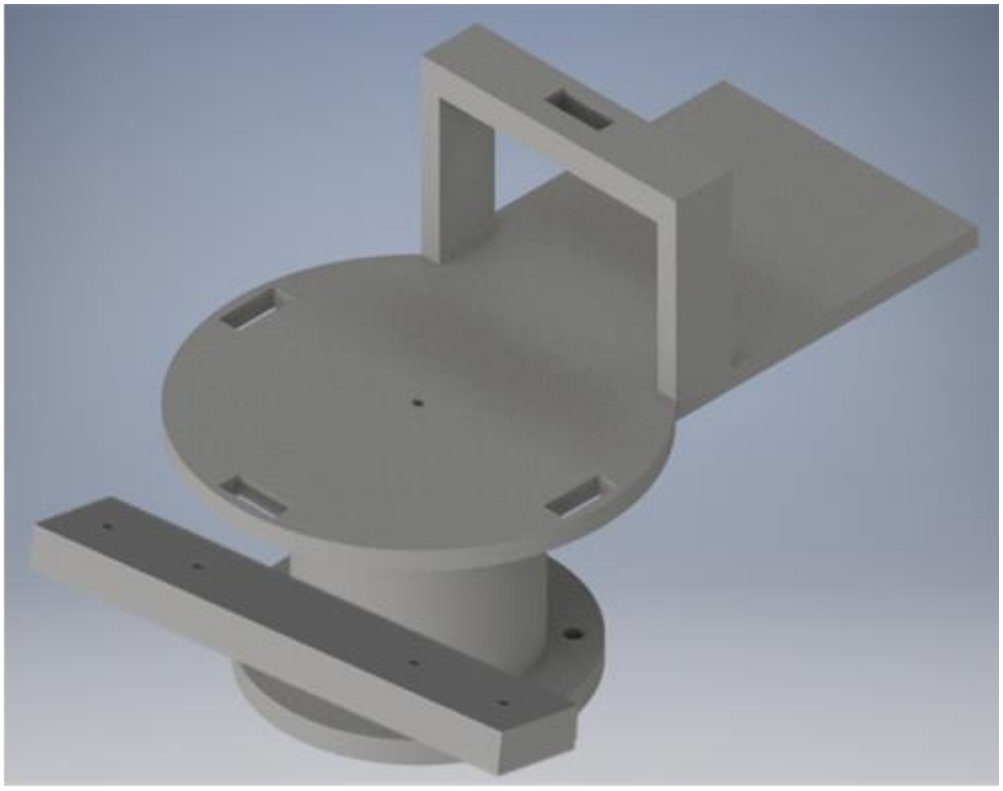

Figure 32: Final Base Plate Calibration Cage Design

4.4.5 Manufacture of Calibration Frame

Once the design had been completed and was ready for manufacture, there were several important aspects to consider prior to fabrication of the design. It was critical that the base plate calibration frame be made of a radio-transparent material such that the design itself didn't obstruct the view of any of the markers lying with the RSA calibration frame. It was also important that the surface of the base plate's top plate have a slight material surface roughness such that the bottom of the foot specimen could remain unconstrained to the base plate (allowing the foot to naturally splay out as the deformity is produced) whilst minimizing slip of the specimen on the surface of the plate. Upon these considerations, acrylic and ABS were both suitable materials for the design, both of which were used in the fabrication of the full base plate calibration frame.

To ensure the calibration rods were perpendicular to the base plate, an additional component was designed via CAD (Autodesk inventor) and 3D printed to serve as a flat platform for the bottom of the calibration rods which lay within the slots. This allowed the base of the rod to lay square with the flat platform.

4.4.5.1 Method

To fabricate the full base plate RSA frame (Figure 34 – 35), the design had to be manufactured in components and assembled.

The central column of the design, the x-ray cassette mounting bar and the 4 RSA calibration rods were laser cut in acrylic from the digital CAD files using a Rayjet 300 laser cutter.

The top surface plate of the base plate, and the front bridge (to accommodate the front-most calibration rod), were 3D printed in ABS using an Ultimaker 2+ 3D printer. Due to the large size of the base plate's top plate, and the limited size of the Ultimaker 2+ build platform, the top plate was printed in 2 parts; one part supporting the hindfoot of the specimen, and the other supporting the forefoot. An interlocking assembly design was adapted to the attachment ends of the 3 parts to be 3D printed to provide additional fixation strength of the top plate and resistance to deflection. These parts were then assembled together and a high strength adhesive used to secure the components of the top plate in place. Additionally, threaded holes were tapped into the top of the acrylic column and nylon bolts (radio-transparent) used to firmly fasten the top plate to the column.

Threaded holes were also tapped in specific positions of the mounting bar to allow a set of previously designed x-ray cassette holders (3D printed in ABS) to sit upon the mounting bar, thus allowing stereoradiographs to be consistently captured at the desired angle. The exact point positions of these threaded holes were included in the CAD files of the design and the points engraved by the laser cutter. Threaded holes were also tapped vertically along the base of the column as well on the x-ray mounting bar such that the bar could be firmly fastened to the back of the column. This was an important feature of the design in two aspects.

The distance between the x-ray cassette mounting bar and the top plate of the base plate had to be a certain height such that the x-ray cassettes were able to capture all of the markers lying within the RSA calibration frame during testing. Additionally, the x-ray cassette mounting bar had to be securely fixed to the column of the base plate such that during testing, the x-ray cassettes could be moved between the left and right cassette holders without movement of the bar occurring, thus ensuring consistency in the radiographs obtained. These distances were included in the CAD files and points where threaded holes were to be tapped were engraved

by the laser cutter. Nylon bolts were then used to fasten the x-ray cassette mounting bar to the column.

4.4.6 Positioning of RSA reference rods

For the digitization of the tantalum markers from the Stereoradiographs, it was critical for the RSA reference pillars to be in designated positions. This was so that each reference pillar could be individually identified from the Stereoradiographs, thus allowing the 3 markers on each calibration rod to be digitized in order. In doing this, the 3D digital coordinate system could be initialized and calibrated from the sequential digitization of each calibration marker. Referring to figure 33, the ∆ and x pillars placed posterior and anterior to the foot specimen initialized the digital X axis, while the □ and o Pillars placed laterally to the foot specimen initialized the digital Y axis. The vertical beads on the reference pillar initialized the digital Z axis, with the intersection point of the middle bead from all 4 pillars to correspond to the digitally reconstructed position in 3D space of $X,Y,Z = 0,0,0$. As this aspect was critical in the effective function of the final base pillar/calibration frame, the fundamental notions of the digitization and 3D transformation Matlab script was integrated into the base pillars design.

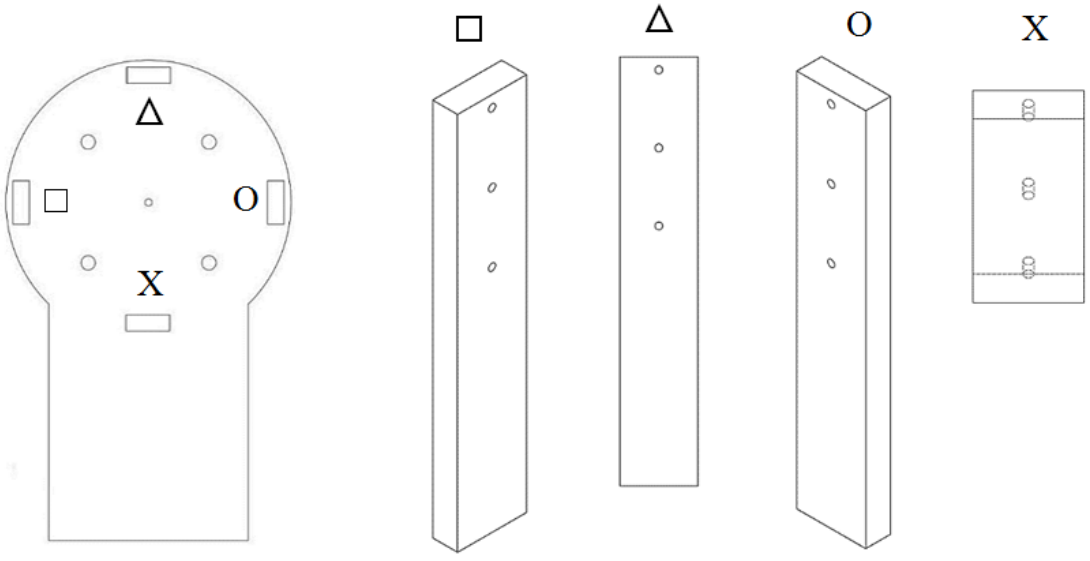

Figure 33: Positioning of RSA Calibration Rods

4.4.7 Final Base Plate Calibration Frame

Figure 34 and 35 exemplify the final assembled base plate calibration frame.

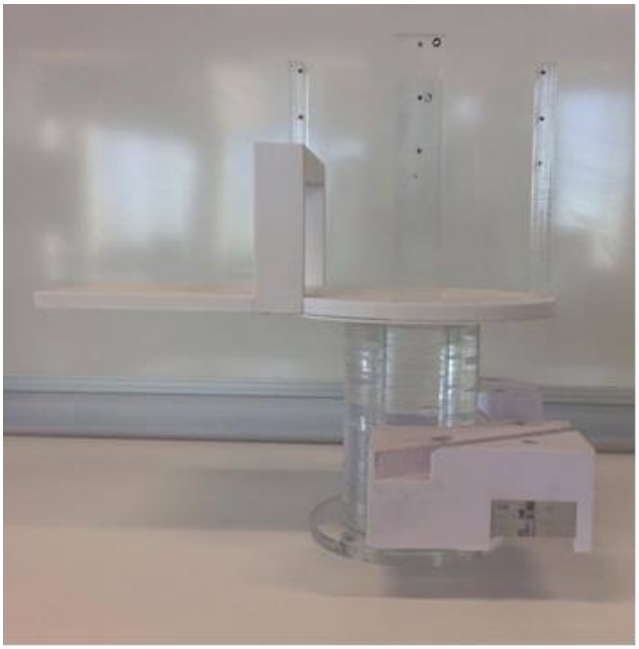

Figure 34: Final Manufactured Base Plate Calibration Cage: Side View

Figure 35: Final Manufactured Base Plate Calibration Cage: Anterior and Posterior View

After assembly of the RSA reference jig, the physical locations of the reference beads were re-measured with venieer calipers to be used for the digital calibration of the system (detailed in section 4.7.1).

4.5 RSA Bead Placement

Through several clinical, medical and biomechanical studies, the ligaments which known to experience deterioration (i.e. microtears within the ligament structure) and thus contribute to the pathology of AAFD have been established(Deland et al. 2005; Braito et al. 2016). The primary static stabilizing structures of have been identified as being the Spring ligament complex, talocalcaneal ligament and deltoid ligament complex (Deland et al. 2005; Pinney & Lin 2006; Lever & Hennessy 2016; Braito et al. 2016).

To observe the behavior and hence quantify displacement and strain of the static stabilizing ligaments, tantalum markers were placed as close as possible to the anatomic attachment sites of the primary support ligaments of the medial column (deltoid, spring, medial talocalcaneal, cuneonavicular & plantar tarsometatarsal ligaments) with a pair of beads marking the ends of a ligament, such that the average strain across the ligament could be measured (Butler et al. 1992; Fleming & Beynnon 2004). As the position of a flatfoot is progressively produced, the displacement of the ligaments of interest can be found through examining the displacements of a ‘bead pair’ at the attachment sites of a particular ligament. For this project, the behavior of the static stabilizers was of interest, as such, the posterior tibial tendon (dynamic stabilizer) was sectioned during the preparation of the specimens.

4.5.1 Objectives of bead positioning

With the primary static stabilizing ligaments identified as the deltoid ligament complex, spring ligament, talocalcaneal ligament, cuneonavicular and plantar tarsometatarsal ligaments, beads were to be placed at the attachment sites of these ligaments, while minimizing the number of beads used. This was due to the fact that if the specimen contained too many beads, the

captured radiographs would detect the dense arrangement of tantalum markers, thus making each individual feature harder to distinguish, and hence ligament, more difficult to identify during the digitization process.

An additional consideration regarding placement of the beads was the dense anatomical structure of the foot and ankle. The beads were to be placed as close as possible to the attachment sites of the ligaments to be tracked, whilst maintaining as much structural integrity of the foot and its constituent soft tissues as possible.

With this in mind, the objectives of the placement of the beads were as follows:

1. The beads were to sit on the anatomic bony landmark attachment sites of the supporting structures of the medial column ligaments
    - *Deltoid ligament complex (posterior tibiotalar, tibiocalcaneal, tibionavicular, anterior tibiotalar parts)*
    - *Spring ligament (plantar calcaneonavicular ligament)*
    - *Talocalcaneal ligament (medial and posterior tibiocalcaneal)*
    - *Cuneonavicular ligament*
    - *Plantar tarsometatarsal ligament (1st metatarsal)*
2. The number of beads placed within the foot was to be minimized for efficient identification of the markers in digital post processing.
3. Except for the posterior tibial tendon (dynamic stabilizer - sectioned), care was to be taken to ensure all other ligament structures are left intact.

4.5.2 Conceptualization of Bead Placement

To address these requirements and allow for the ligaments of interest to be analyzed, beads were assigned to the following ligaments:

Deltoid Ligament

- Posterior tibiotalar part
- Tibiocalcaneal part
- Tibionavicular part
- Anterior tibiotalar part
- Tibiospring ligament
- Spring ligament (calcaneonavicular)
- Medial talocalcaneal ligament
- Plantar cuneonavicular ligament
- Plantar fascia (additional)

Markers were then added to the anatomic diagram of the medial ankle to represent the designated positions of the tantalum markers.

From the anatomical diagram, components of the deltoid ligament were marked by the 3 beads at the distal tibia, with 1 bead at each of the attachment sites of the 5 components of the deltoid ligament (*posterior tibiotalar part, tibiocalcaneal part, tibionavicular part, anterior tibiotalar part and tibiospring part*). (8 beads total)

The spring ligament, medial talocalcaneal, plantar cuneonavicular and plantar fascia ligaments were marked by a pair of beads, one at each attachment site of the ligament.

Deltoid Ligament

- Posterior tibiotalar part (beads 3 - 4)
- Tibiocalcaneal part (beads 1 - 5)
- Tibionavicular part(beads 1 - 9)
- Anterior tibiotalar part(beads 2 - 7)
- Tibiospring ligament(beads 1 - 6)

Spring ligament (calcaneonavicular) (beads 5 - 6)
Medial talocalcaneal ligament (beads 5 - 4)
Plantar cuneonavicular ligament (beads 9 - 10)
Plantar fascia (additional) (beads 11 - 12)

[Figure has been removed due to copyright restrictions]

Figure 36: Initial bead placement positions and bead paring (ligaments)

4.5.3 Pilot Bead Implantation & Changes to Specimen Bead Placement Protocol

As the foot the ankle is an anatomically dense structure, and the anatomical structures displayed in 2D textbook diagrams is very different to a physical 3D scenario, it was important to verify the proposed placement locations and specimen preparation method through dissection and implantation of the markers in a pilot foot specimen (Figure 37). An orthopaedic foot and ankle surgeon carried out the implantation of the tantalum in the pilot foot specimen.

Figure 37: Pilot Implantation in Cadaveric Foot

From the process of dissecting and implanting tantalum markers in the proposed locations, challenges were met in implanting the beads at the attachment sites of the ligaments without damaging any other structures in the process. This was due to the fact that the 2-dimensional images in textbook anatomy displayed a much simpler representation of the structures and landmarks within the foot. Due to the dense anatomical arrangement through the physical dissection, several changes were made to the bead placement protocol upon discussion with a foot and ankle specialist. Additionally, upon gaining familiarity with the 3-dimensional anatomy of the foot and ankle in a cadaveric model, several additional beads were added to the bead placement protocol to most effectively monitor the behavior of the ligaments of interest, whilst remaining minimally invasive to the supporting soft tissue structures.

Of the changes to the bead positions, the locations of most of the beads remained unchanged, with modifications to the numbering of some of these markers as several extra markers were added. From the original bead position diagram, beads numbered 1, 2 and 3 on the distal tibia, bead 4 on the posterior process of the talus, bead 7 at the distal side of the tibiotalar joint, bead 9 on the navicular bone, bead 11 on the 1st metatarsal, and bead 12 at the back of the calcaneus remained unchanged. The following modifications were then made to the bead placement protocol:

- Bead 5 is moved posteriorly towards the back of the sustentaculum tali
- Another bead was added to the anterior end of the sustentaculum tali
- Bead 6 was moved to the plantar attachment site of the spring ligament (lateral attachment site)

- Another bead was added at the attachment site of the plantar spring ligament (medial attachment site)
- A bead was added to the medial cuneiform bone (plantar side)
- A bead was added to the proximal end of the 1st metatarsal (plantar side)

4.5.4 Final bead placement

With the modifications to the positions of the tantalum beads, the visual representation of the markers positions served by the anatomic diagram was modified as follows;

[Figure has been removed due to copyright restrictions]

Figure 38: Amended Bead Placement Positions

Table 7: Bead Pairs for Corresponding Ligaments

Deltoid Ligament	**Spring Ligament (calcaneonavicular)**
• Posterior tibiotalar part (beads 3 - 4) • Tibiocalcaneal part (beads 1 – 5) • Tibionavicular part (beads 1 - 6) • Anterior tibiotalar part (beads 2 - 7) • Tibiospring ligament (beads 1 - 10) Medial talocalcaneal ligament (beads 5 - 4**)**	• Superomedial part (beads 8 – 10) • Inferior part (beads 8 – 9) Plantar cuneonavicular ligament (beads 10 - 11) Plantar cuneometatarsal ligament (beads 11 - 12) Interosseous ligament (indirect) (beads 8 – 7) Plantar fascia (additional) (beads 13 - 14)

4.5.5 Specimen preparation and bead implantation procedure

An orthopaedic foot and ankle surgeon carried out the implantation of the tantalum beads in their designated anatomic locations (Figure 39).

1

Cadaver Ankle Specimen – Thawed for 24 Hours

2

Mark Medial Malleous & lines for flap

3

Cut along lines and carefully 'skin'' the flap, maintaining cut on the fat tissue plane.

4

The PTT is visibile. The flexor digitorum longus (FDL) is seen posterior to the PTT

5

Section the PTT from the navicular insertion

6

Idenfify medial maleoulus, mark beads 1,2,3 - Bead 1 is in the middle of the maleoulus, beads 2 and 3 are 1.5cm away from bead 1 and at a 45 degree angle.

7

Bead 4 is placed on the posterior process of the talus

8

The Sustentaculum tali is identified, bead 5 is placed at the posterior end of the process.

9

Bead 8 is placed on the sustentaculum tali, anterior to bead 5

10

Beads Bead 9 is placed on the plantar attachment of the spring ligament

11

Bead 10 – placed anterior to bead 8, on the plantar part of the foot - Spring Ligament plantar attachment

12

Bead 11 placed on the plantar part of the cuneiform

13

Bead 11 – Plantar part of cuneiform

14

Bead 7 – placed on the top of the talus

15

Bead 12 – Plantar part of the proximal Metatarsal

16

Bead 13 – Plantar part of the distal metatarsal

17

Suture access flap back up.

18

For adequate tibia potting fixation, 70cm of tibia must be exposed with all soft tissue removed.

Figure 39: Implantation of Markers in Cadaveric Foot

4.6 Achilles Tendon Tension

In preparation of the ankle specimens, one important aspect to consider was the tension applied to the Achilles tendon. Within the human body, the foot and ankle is capable of rapidly transforming from a flexible mobile adapter to a rigid adapter when required, to most effectively generate movement on even and uneven surfaces (Jarvis, 2014). To do so, the natural physiological tension through the Achilles tendon allows the plantar fascia, a dynamic stabilizer of the arch of the foot, to tighten and adequately distribute ground reaction forces through the structures of the foot and ankle during the stages of gait (Bolgla & Malone 2004; Bonnefoy-Mazure & Armand 2015).

The longitudinal arch of the foot is comprised of a four-layer load sharing system that is made up of the plantar fascia, plantar intrinsic and extrinsic muscles, as well as the plantar ligaments (Kirby, 2017). As stated by Kirby (2017), the passive tension load-bearing elements of this load sharing system (plantar fascia and plantar ligaments) are not under direct control of the central nervous system and "serve to stiffen the longitudinal arch with an automatic stiffening mechanism that is based on Achilles tendon tension and plantar forefoot loading" (Kirby, 2017). Moreover, as understood in the physiological mechanisms of gait, dorsiflexion of the ankle, which allows the body to pass over the foot, is an essential step of the gait cycle (Bolgla, 2004). As stated by Bolgla (2004), "A tight Achilles tendon limits the amount of dorsiflexion available during gait". Anatomically, the collagen fibres of the Achilles tendon pass around the posterior of the calcaneus and wrap to the superficial layers of the plantar fascia (Bolgla, 2004). Positive correlations between tension of the Achilles tension and the plantar fascia have been found in literature (Cheung et al, 2006), through which a tightening of the plantar fascia heightens the medial longitudinal arch by reducing the distance between the metatarsals and the calcaneus (Bolgla, 2004).

As such, it is important to provide tension in the Achilles tendon so that the tarsal bones are tightened together, maintaining the physiological form of the arch and resisting a collapse due to excessive flexibility of the arch.

Initially, the design of a mechanical loading frame was considered to apply a constant vertical tension through the Achilles tendon, independent to the forces exerted upon the foot under control of the hexapod robot. The magnitude of which was to be similar to the physiological tension force experienced by the tendon in the human body. This would have required careful

conceptualization, design of a mechanical pulley system and involve the use of a data acquisition system to monitor the applied tension through the Achilles tendon in real-time. As this would have added another component to the project, and with the time constraints of a one year project, this design aspect of the project was deemed unfeasible and not able to be included in this project. In addition to this, as the project aimed to produce a physiological change in position and investigate the behavior of the ligaments as this position was induced, the design of a full physiological 'constant tension' system was not included in this project.

However, in order to produce flexion of the plantar fascia, and replicate the physiological tension within the longitudinal arch of foot as observed in the human body, it was critical for some tension to be applied through the Achilles tendon. With this in mind, two methods of maintaining tension to the Achilles tendon were considered:

- Applying a nominal tension through Achilles and pinning the tendon to the tibia.
- Applying a nominal tension through the Achilles using a wire attached to the top cup used to pot the specimen (attached to the S*pecimen Coupling Plate* of the Hexapod Robot).

Upon consideration of these two methods, along with the fact that with some specimens coming from older donors possibly had osteoporotic bone, it was concluded that pinning the tensioned achilles tendon to the tibia was not the optimum approach for the specimens at hand and the latter method was implemented.

4.6.1 Nominal Tension Achilles – top cup

To apply the tension through the achilles tendon the tendon was first exposed by making an incision down the back of the foot along the superficial layer of the tissue. A non-biodegradable high tensile strength suture was then threaded along the Achilles tendon (Figure 40). A wire was then to be attached to this suture and tightened to specimen top cup when potting the specimen.

Figure 40: Sutured Achilles Tendon for Tension

4.7 Stereometric X-Ray Digitization & Transformation Code

In order for the designed baseplate/RSA Calibration frame to effectively function with the digitization and 3D transformation MATLAB script also developed, measurements for the vertical positions of the 3 reference markers on each of the 4 calibration rods needed to be taken and implemented into the MATLAB script to calibrate digitation/transformation process. This was such that when a set of left and right X-Rays (stereoradiographs) (capture setup depicted in Figure 41) were digitized using the script, the reference marker positions could be detected with their distances known. These were then converted to reference coordinates which in turn initialize a digital reference X, Y and Z axis coordinate system.

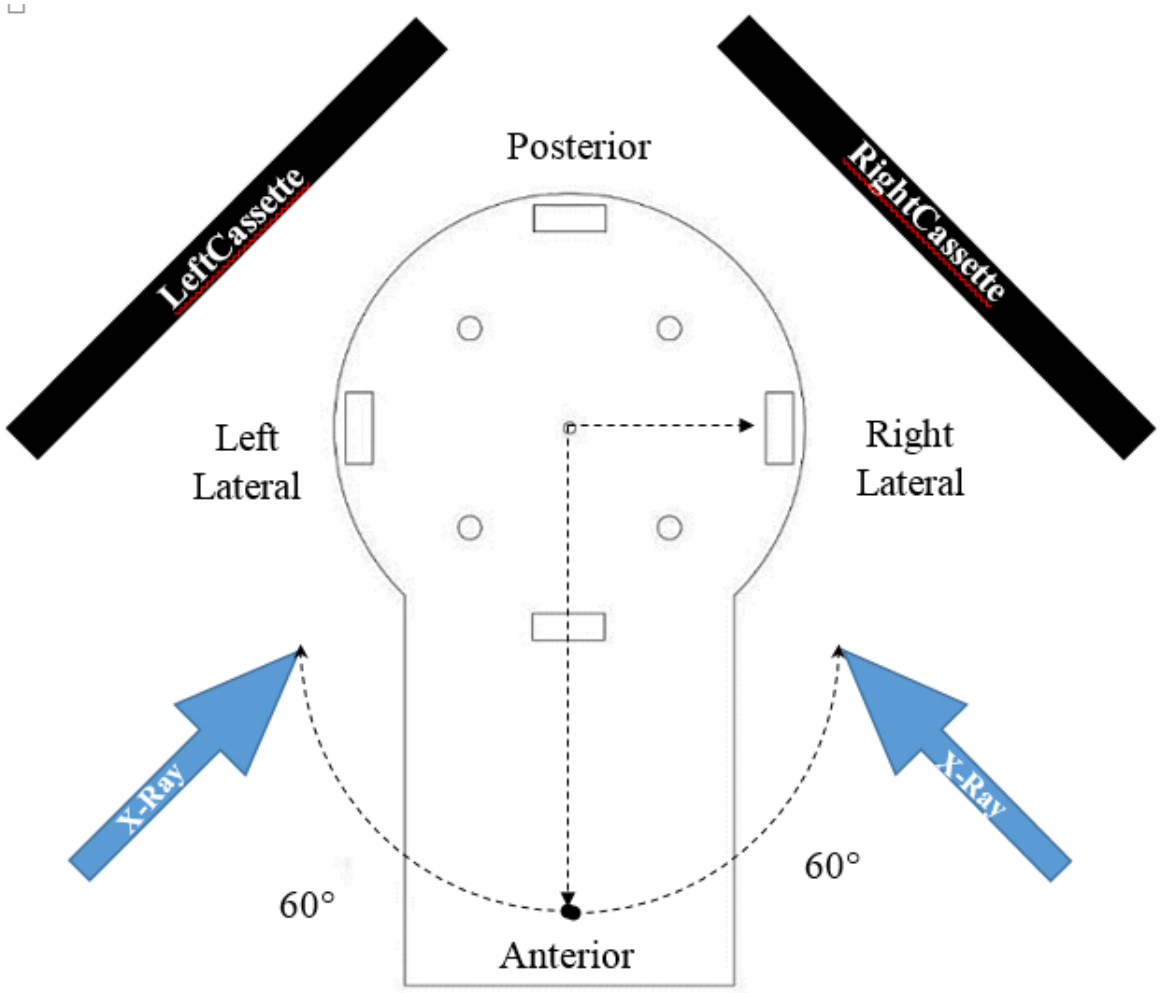

Figure 41: RSA - Stereoradiograph capture setup

4.7.1 Calibration of the RSA frame pillar

To calibrate the digital system, physical measurements of the position of each calibration bead (3 beads on each RSA calibration rod) needed to be taken for each of the 4 calibration rods (Figure 42).

The position of each calibration bead (from the bottom of the base plate) was measured three times and the distances averaged (Table 8).

Table 8: Average Measured Position of Each Calibration Bead from Bottom of Base Plate

	Distance from bottom of Base Plate (mm)							
Pillars	**Square**		**Triangle**		**Circle**		**X**	
Top Bead	159.2	160.2	160.2	160.3	159.9	159.9	160.4	160.3
Average	*159.7*		*160.3*		*159.9*		*160.4*	
Middle Bead	130.1	130.4	129.9	129.8	130.0	129.9	130.0	129.9
Average	*130.3*		*129.9*		*130.0*		*130.0*	
Bottom Bead	99.6	100.1	99.6	99.7	99.7	100.1	99.9	99.9
Average	*99.8*		*99.7*		*99.9*		*99.9*	

As mentioned in Section 4.4.6, The *0,0,0* coordinate point of the digital coordinate system (generated from the digitization of a set of stereoradiographs via the MATLAB script)was initialized as the intersection point of the lines drawn from the each of the middle beads (of the 4 calibration pillars). Due to this, the measured distances of each bead were converted to X, Y, Z coordinates, relative to this intersection point of the middle calibration beads (Table 9).

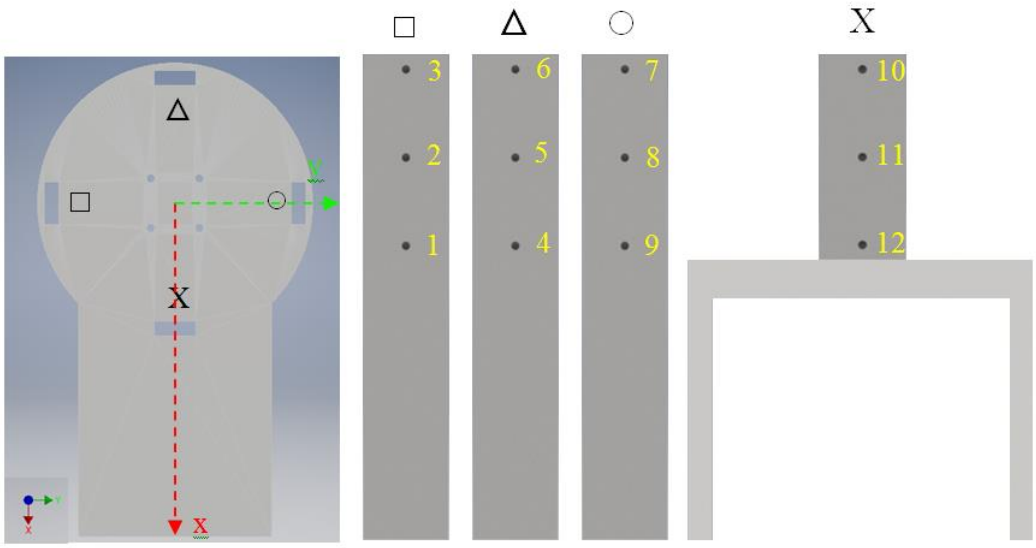

Figure 42: RSA Calibration Rods: Reference Bead Identification

Converting the bead positions to coordinates relative to the digital 0, 0, 0 coordinate position, formed by the intersection of the horizontal lines drawn from the middle beads.

Table 9: Average Measured Coordinate Positions of Each Calibration Bead

Bead No.	X (mm)	Y (mm)	Z (mm)
1	0	-89.3	-30.5
2	0	-89.3	0
3	0	-89.3	29.4
4	-89.2	0	-30.2
5	-89.2	0	0
6	-89.2	0	30.4
7	0	89.2	29.9
8	0	89.2	0
9	0	89.2	-30.1
10	89.3	0	30.4
11	89.3	0	0
12	89.3	0	-30.1

These coordinates were then written to a configuration file upon which the RSA transformation script would call upon to determine coordinate positions (*mm*) for the markers lying within the RSA Calibration frame.

4.8 Validation Test: Error Measurement of Calibration Frame

To validate the accuracy of the RSA digitization system, several tantalum markers were to be placed within the designed baseplate/RSA calibration frame at known positions such that the X, Y, Z coordinates for each marker could be measured. These measured (known X,Y,Z) coordinate positons, for each marker could then be compared to the digitally calculated X,Y,Z coordinates obtained from the digitization and transformation of left and right stereo X-Rays. From the comparison of the measured (known) coordinate positions with the RSA coordinates, the function of the RSA base plate calibration frame system could be validated and its accuracy in reconstructing positions in 3D determined.

4.8.1 Method

In order to do this, a mock foot was digitally designed in Autodesk Inventor (CAD) (Figure 43) and 3D printed in ABS with an Ultimaker 2+ (UM2+). The base of the ABS mock foot consisted of 4 circular extrusions which lined up with the centralized circular holes on the top

surface of the designed baseplate/RSA calibration frame. From slotting into these holes, the point at which the validation block lined up with the center of the base plate (X, Y, Z coordinates of 0, 0, and 0) could be established and was digitally indented with an extra point for identification.

Within the digital design, 4 points were inscribed into of the mock foot at locations roughly similar to that of where markers were implanted in the cadaveric feet. Once 3D printed, 4 tantalum markers were then carefully embedded and glued at each of these 4 indented points. When the mock foot was slotted into place on the base plate, the 0, 0, 0point indentation of the validation block aligned centrally with the middle of the base plate and could be identified. Measurements could be made of each of the each of the 4 known marker locations. These were then converted to X, Y, Z coordinates relative to the 0, 0, and 0 position initialized by the central intersection point of the middle bead from each of the 4 reference pillars (corresponding with the central point on of the base plate).

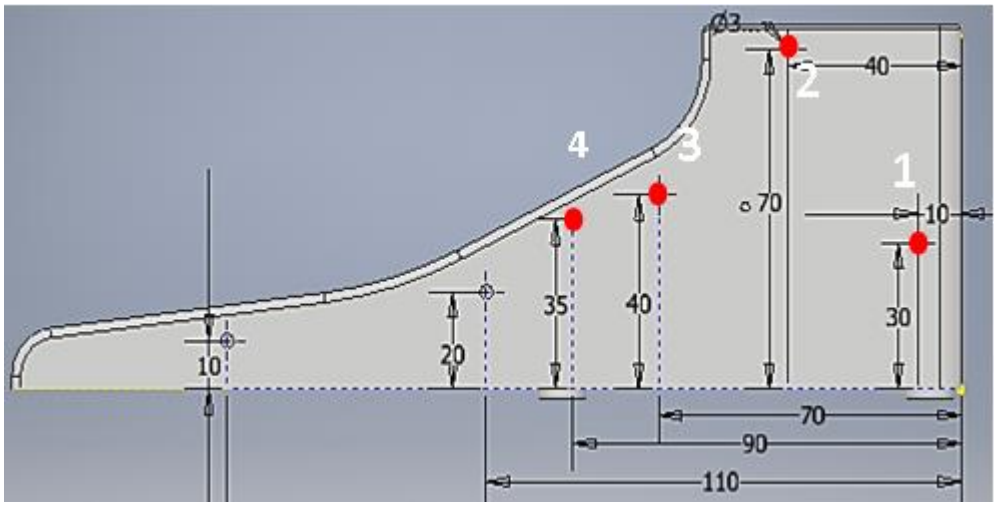

Figure 43: Mock foot with beads (1-4) in known positions

Once the 3D printed mock foot was slotted into the centrally aligned holes of the base plate RSA frame,

Once the 3D printed mock foot was slotted into the centrally aligned holes of the base plate RSA frame, physical measurements each of the 4 marker locations were taken with venier calipers. These physical measurements were preferred over digital coordinate positions in Autodesk inventor as it took into account any errors introduced by the Ultimaker 3D printer as it printed curved surfaces.

Following this, the base plate calibration frame was mounted into the hexapod and left and right stereo X-rays taken (Figure 44).

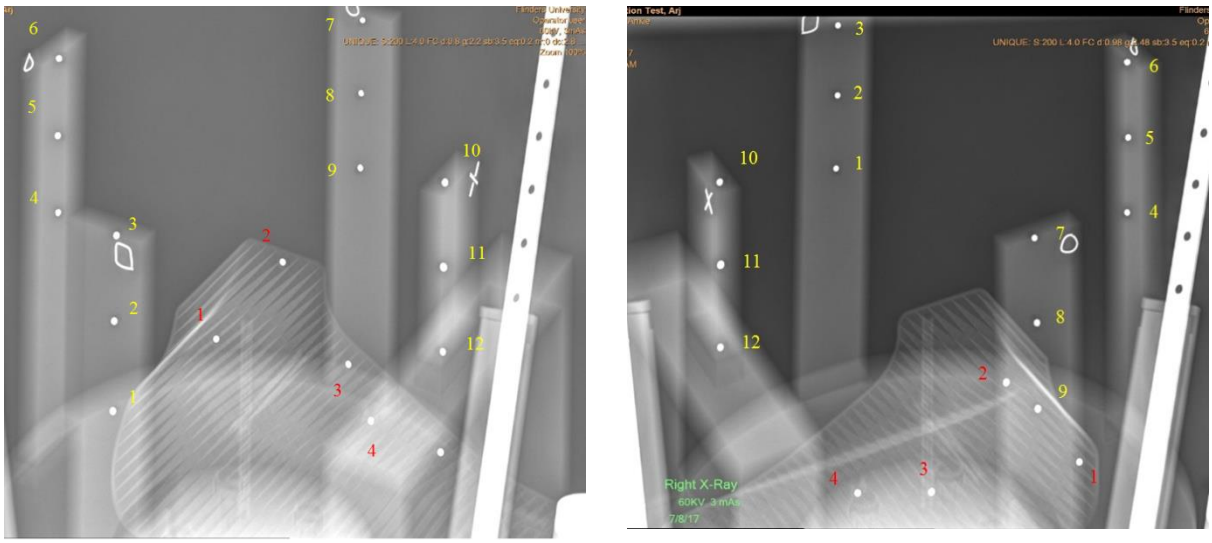

Figure 44: Left and Right Stereoradiographs of 3D printed Mock Foot

The left and right Stereoradiographs were then digitized via the MATLAB program to calculate coordinate positions for each of the 4 markers with reference to the 0,0,0 point initialized by the intersection point of the line drawn from the middle bead from each of the 4 calibration rods.

4.8.2 Results

Based on the measurements taken of the positions for each of the 4 markers, the exact theoretical coordinate positions for each of the four markers were as follows (see table 10).

Table 10: Measured Coordinate Positions of Beads in Mock Foot

Marker	X (mm)	Y (mm)	Z (mm)
1	-40.0	44.0	-87.0
2	-10.0	44.0	-48.0
3	20	44.0	-78.0
4	-41.0	25.0	-81.0

Through digitization and 3D reconstruction of the markers with the developed RSA script, the following coordinate positions were calculated by the system (Table 11).

Table 11: RSA Coordinate Positions of Beads in Mock Foot from Stereoradiographs

Marker	X (mm)	Y (mm)	Z (mm)
1	-41.87	44.67	-86.09
2	-10.61	44.63	-47.96
3	20.7	44.73	-77.79
4	-42.25	25.91	-82.37

Upon comparison of the known theoretical positions with the digitized positions, the absolute displacement error can be calculated for each marker (Table 12).

$$Absolute\ error = pos_{known} - pos_{experimental}$$

Table 12: Absolute error (mm) between measured and RSA calculated beads positions

Marker	X (mm)	Y (mm)	Z (mm)
1	1.87	0.67	0.91
2	0.61	0.63	0.04
3	0.70	0.73	0.21
4	1.25	0.91	1.37
Average	1.108	0.735	0.633

From the average absolute displacement uncertainties shown above, the relative uncertainty of measurement compared to the size of the measurement can be calculated (relative error) (Table 13).

$$Relative\ error = \frac{Absolute\ error}{pos_{known}}$$

Table 13: Relative error between measured and RSA calculated beads positions

Marker	X (mm)	Y (mm)	Z (mm)
1	0.04675	0.0152	0.0105
2	0.061	0.0143	0.0008
3	0.035	0.0166	0.0027
4	0.03048	0.0364	0.0169
Average	0.043308	0.020625	0.007725

4.9 Data Collection

For each of the specimens tested, stereoradiographs were captured at each of the incremental loadsteps applied (i.e. Initial, 100N, 230N, 460N, 690N, 920N). From each set of the captured stereoradiographs, the markers implanted at the attachment sites of the ligaments could be seen.

For each specimen, the stereoradiographs at each loadstep had to be digitized by the developed MATLAB script in order to form a 3D reconstruction of the radiographs. This was essential in order to elicit coordinate position data for each of the markers at each loadstep.

From comparing the position data of each marker at the incremental loadsteps (i.e. from the original position to each sequential load), the displacement vectors of each marker, and their constituent X, Y and Z components could be calculated. As the markers were implanted at the attachment sites of the ligaments, through pairing corresponding beads together (refer to figure X), the original length, displacement and resulting strain response of the ligament could be calculated.

For the digitization of the left and right x-rays, it was important that all 3 tantalum markers on each of the 4 calibration reference rods were visibly evenly spaced in the vertical direction from one another on the radiographs. Additionally, the markers on the radiographs had to be visually clearly defined for the program to detect them. As such, to ensure efficient digitization, the x-rays were visually enhanced in post processing (Adobe Photoshop) by adjusting the sharpness, brightness and contrast to make the markers more visually defined. Additionally, if any calibration markers were visually obstructed in the radiographs by the physical dimensions of the hexapod robot, these markers were aligned and interpolated using Adobe Photoshop's ruler & measurement tool. This could be done when for a given calibration rod, only 2 of the 3 reference markers were visible. In this process, the digital ruler tool was used to connect the centers of the visible two reference markers and measurement algorithm changed from the image pixel length, to the known distance between the reference markers on each calibration rod (30mm). The tool was then used to digitally replicate a visible calibration marker at the digitally measured position of the expected calibration marker.

Once the stereoradiographs for each specimen were run through the RSA digitization &, transformation program, the strain response values for each of the 11 ligaments at each of the 5 incremental loads (100N, 230N, 460N, 690N and 920N) were written to a text file.

4.10 Data Analysis

Once the strain values at each loadstep, for the 11 ligaments of interest were collected, the data was tabulated in an excel spreadsheet to document the results from the experiment. From this spreadsheet, average strains for each ligament, at each incremental loadstep across all of the specimens tested were calculated.

Within the data, as there were 5 loadsteps (conditions) under which the same 11 ligaments were straining, the study was of a repeated measure design. As such, SPSS (IBM) was be used to conduct a repeated measure 2-way analysis of variance (ANAOVA), which was optimal for the statistical analysis of the data. This is discussed further in the results section of the dissertation (See Chapter 7).

Chapter 5: Pilot Cadaveric Human Foot Testing - Simulation of Adult Flatfoot in Cadaveric Model with a 6DOF Hexapod Robot

Once the experimental design was completed, tested and validated in its several individual stages, a full pilot test was conducted with a cadaveric human foot specimen to integrate all aspects of the experimental design. This pilot test was essential in verifying the foot and ankle fixation method to the hexapod robot (potting), confirming the effectiveness of data collection (identification of the implanted markers via the stereo X-Rays) and efficiency of the RSA digitization & transformation MATLAB scripts developed to operate with the base plate calibration frame. For this pilot test, an unused left cadaveric foot specimen (obtained from the United Tissue Network, Oklahoma) available in the cadaver freezer of the biomechanics and implants laboratory was used.

5.1 Human Foot Preparation – Potting

In order to effectively mount the cadaveric specimen to the Hexapod Robot and apply the required loading conditions, the specimen needed to be prepared for testing by fixating the foot in a centrally aligned, plantigrade position via the tibia and fibula, to a 'top cup' which could then be attached to the 'Specimen Coupling Plate of the Hexapod Robot. The specimen to be used was removed from the freezer room and thawed for 24 hours prior to handling and preparation of the specimen to be tested.

The first step of preparing the specimen for testing was ensuring that the proximal tibia and fibula was exposed, with a majority of soft tissue removed from the bone. This was essential in minimizing the amount of mechanical give within the specimen/top cup fixation and thus ensuring that the force and position data both applied and recorded via the hexapod robot was as accurate as possible. The removal of the soft tissue from the tibia and fibula was carried out using a scalpel and forceps during the bead implantation preparation of the specimens.

Following this, proximal end of the specimen consisting of the tibia and fibula needed to be cut down slightly such that the distance from the talocrural joint to the proximal end of the

specimen measured roughly around ~200mm. This was important in ensuring that the specimen could be adequately mounted within the hexapod robot without the upper leg limits of the robots encoders being reached when forces were applied to the specimen, as this would record a system error and half the simulation. This was conducted by using a ruler and permanent marker to mark the approximate distance from the talocrural joint followed by using a bone saw to cut through the proximal end of the tibia and fibula.

Once the specimen had been cut down slightly, the top cup into which the proximal tibia & fibula were to be fixated in was attached to an 'alignment rig'. The purpose of the alignment rig was to align the foot centrally with the axis of the hexapod and thus simulate the position that the specimen would be in once mounted to the testing robot. The top cup was then prepared for potting the specimen by blocking off any excess threaded holes which wouldn't be occupied with tape. This stage was conducted within a vacuum chamber fume cupboard as the chemicals used to pot the specimen are harmful when inhaled. The foot specimen was then inverted with the forefoot (anterior foot) directed forwards and the tibia placed centrally inside the top cup. Care was taken to position the tibia vertically such that the talocrural joint of the ankle also lined up approximately with the center of the top cup.

Once placed within the top cup, 2 retort stands were used to hold and maintain this position – one to hold the position of the proximal foot within the cup, and the other to hold the front of the foot in a neutral plantigrade position (Figure 45). Several lubricated screws were then used to hold the tibia and fibula in place as well as to prevent any rotational movements of the bone cement (polymethyl-methacrylate (PMMA) to be used to fixate the specimen to the top cup. Once the specimen was secured in this position, self-curing PMMA powder and a PMMA liquid monomer agent were measured out separately in a ratio of 2.5mL powder to 1mL liquid. These were then combined into a mixing cup and stirred through to produce a regular form of the desired consistency. The PMMA mixture was then poured into the top cup and left to set for 30 minutes.

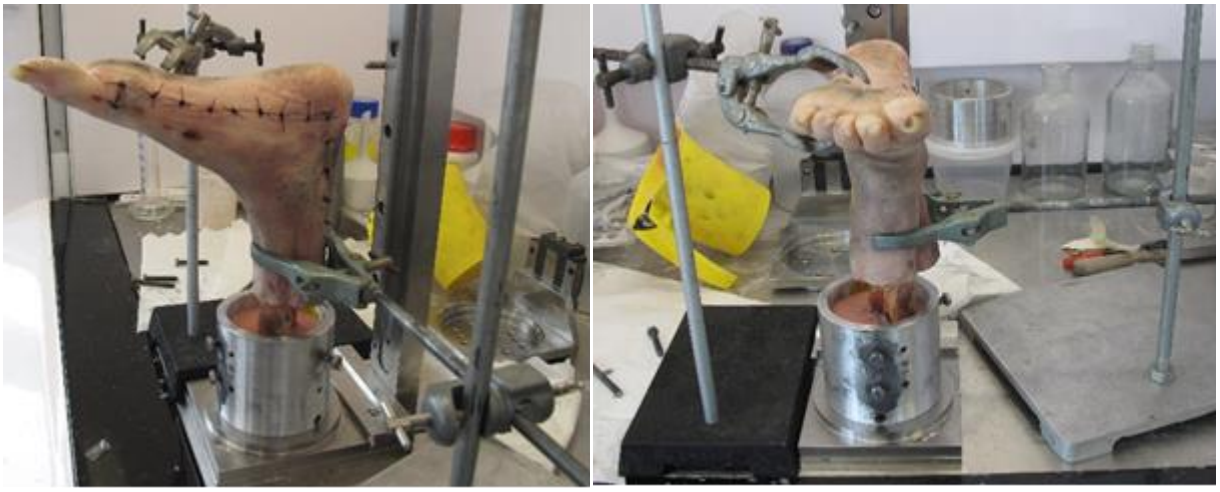

Figure 45: Potting (mounting preparation) of Cadaveric Foot

A full protocol for the preparation and potting of foot/ankle specimens was developed and is included in APPENDIX E. In this protocol, all steps involved in the potting and mounting of the specimen to the hexapod prior to testing are outlined.

5.2 Specimen Offset

Once the PMMA had set, the specimen was firmly secured to the top cup. Prior to mounting the specimen to the hexapod and exerting forces upon the specimen, X, Y and Z offsets for the axis of rotation (AoR) of the ankle joint needed to be determined relative to the center of the hexapod robots global coordinate system (GCS). For each specimen, it was required for this information to be inputted into the hexapod robots control system such that forces and moments could be applied to the foot about a known axis of rotation.

To determine the X, Y and Z offsets of the specimen's axis of rotation (talocrural joint), lateral and PA (posterior-anterior) X rays needed to be taken and measurements made digitally via the X-Ray system (*Philips DigitalDiagnost*). To do this, a radiopaque piece of material of known length needed to be captured in the X-Rays alongside the specimen so that it could be used as a measurement calibration tool. A lateral X-Ray was taken of the specimen to determine the Y and Z offsets of the AoR from the center of the hexapod's GCS, and a PA X-Ray was taken to determine the X offset (Figure 46).

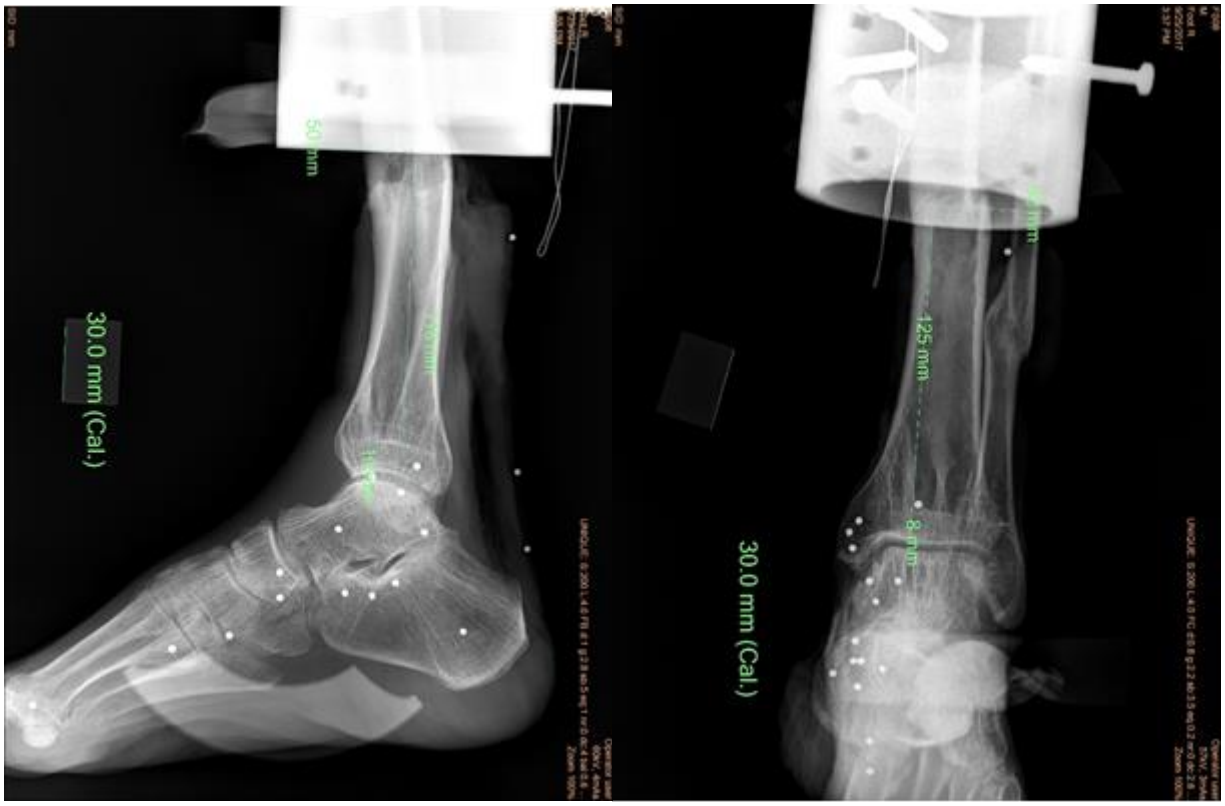

Figure 46: Lateral & PA x-rays to measure Axis of Rotation (Talocrural Joint) offset

After the X, Y and Z offsets for the AoR had been measured (Figure 46); the top cup was attached to an adaptor plate via several bolts which allowed the specimen to be coupled to the Specimen Coupling Plate (SCP) of the Hexapod Robot. The RSA base plate calibration frame was then bolted to the lower pillar of the hexapod and the specimen mounted to the SCP of the hexapod with the anterior end of the foot facing outwards, directly in line with the positive Y axis of the hexapod's coordinate axis system.

Once both the base plate and specimen were mounted within the hexapod, the end effector of the hexapod's top plate was lowered under operation of the hexapods control system until the six legs of the robot were at the required high for the specimen to be tested. At this height, the 6DOF load cell of the robot was in contact with the SCP and could be bolted together prior to commencing testing.

A full protocol for the operation of the hexapod robot for the foot and ankle testing conducted in this project was developed and is included in APPENDIX F. Within this protocol, all steps

from initialization of the hexapod, input commands and sequential application of loading conditions are described.

5.3 X-Ray Setup

To capture the X-Rays in this project, the Biomechanics and Implant Laboratory's Philips DigitalDiagnost X-Ray system was used. This system was mounted to a rail system on the ceiling which allowed for effective X-Y-Z translation of the instrumental. Additionally, the head of the X-Ray could also be rotated with respect to the horizontal and vertical axis for effective positioning. In order to efficiently capture the left and right Stereoradiographs required for Radiostereometric 3D reconstruction process, the x-ray was positioned 60° left (for the left image) and right (for the right image) of the anterior plane, and angled downwards from the horizontal plane at an angle of 56°. These positions were marked with masking tape on the rails of the X-Ray system as well as locking system stoppers installed at these locations to ensure consistency in both the positioning of the x-ray system as well as the resulting left and right Stereoradiographs captured.

5.4 Simulation of Adult Acquired Flatfoot position in Cadaveric Model with the 6DOF Hexapod Robot

As described in Chapter 4, Section 4.3 – 4.5, the physical deformity was replicated by bringing the foot into 10 degrees of dorsiflexion, and applying compressive loads such that the force was directed approximately over the talonavicular joint of the ankle, resulting in the 3 physical characteristics of the deformity; (1) A collapse of the arch, (2), valgus of the hindfoot, (3) abduction of the forefoot (DiGiovanni & Greisberg 2007; Smyth et al. 2017; Kido et al. 2013b; Levinger et al. 2010). This was conducted under the observation of an orthopaedic foot and ankle specialist who concluded that the physical characteristics of the deformity had been produced.

Once the specimen was in dorsiflexion, simulating the stance phase of natural gait, incremental loads of 100N, 230N, 460N, 690N and 920N were applied in incremental

loadsteps such that the deformity could be progressively produced in discrete stages. Stereoradiographs were taken at each of these loadsteps.

When inducing the physical characteristics of AAFD through the application of sequentially increasing loading conditions, it was important to capture the stereoradiographs as closely as possible to the applied loadsteps to minimize the influence of the viscoelastic tissue responses, creep and stress relaxation on the ligament strain. In order to capture the radiographs using the hexapod robot, the load control mode needed to be exited (alleviating the load and holding the position), such that the doors of the system could be opened to insert the X-ray cassettes.

To capture the position of the foot as closely as possible to the applied loadsteps - once the loads had ramped up to the set loadstep, load control mode was exited and as quickly as possible, the cassettes were inserted and stereoradiographs captured. After the stereoradiographs were captured, load control was then reinstated such that the position of the foot was maintained at the set loadstep.

After exiting load control, and capturing the radiographs, some creep effects were observed where there was some recovery of strain, which occurred slowly over time. While the effects of creep are inevitable when simulating the biomechanics of cadaveric specimens, the effects were minimized by capturing radiographs as soon as the hexapod's load control mode was exited.

For the full testing protocol, refer to **APPENDIX F**.

5.5 Recording Data

The data from the pilot test was collected by the stereoradiographs captured at each loadstep as it was from the 3D reconstruction of these stereometric x-rays that displacement and strain data of the ligaments could be obtained. In addition to this, the hexapod robot also recorded force and position data at the end effector plate as the position of the foot was altered. To interpret this information, this data must first be transformed from the hexapod's raw 'leg length' data into readable force and position data at the specimens axis of rotation in post processing using a LabVIEW program developed to be used in conjunction with the hexapod's control system. This data includes force, positon and time information at each loadstep induced throughout the simulation. This hexapod data could be used to calculate the

theoretical stiffness of the foot/ankle specimens as a whole, as well as use the time information to explore strain rates. While this data was obtained from this project, the analysis of this information steps outside the scope and aims of this dissertation.

5.6 Results of pilot testing

From this pilot test, it was observed that the physical clinical characteristics of an anatomic adult acquired flatfoot deformity (collapse of the arch, hindfoot valgus, forefoot abduction) were successfully progressively produced in the cadaveric human specimen through the application of incremental loading conditions (Figure 47).

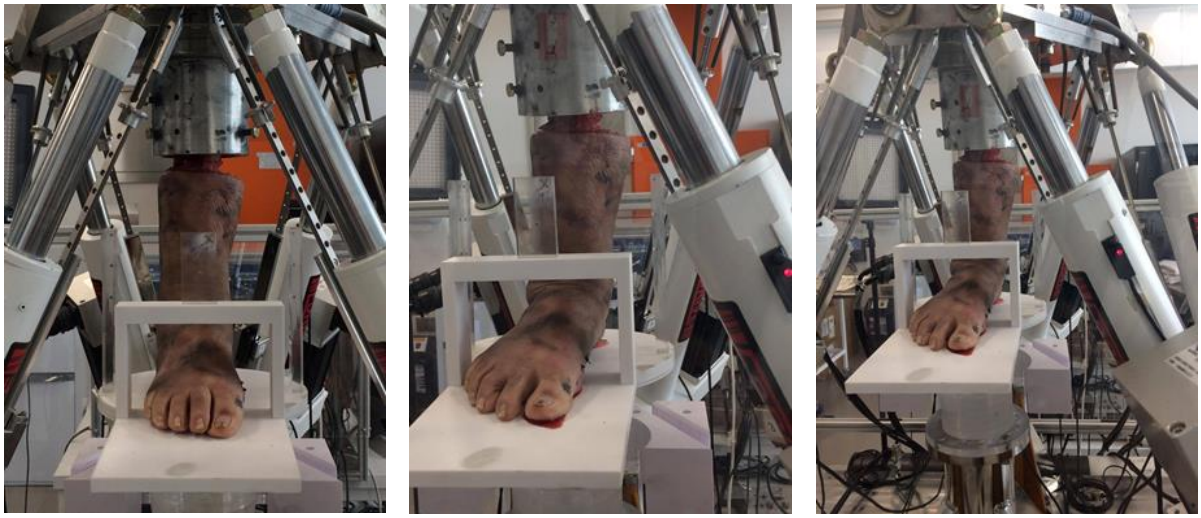

Figure 47: Hexapod Robot simulating the physical characteristics of AAFD in a cadaveric specimen

Stereoradiographs were captured (Figure 48) to determine whether an adequate number of beads were visible from the X-Rays, allowing the ligaments of the medial column to be tracked through the digitization of the stereoradiographs. As the sequence of involvement of the spring and deltoid ligaments were of high interest, it was important that the markers at the attachment sites of these ligaments be captured. Through this pilot test, the first set of stereoradiographs, representing the initial position of the foot were used as test stereoradiographs run through the MATLAB program. In doing so, a 3-dimensional representation of the markers with the foot was reconstructed from the stereoradiographs (Figure 49& 50) and the 3D coordinate positions for each marker calculated. From this initial

workable set of test x-rays, the RSA script was also further developed to calculate displacements of each marker between sequential incremental loadsteps and corresponding pairs of markers to trace their respective ligaments and calculate displacement and strain of each ligament.

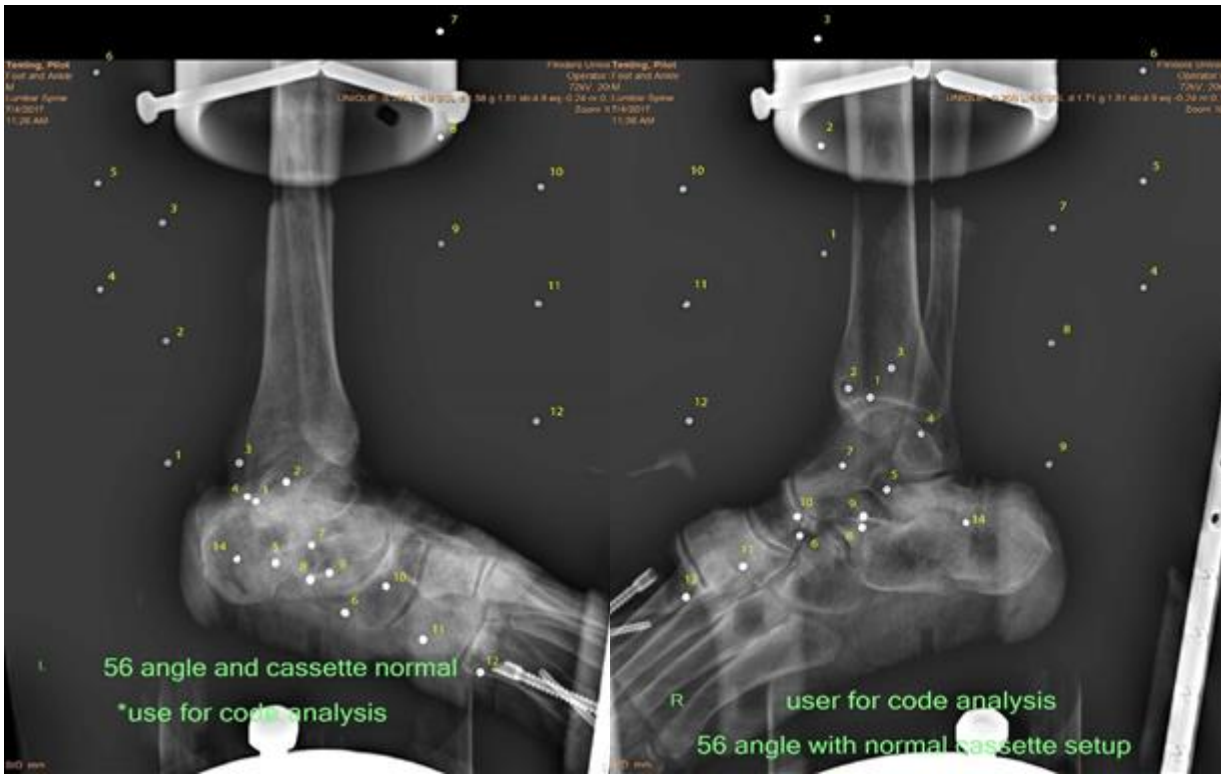

Figure 48: Stereoradiographs of Pilot Test Foot for Radiostereometric Analysis

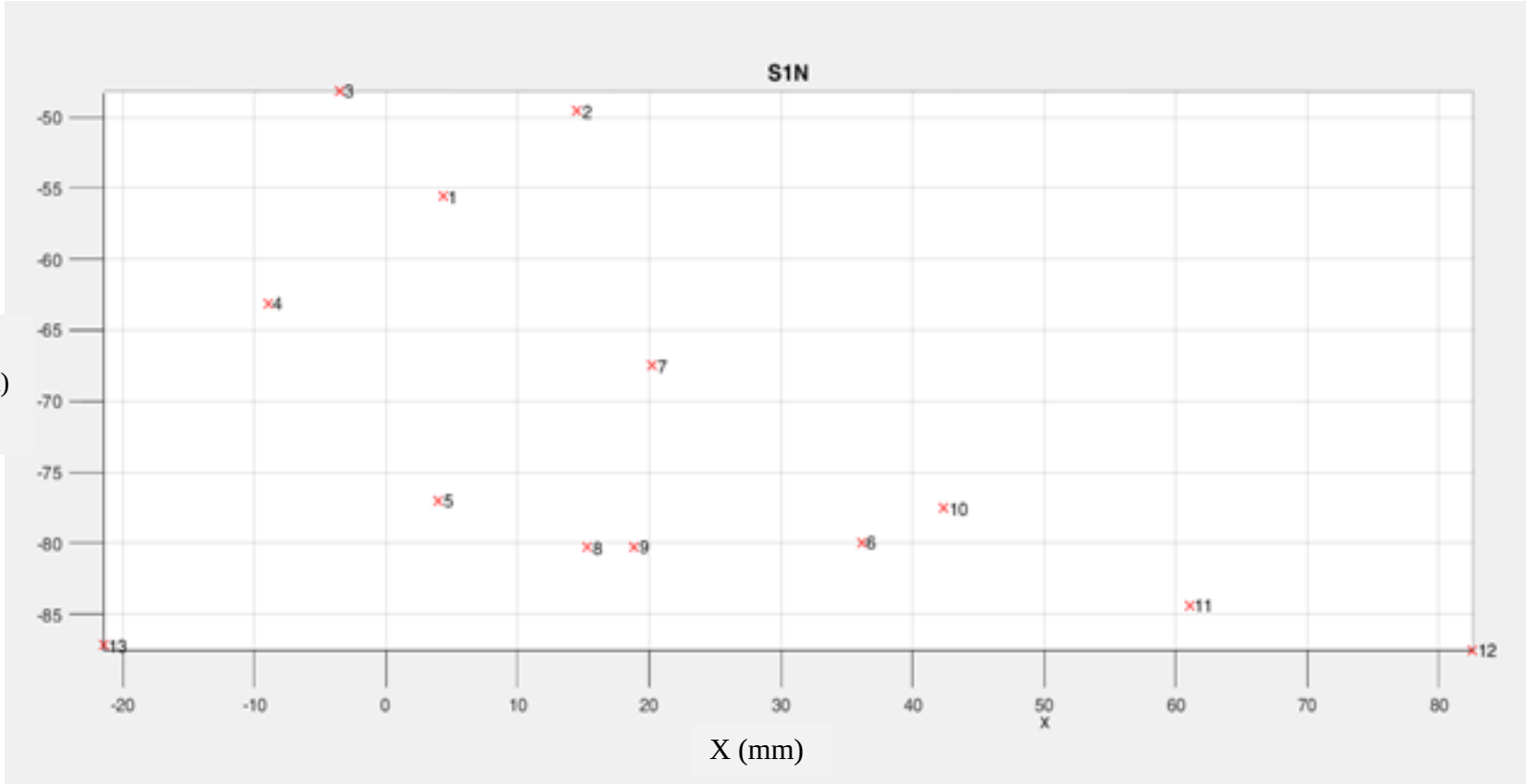

Figure 49: 3-Dimensional Coordinate Positions of Implanted markers through digitization of captured stereoradiographs (left lateral view)

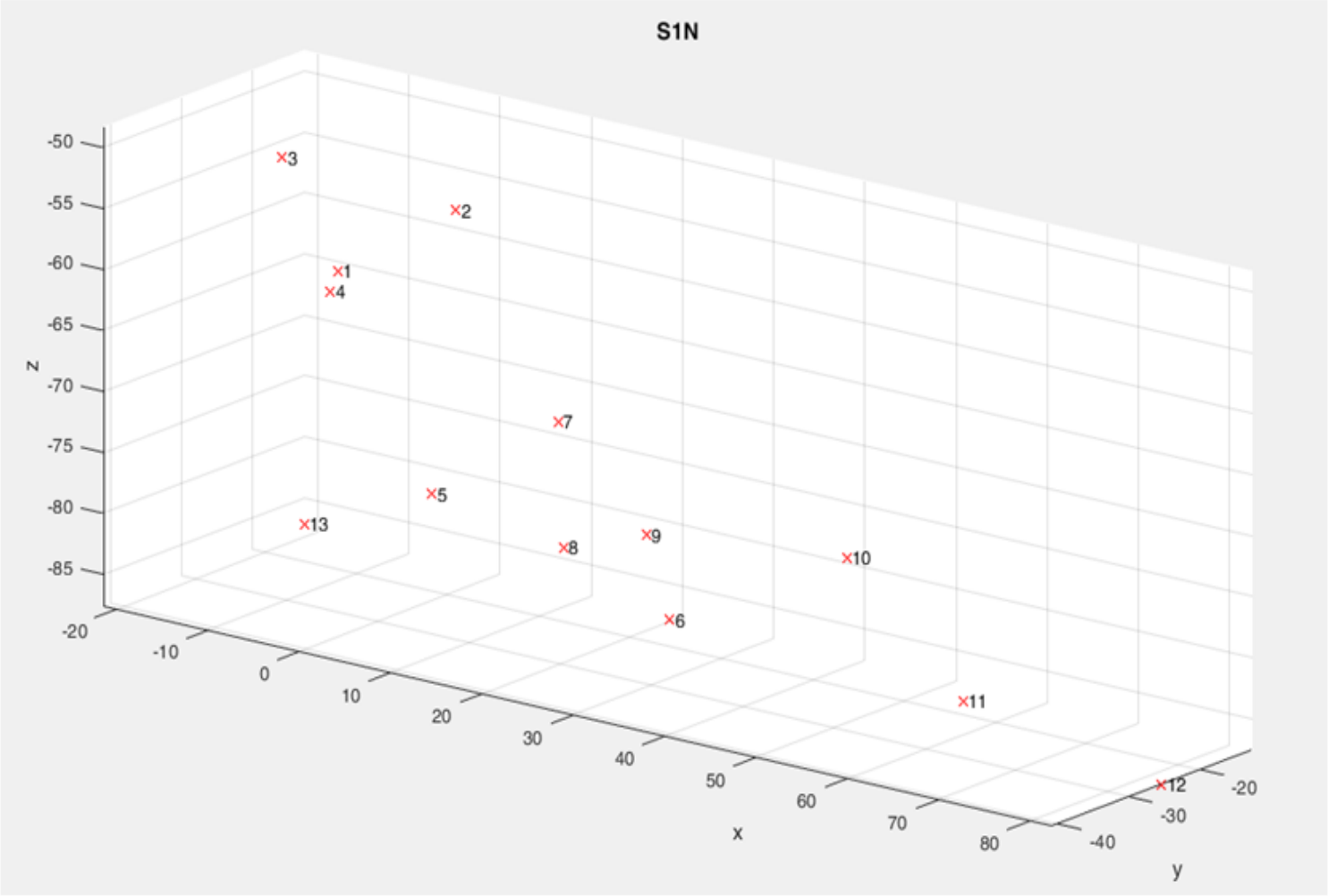

Figure 50: 3D representation of Implanted markers from captured Stereoradiographs

From the reconstructed stereoradiographs at the initial position, coordinate positions for each marker were calculated by the software in the digital reconstruction process.

Table 14: RSA Coordinate Positions of Beads within Pilot Test Foot Specimen

Marker	X (mm)	Y (mm)	Z (mm)
1	4.13	-40.91	-55.66
2	14.32	-37.36	-49.67
3	-3.73	-38.62	-48.24
4	-9.07	-25.00	-63.17
5	3.88	-27.34	-77.02
6	35.98	-35.03	-80.04
7	20.09	-30.37	-67.57
8	15.24	-23.35	-80.30
9	18.84	-16.36	-80.24
10	42.32	-18.28	-77.56
11	60.93	-25.80	-84.42
12	82.47	-25.56	-87.57
13	-21.50	-12.75	-87.18

5.7 Improvements for test specimens

From this pilot test, it was realized that it would be of interest and beneficial to the study to calculate the strain within the achilles tendon of the specimen as the physical deformity was progressively produced. As such, it was decided that during the preparation & potting of the test specimens, 2 additional tantalum beads would be placed on the achilles tendon, such that longitudinal strain of the tendon could be calculated at each progressive loadstep, in addition to the ligaments of the medial column being tracked.

[Figure has been removed due to copyright restrictions]

Figure 51: Final Bead Placement Positions for Test Specimens

5.8 Conclusion

Overall, the pilot test confirmed that the physical clinical characteristics of an anatomic AAFD (i.e. collapse of the longitudinal arch, hindfoot valgus, forefoot abduction) could be progressively produced in a cadaveric human foot specimen using the hexapod robot. Furthermore, the RSA technique was successfully conducted and coordinate positions for each marker implanted within the foot specimen were captured. This allowed for the RSA script to be developed further to automatically pair sets of markers corresponding to their respective ligament from the stereoradiographs of the human specimen at hand thus and calculate displacements and strains occurring at each incremental loadstep.

Chapter 6: Specimen Testing

For the test specimens, 10 fresh-frozen cadaveric feet (right side) were obtained from the United Tissue Network, Oklahoma (from donors aged 58 – 84 years old). Specimen demographic data is included in the Appendix (**Appendix H**). As these specimens were prepared through the implantation of the tantalum markers at the attachment sites of the ligaments of the medial column, one specimen was noted to have severe peripheral edema. On the grounds of a biological health, safety and hygiene issue, this specimen was deemed unsuitable for biomechanical testing within the hexapod robot on. Hence, 9 fresh-frozen cadaveric feet (aged 58 – 84 years old) were used for experimental testing.

6.1 Human Foot Preparation

The specimens to be tested were removed from the freezer room and thawed for 24 hours to the day of testing. In the preparation of these specimens for potting, as the excess soft tissue was removed from the tibia and fibula, the achilles tendon was also exposed by cutting the sutures inserted by the surgeon during the implantation of the tantalum markers which held the epithelial soft tissue above the tendon closed. Two additional beads were then placed on the achilles tendon, as described in chapter 5, section 5.5 and secured in placed with a small drop of liquid adhesive.

Following the insertion of the markers on the achilles tendon, As described in chapter 5, section 5.1, to mount the cadaveric specimens to the Hexapod robot, the specimens had to be ‘potted’ into metal top cup and secured in place with a PMMA cement mixture. (Refer to Chapter 5, section 5.1 & Appendix X for the full specimen preparation protocol).

6.2 Specimen Offset

For each of the specimens tested, once the specimen was prepared and potted, lateral and PA x-rays were taken to determine X,Y and Z offsets for the axis of rotation (AoR) as described in chapter 5, section 5.2. The offsets for the AoR for each specimen are shown below (refer to table 15)

Table 15: Axis of Rotation Offsets for the Test Specimens

No.	Specimen ID	X offset	Y offset	Z offset
1	FS00	0	-12	244
2	FS01	0	-4	236
3	FS02	-8	-9	187
4	FS03	0	0	191
5	FS04	-10	14	181
6	FS05	-7	0	170
7	FS06	-5	-16	190
8	FS07	0	-9	195
9	FS08	-7	10	200

6.3 X-Ray Setup

As with the pilot tests, the positioning of the x-rays used for the test specimens were taken at 60° left (for the left image) and right (for the right image) of the anterior plane, and angled downwards from the horizontal plane at an angle of 56°. (Refer to chapter 5, section 5.2).

6.4 Testing of Simulated Flatfoot Deformity

As described in Chapter 4, Section 4.3 – 4.5, the test specimens were subjected to a series of incremental loads (100N, 230N, 460N, 690N and 920N) to progressively produce the physical characteristics of AAFD.

For the full simulation testing protocol, refer to APPENDIX F.

At each of these loadsteps, stereoradiographs of the specimen were captured. After capturing each x-ray, the image was checked to ensure all the calibration markers were visible. In some instances, as the legs of the hexapod moved to apply the incremental loading conditions, the legs of the encoder blocked visibility of some of the calibration markers. In this case, it was always one marker for a given rod that was occluded, thus leaving 2 markers of the same rod visible on the x-ray. As outlined in chapter 4, sections 4.9, all of the x-rays were visually enhanced in post processing to ensure effective identification and digitization of the markers from the x-rays through the MATLAB software. In the instances where for a given rod, only 2

calibration markers were visible (due to one being occluded by the physical dimensions of the hexapod robot), the ruler tool was used to measure the distance between the 2 visible markers, and accurately interpolate the remaining reference marker.

6.5 Results from Specimen Testing

From conducting the testing on the 9 test specimens, it was observed that the physical clinical characteristics of an anatomic adult acquired flatfoot deformity (collapse of the arch, hindfoot valgus, forefoot abduction) were successfully produced in the cadaveric feet, with stereoradiographs successfully captured through the progression of the deformity at the incremental loads applied. From the stereoradiographs captured, it was noted that as the arch was increasingly reduced and the foot splayed out, for some specimens, it was not possible to capture the markers implanted closer towards the proximal end of the foot (markers 10, 11 and 12) in the field of view of the x-rays. This was addressed through a statistical approach in the results section of this dissertation (refer to chapter 7).

The stereoradiographs captured from the experiment were then visually enhanced in post processing (Adobe Photoshop CS6) and any missing calibration markers (obstructed from x-ray view by the hexapod's encoders) interpolated via the software's digital measurement tool. For each specimen, the stereoradiographs at each loadstep were then run through the RSA MATLAB script to produce a 3-dimensional representation of the markers with the foot with calculated coordinate positions for each marker. From comparing the 3D coordinate positions for each marker at sequential loads and pairing sets of markers to form the corresponding ligaments, the displacement of each marker and strain response of each ligament could be calculated.

Chapter 7: Results

This chapter provides an understanding of the analysis and results of the data collected for the research study. The value and quality of the data collected is highly dependent on the design of the RSA calibration frame, hexapod control protocol, bead implantation in carefully identified locations, optimal use of x-ray machine as well as the RSA transformation algorithm developed in MATLAB to measure the positons and displacements of the implanted beads with each incremental load applied.

As highlighted in the aims and rationale of this dissertation (Chapter 3), the broad research aim was to investigate the sequential biomechanics involvement of the medial column ligaments in the progression of AAFD, however in order to elicit this data, the experimental design had to carefully thought through and executed to ensure the data collected was as authentic and useful as possible.

From this experimental design, 3 dimensional positions and displacements of each marker (tantalum beads implanted at the bony landmark attachment sits of the 11 ligaments) were captured. Through using automated marker pairing to identify the ligaments of interest at their approximate fiber orientation, longitudinal strains for each ligament were calculated at each incremental load, inducing progression of the physical characteristics of the deformity. As a result, the strain response data for each of the 11 ligaments at incremental loads (through which the physical characteristics of the deformity was progressively induced) was collected. From the obtained data, a statistical analysis of the data could be conducted. The broad aim of the statistical analysis was to investigate the associate between the strain responses of the ligaments (MCL) as the physical deformity progressed.

From the data obtained, this aim could be investigated through addressing 4 specific research questions.

1. How do the administered incremental loadstep impact each of the ligaments?
2. Is there a difference between the dependent variable (strain response of ligaments) and the loadsteps (100N, 230N, 460N, 690N, 920N)?
3. What are the interaction-effects between the progressive loads and the ligaments?
4. How the various ligaments are clustered and do they exhibit a similar response?

7.1 Data Introduction

In this experiment, there were 11 static stabilizing ligaments of the medial column for which the strain response is measured at 5 incremental loads, as the position of the foot is progressively altered to replicate the anatomic position of the deformity.
As the same ligaments are subjected to 5 loading conditions, the study is of a repeated measure design.

It should be noted that physiologically, the ligaments do not behave independently of one another and there are interactions between them as the bones of the foot are held together. "The joints are interdependent. A change in the function or structure of one joint in the system will usually cause a change in the function of a joint either immediately adjacent to the affected joint or at a distal joint" (Levangie & Norkin 2005). In regards to this project where characteristics of an anatomic deformity are induced, there are compensatory reactions between the ligaments involved (Houglum & Bertoli 2012;Bonnefoy-Mazure & Armand 2015).

For the dataset collected from this project, it was essential for x-rays to be taken at a horizontal angle of 56 degrees and a vertical angle of 60 degrees to the subject in order to most effectively digitally reconstruct the left and right stereoradiographs to form a 3D transformation. Due to this and the physical change progressively induced in the feet specimens; for some specimens at the higher loadsteps (where the arch was flattened), the x-rays were not able to capture some of the markers located most proximally of the specimen (markers 10, 11 and 12) in the field of view. This occurred as a result of the foot splaying as the hindfoot valgus, forefoot abduction and collapse of the medial arch was produced. This resulted in some missing values for the ligaments more distal to the ankle joint.

7.1.1 Handling Missing Data & Imputation Techniques

In any experiment, missing data is inevitable(Blann 2015; Dinov 2016; Hoffman 2015; Little & Rubin 2014). Dinov (2016, p.6) indicates "missing data arise in most complex data-driven inquiries". Moreover, "substantial instances of missing data are a serious problem that undermines the scientific credibility of casual conclusions from clinical trials. The assumption that analysis methods can compensate for such missing data are not justified, so aspects of trial

design that limit the likelihood of missing data should be an important objective"(Little et al. 2012, p.1335). They highlight further that "too many current analyses of clinical trials apply naïve methods for missing-data adjustment that make unjustified assumptions, such as the last-observation carried-forward approach. In reports and interpretations of trial results, the handling of missing data requires a scientifically defensible analysis coupled with a sensitivity analysis to assess robustness" (Little et al. 2012, p.1359).

Considering this, missing data can be addressed through statistical techniques(Little et al. 2012; Marron & Wahed 2016). Here are various statistical methods implemented in software available to impute (fill) in these missing values. Maron & Wahed (2016, p.8), highlight "the need for valid statistical analyses in medical sciences and many other fields and an education in statistical reasoning can lead to practical statistical literacy and a greater appreciation of the topic"

The authors reiterate the importance of understanding missing data and imputation, which takes a correlation between known cell data from which a regression formulate is used to fill in the missing values. They then re-introduce the use of "two methods of multiple imputation: regression imputation and Monte Carlo Markov Chain (MCMC) multiple imputation" (Marron & Wahed 2016, p.12). In this study, the later was used though IBM SPSS (Version 20).

The "MCMC is described as using Markov chains based on observed information to obtain random draws from a joint distribution of variables that contain missing values. The random draws are then used to impute values in place of missing observations. Like regression imputation, MCMC imputes values for missing observations in the outcome, but it can also impute values for missing observations in predictors" (Marron & Wahed 2016, p.12).

7.2 Analytic Framework

Repeated measures analysis (also called within-subjects), deals with response outcomes measured on the same experimental unit at different times, or under different conditions/treatments (Singh et al. 2013). In this study, repeated measures were taken for the Achilles tendon (L0), as well as the 11 static stabilizing ligaments of the medial column (L1 – L11) at incremental loads.

The analysis of variance (ANOVA) is used to analyze the differences among group means and their associated variances both among and between groups. A t-test compares the means of two groups, and the ANOVA is useful for comparing three or more means (groups/variables) for statistical significance(Johnson 2018; Peck et al. 2016). A two-way ANOVA indicates possible interactions between subjects and the conditions applied.

This study utilized the Repeated Measures two-way ANOVA to answer the specific research questions surrounding the involvement of the 11 ligaments subjected to the 5 load conditions. The primary purpose of conducting the ANOVA is to understand if there is an interaction between factors on the dependent variable.

To examine this research question (RQ3), a repeated-measure analysis of variance (ANOVA) was conducted to assess if mean differences exists on the dependent variable by the treatment (incremental loading conditions). The repeated measures ANOVA is used to test the effects of a continuous dependent variable (strain response of the ligaments) measured several times with different treatments (loading conditions). The F-test of significance is used to assess the effects of the different treatments. To use this, it is assumed that the dependent variables (ligament strain data) are normally distributed. Sphericity, i.e. the validity of the ANOVA will be assessed through a Mauchly's test of Sphericity.

Before an ANOVA can be used, it must be acknowledged that there are a number of assumptions which must be met. These assumptions include:

1. The dependent variable (ligament strain) should be measured at the continuous level.
2. Within-subjects factors (i.e. loadsteps applied) should consist of at least two categorical "related groups" or "matched pairs" (ligaments subjected to five loadsteps).
3. Distribution of the dependent variable should be approximately normally distributed
4. Sphericity (the variances of the differences between all the combinations of related groups) must be equal.

This study acknowledges the importance of statistical power analysis used in repeated measures designs (Guo et al. 2013; Morgan & Case 2013). Although Borzage et al (2017) used 12 samples for their repeated measures study(Borzage et al. 2017), a delimitation of this study is the sample size (n=9) used, which has important implications for future research work.

In addition to the Repeated-Measure Two-way ANOVA used, a Cluster Analysis was also conducted with the dataset. An important extension to Repeated Measures is Cluster Analysis (Ilango et al. 2011; Johnson 2018; Xu & Wunsch 2010; Zhao et al. 2014). Ilango et al (2011) highlights that cluster analysis, a method of multivariate data mining, is concerned with the similarity of the subjects (strain response of the ligaments in this study). The objective of a Cluster Analysis is to find similar groups of subjects where "similarity" between each pair of subjects exists. "Applications of clustering algorithms in biomedical research are ubiquitous, with typical examples including gene expression data analysis, genomic sequence analysis, biomedical document mining, and MRI image analysis"(Xu & Wunsch 2010, p.120). Zhao et al (2014, p.2) reiterates the importance of Cluster Analysis with biological and medical datasets through highlighting that "cluster analysis is a commonly used data mining technique to explore the relationships among attributes, samples and the relationships between attributes and samples. Clustering algorithms assign samples or attributes to clusters based on their similarity. Cluster analysis can be used as a preliminary method for classification or for finding new classes or associations. A hierarchical clustering tree (HCT) sequentially merges the most similar cluster sub-nodes resulting in a tree-like dendogram".

A common way to visualize the cluster analysis's progress is by drawing a dendogram that displays the distance level at which there was a combination of objects and clusters(Mooi & Sarstedt 2011, p.253). Cluster analysis was undertaken with the dataset collected in this project and a dendogram plotted to answer RQ4.

To respond to the various specific research questions (RQ1 – RQ4), a number of online resources have been studied. Several of these resources provide examples into undertaking Repeated Measures 2-way ANOVA and include annotations of outputs and their interpretations. The following online resources provided useful support.

- Two-way repeated measures ANOVA using SPSS Statistics (https://statistics.laerd.com/spss-tutorials/two-way-repeated-measures-anova-using-spss-statistics.php)
- University of Sheffield Stats Tutor (https://www.sheffield.ac.uk/polopoly_fs/1.531222!/file/MASH_repeated_measures_ANOVA_SPSS.pdf)

- University of Sussex ‘Using SPSS: Two-way Repeated-Measures ANOVA’ site (http://www.lifesci.sussex.ac.uk/home/Zoltan_Dienes/SPSS%202-way%20rm.html)
- University of Ottawa Biomechanics Laboratory Site – Repeated Measures ANOVA (http://health.uottawa.ca/biomech/courses/apa6101/Repeated%20Measures%20ANOVA.pdf)
- University of Colorado – Denver College of Nursing Site (http://www.ucdenver.edu/academics/colleges/nursing/Documents/PDF/RepeatedMeasuresANOVA.pdf)

7.3 Data Imputation

As previously highlighted in the beginning of this chapter, unobtainable data for markers 10, 11 and 12 in some of the specimens at the higher loads resulted in missing strain data for some of the ligaments. The ligaments containing missing data were primarily the plantar cuneonavicular ligament (L9), plantar cuneometatarsal ligament (L10), as well as few missing values at higher loads for the Tibiospring portion of the deltoid ligament (L5) and the superomedial calcaneonavicular spring ligament (L6).

As highlighted in Section 7.1.1, a Monte Carlo Markov Chain (MCMC) multiple imputation method implemented in IBM SPSS was used to statistically impute some of the missing data present.

From the statistical data imputation of strain response data, a full sample number of 9 was achieved for all of the ligaments, except for ligaments 9 (plantar cuneonavicular ligament) and ligament 10 (plantar cuneometatarsal ligament) for which the algorithm was not able to statistically impute due to the small data size available for these ligaments. For these two ligaments, a sample number of 6 and 3 respectively was able to be included in the dataset (Table 16).

Table 16: Sample number for each ligament (After Statistical Imputation)

Ligament	N
L0 - Achilles tendon	9
L1 - Deltoid: anterior tibiotalar Pt.	9
L2 - Deltoid: posterior tibiotalar Pt.	9
L3 - Deltoid: tibiocalcaneal Pt.	9
L4 - Deltoid: tibionavicular Pt.	9
L5 - Deltoid: tibiospring Pt.	9
L6 - Spring Ligament: superomedial calcaneonavicular	9
L7 - Spring Ligament: inferior calcaneonavicular	9
L8 - Medial talocalcaneal Ligament	9
L9 - Plantar cuneonavicular ligament	6
L10 - Plantar cuneometatarsal ligament	3
L11 - Interosseous (indirect)	9

7.4 Descriptive Statistics

For each specimen, the stereoradiographs at each loadstep were transformed to output position data. From the comparison of coordinate position data at sequential loadsteps, the displacements that occurred at each marker was calculated. From this, a 3D vector map illustration the displacements of each marker at sequential loads could be plotted. Upon averaging the displacements of each marker across the specimens, a similar 3D vector map could be generated. These 3D models display the coordinate position of the marked landmarks at an initial position, as well as displacement vectors (scaled up by a factor of 4) for each marker at the sequential loads applied. This illustrates the physical movement occurring within the specimen as the physical characteristics of the deformity were induced.

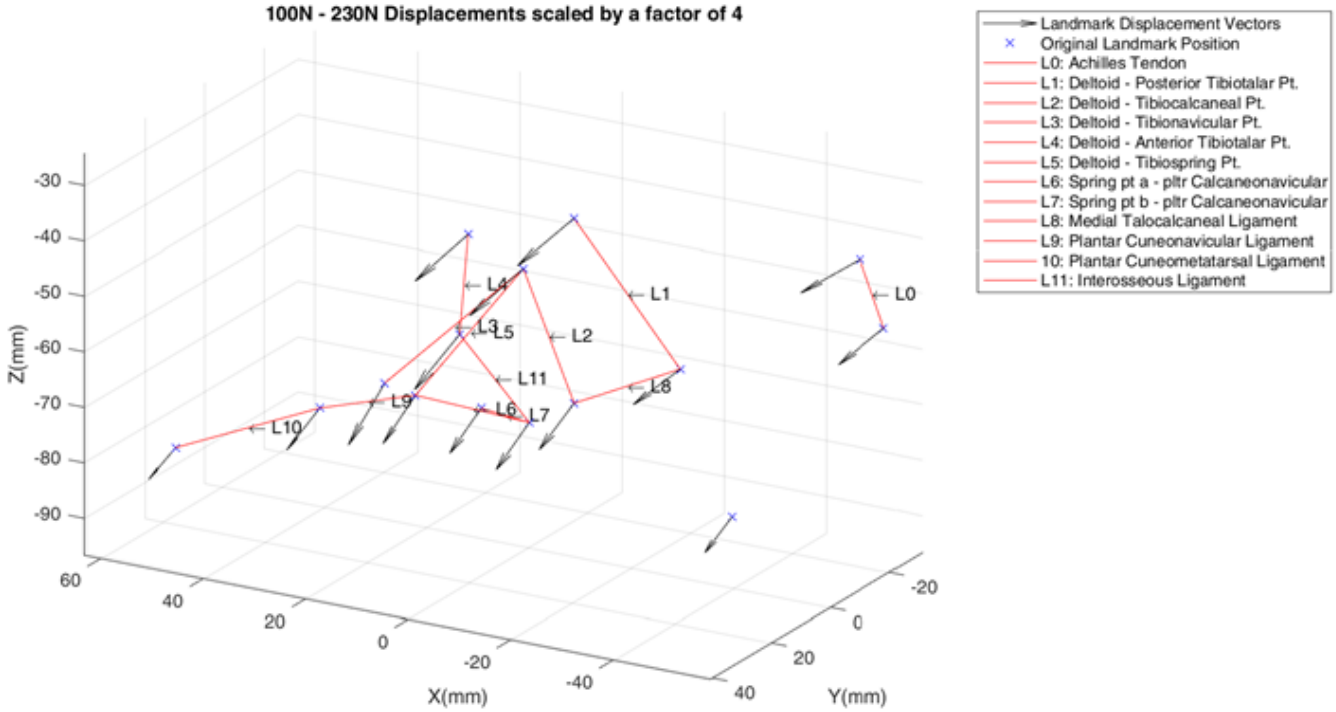

Figure 52: 3D Displacement Vector Map – Progression I (100N – 230N)

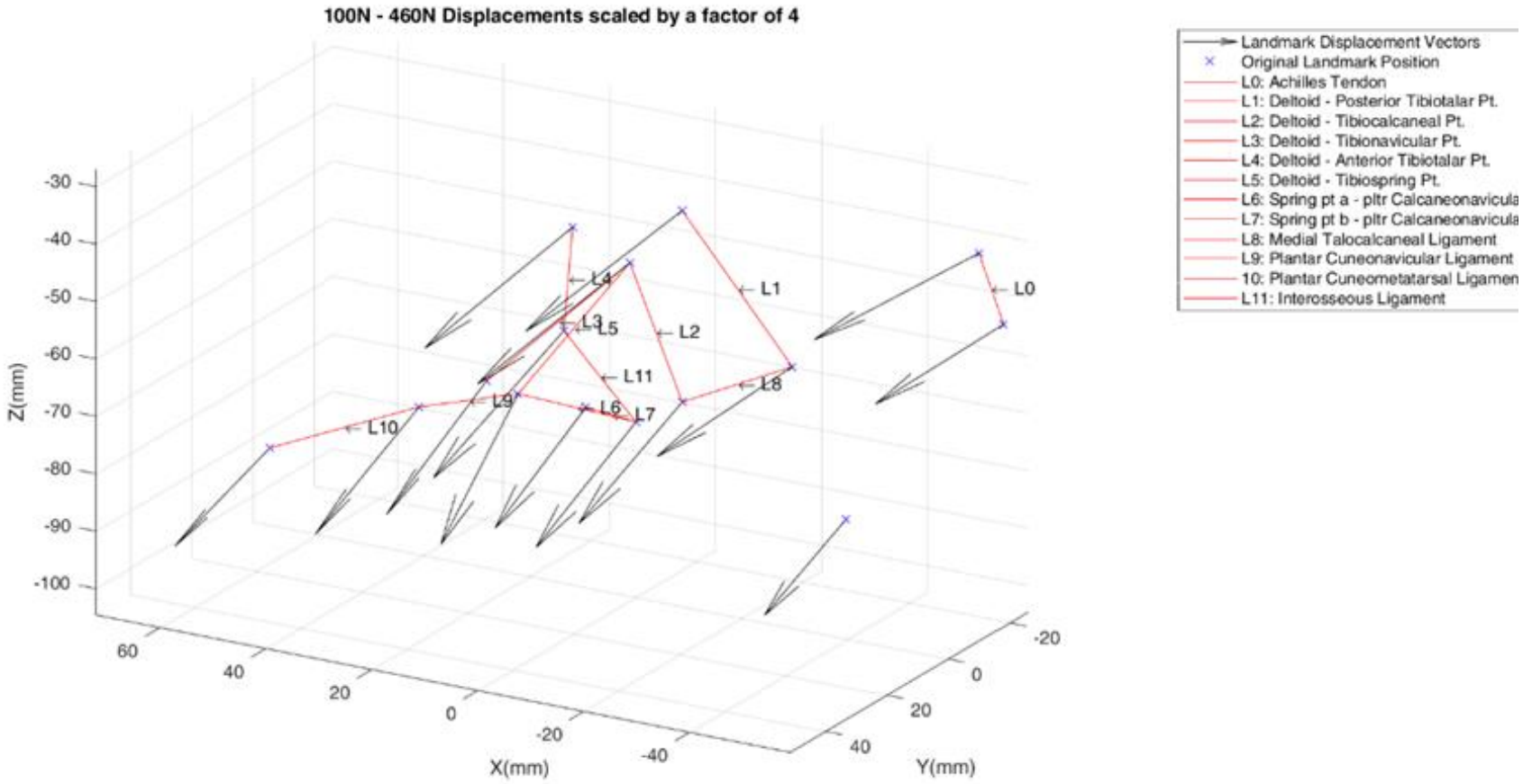

Figure 53: 3D Displacement Vector Map – Progression II (100N – 460N)

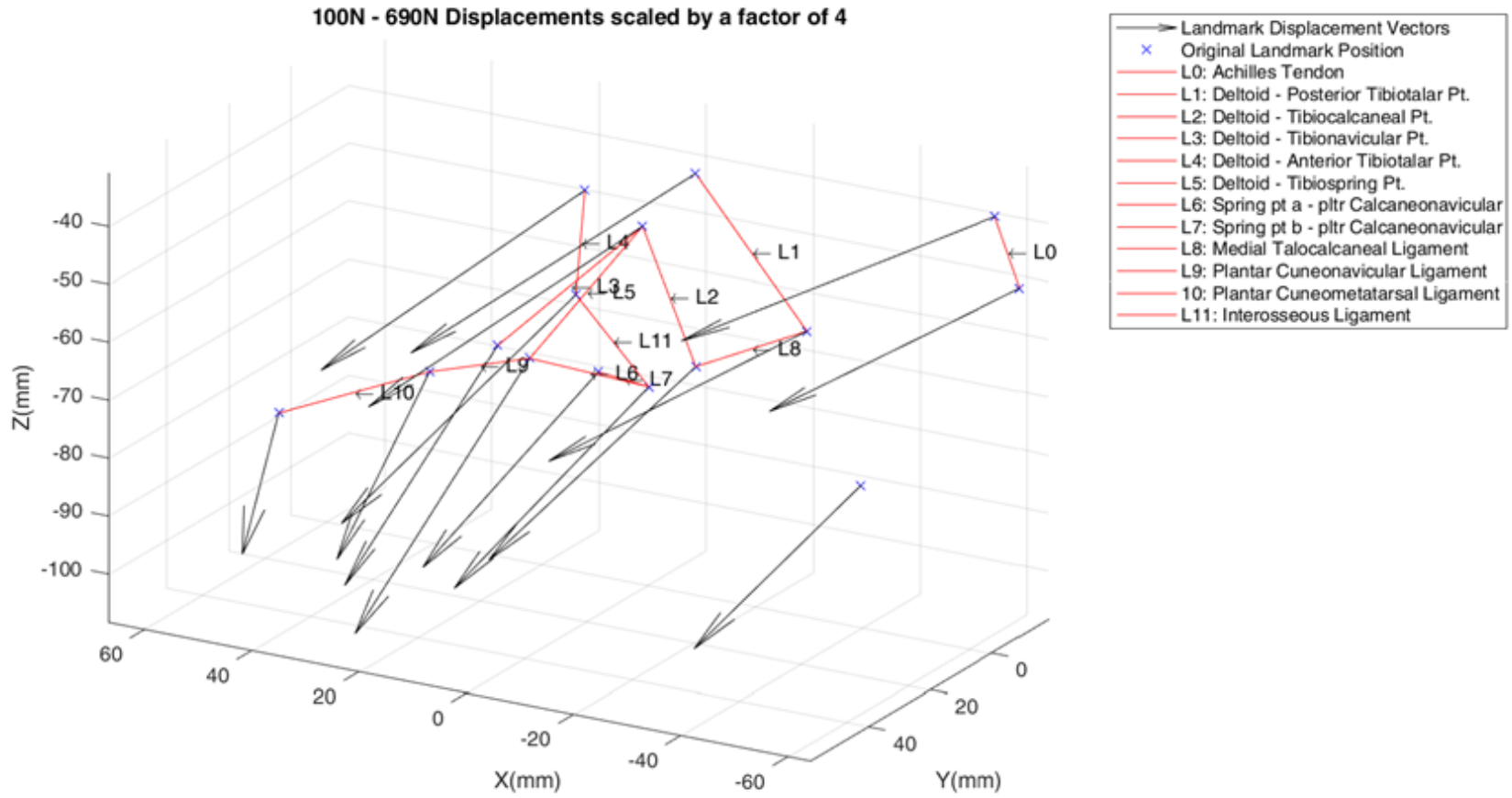

Figure 54: 3D Displacement Vector Map – Progression III (100N – 690N)

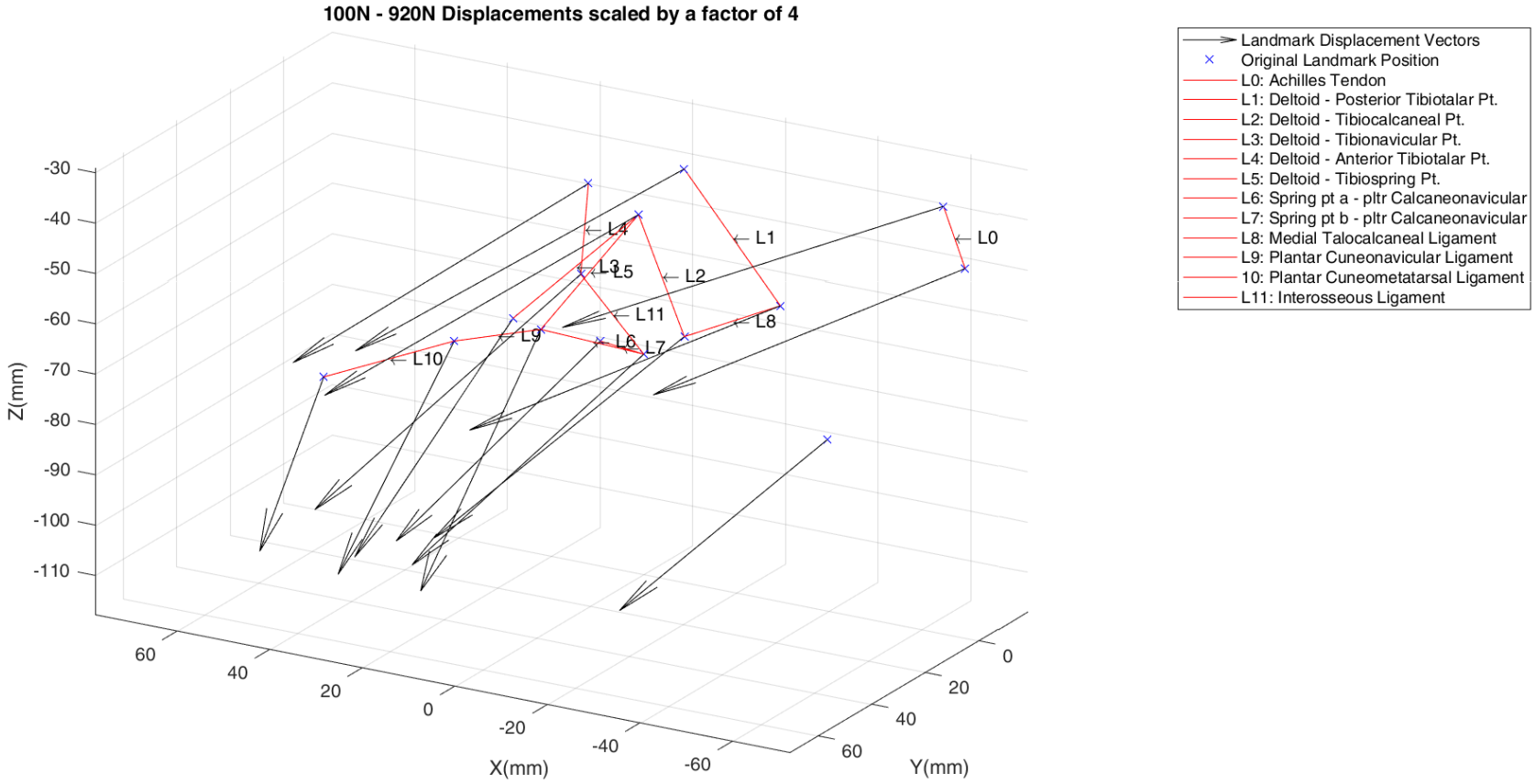

Figure 55: 3D Displacement Vector Map – Progression III (100N – 920N)

From the vector map, the key anatomic characteristics of AAFD can be identified through comparison of the displacement vectors at the key anatomical landmarks within the foot.

1. Flattening of the longitudinal arch
2. Valgus of the hindfoot
3. Forefoot abduction

Each sequential 3D vector map illustrates the accumulative displacements occurring of the tantalum markers implanted within the specimen. As the loads are progressively increased, the physical characteristics of the deformity were more pronounced. This is indicated by the increasing magnitudes of the displacement vectors in the series of 3D plots.

It can be observed that the vectors of the forefoot are moving in the same direction as the hindfoot, however, the magnitude of the vectors of the forefoot are smaller than those of the midfoot and hindfoot. This indicates an abduction of the forefoot relative to the hindfoot, as was observed across the specimens during testing.

The downward components of the vectors (particularly the markers on the structures laying closest to the base plate) illustrates the progressive flattening of the arch.

The magnitude of the hindfoot vectors pointing towards the left are greater than those of the forefoot, illustrating the hindfoot valgus which was physically observed during testing.

7.4.1 RQ1: How the various loads administered impact on the ligaments (L1 – L11; Achilles Tendon L0)?

From the displacements and pairing of markers (located at the bony landmark ligament attachment sites) to form the corresponding ligaments, the average strain response across each ligament could be calculated at the incremental loads. This was calculated via the formula:

$$\varepsilon = \frac{L - L_0}{L_0}$$

Table 17 highlights the average strain response (mm/mm) across the tested specimens for each ligament, at the incremental loadsteps. It is evident from the table that some of the ligaments were recruited into tension and elongated, while others contracted. In the table, the negative values are depicted in red and represent a contraction of the ligament, while the positive values are depicted in blue and represent an elongation of the ligament. At each incremental load, the highest strain in elongation and contraction is highlighted.

Table 17: Averaged Accumulative Strain Response of the Medial Column Ligaments and Achilles Tendon at Incremental Loads

	F100_230N				F100_460N				F100_690N				F100_920N		
Ligament	**Strain Ɛ(mm/mm)**				**Strain Ɛ(mm/mm)**				**Strain Ɛ(mm/mm)**				**Strain Ɛ(mm/mm)**		
	Mean	**Std. Deviation**	**N**		**Mean**	**Std. Deviation**	**N**		**Mean**	**Std. Deviation**	**N**		**Mean**	**Std. Deviation**	**N**
L0 - Achilles Tendon	0.009673	0.015248156	9		0.0120083	0.017039	9		0.02856989	0.038008	9		0.050449	0.038931	9
L1 - Deltoid: Anterior Tibiotalar Pt.	0.00136811	0.020216865	9		-0.009011	0.016627	9		-0.0231659	0.027736	9		-0.03786	0.040147	9
L2 - Deltoid: Posterior Tibiotalar Pt.	0.00919311	0.012266579	9		0.0256622	0.027696	9		0.04192411	0.031717	9		0.049291	0.038022	9
L3 - Deltoid: Tibiocalcaneal Pt.	0.01532467	0.016765551	9		0.0526974	0.072493	9		0.06996989	0.107938	9		0.06255	0.124383	9
L4 - Deltoid: Tibionavicular Pt.	-9.211E-05	0.024346626	9		0.0175118	0.03603	9		0.03924411	0.044346	9		0.051244	0.059379	9
L5 - Deltoid: Tibiospring Pt.	0.00514211	0.011743552	9		0.0200931	0.051727	9		0.02597348	0.070448	9		0.047197	0.080255	9
L6 - Spring Ligament: Superomedial Calcaneonavicular	0.01462844	0.02125332	9		0.0168587	0.064617	9		0.00249564	0.066214	9		-0.01868	0.073489	9
L7 - Spring Ligament: Inferior Calcaneonavicular	-0.0009859	0.010036577	9		-0.009357	0.026626	9		-0.0261876	0.031207	9		-0.0315	0.045401	9
L8 - Medial Talocalcaneal Ligament	-0.0053107	0.029120697	9		-0.000663	0.044665	9		0.01630822	0.052136	9		0.018048	0.059527	9
L9 - Plantar cuneonavicular ligament	-0.0191655	0.044635665	6		-0.023866	0.099126	6		0.01702783	0.147878	6		0.001111	0.165392	6
L10 - Plantar cuneometatarsal ligament	-0.0117717	0.0027074	3		-0.045197	0.01318	3		-0.0647729	0.066515	3		-0.07065	0.097363	3
L11 - Interosseous Indirect	0.00186189	0.007835186	9		0.0048	0.013635	9		0.01393022	0.039479	9		0.011105	0.057648	9

Table 17 highlights that in general, amongst a majority of the ligaments there tend to be increase in the magnitude of the strain as the loads are progressively increased. As the physical characteristics of AAFD were progressively produced, at each of the applied loading conditions, the Tibiocalcaneal portion of the Deltoid ligament recorded the highest strain response (elongation)

7.4.2 RQ2: Is there a difference on dependent variable (ligament extension) by load (load 1, load 2, load 3 and load 4)?

To respond to this research question, the information obtained from Table 17 was used to plot the strain responses of the ligaments at the incremental loads. It should be indicated that linear plots were subjected to the spline curve function available in the SPSS graphs to highlight physiological non-linearity of the extensions and contractions of the ligaments.

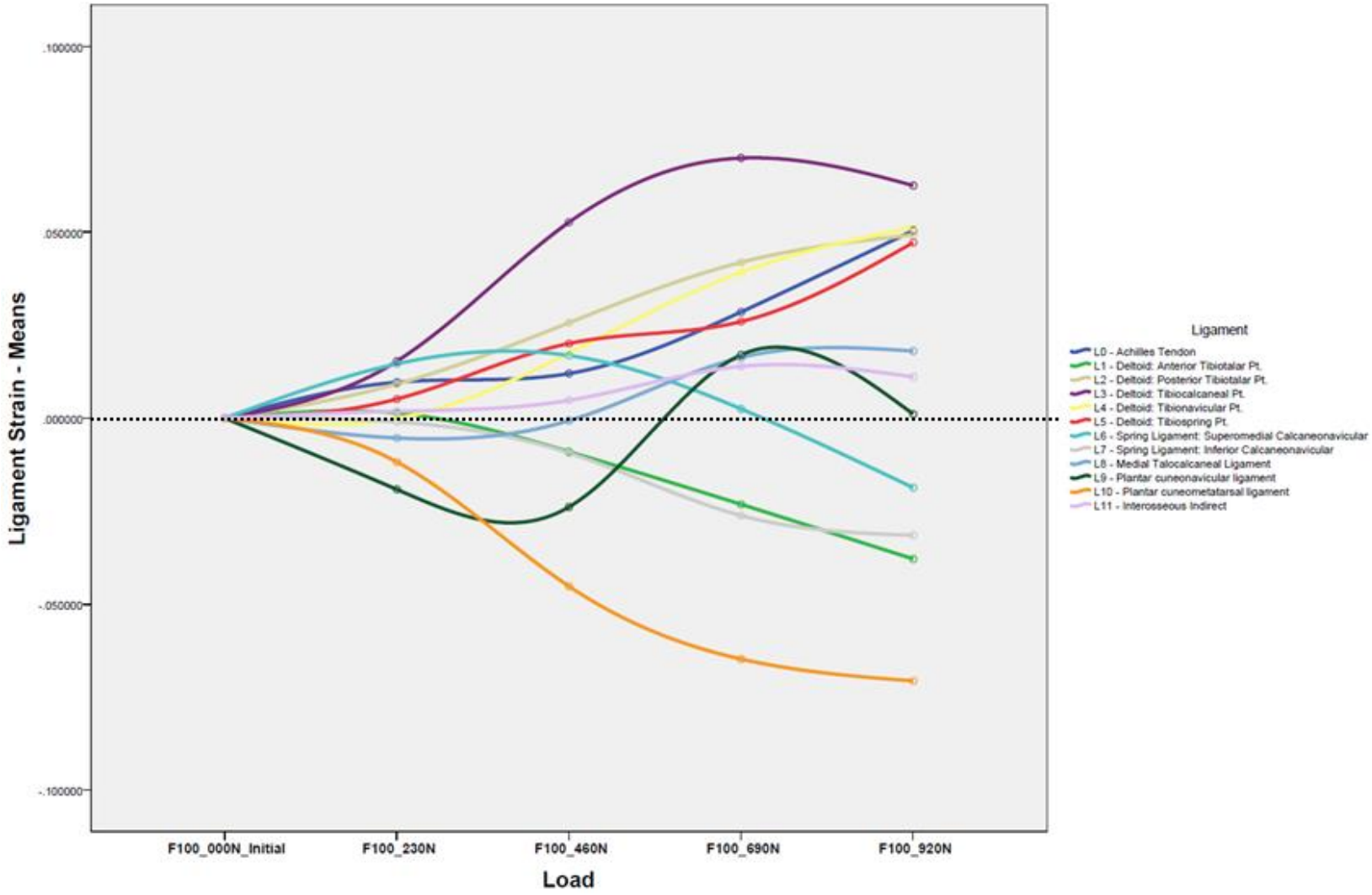

Figure 56: Average Strain Response of the Medial Column Ligaments and Achilles Tendon at Incremental Loads

The graph (Figure 56) illustrates the average strain response of each ligament at the incremental loads applied to progressively simulate the deformity. From the table and resulting graph, the sequential involvement of the ligaments during the progression of the physical deformity can be visualized with the central midline separating contractions and elongations of the ligaments. The standard deviation for each ligament is reported in Table 17 (p.120). Error bars could be included in Figure 56 to represent better the measurement errors associated at each load step; however, the addition of error bars will complicate Figure 56 due to overlapping bars and errors. Moreover, a larger sample (n=30) would provide better representation of ligament recruitment. It can be seen that from the data obtained, the tibiocalcaneal portion of the deltoid experiences the highest strain response in elongation through all of the incremental loads applied. It can also be seen that the plantar cuneometatarsal ligament continues to contract in an effort to maintain the arch by holdings the bones of the forefoot together as the height of the arch is reduced.

Furthermore, it is interesting to note the similarity and association between the accumulative strain response of the tibiocalcaneal portion of the deltoid ligament (ligament 3) and the plantar cuneometatarsal ligament (ligament 10). This trend can also be observed between other ligaments (i.e. the tibionavicular portion of the deltoid and the anterior tibiotalar portion of the deltoid).

7.5 Repeated Measure Analysis of Variance (ANOVA) & Cluster Analysis

7.5.1 RQ3: What are the interaction-effects between loads and ligaments?

From the ANOVA, table 18 was produced and highlights the various outputs of the Analysis of variance.

Table 18: Multivariate Tests[a]

Effect		Value	F	Hypothesis df	Error df	Sig.	Partial Eta Squared	Noncent. Parameter	Observed Power[d]
Load	Pillai's Trace	.047	1.044[b]	4.000	84.000	.389	.047	4.177	.316
	Wilks' Lambda	.953	1.044[b]	4.000	84.000	.389	.047	4.177	.316
	Hotelling's Trace	.050	1.044[b]	4.000	84.000	.389	.047	4.177	.316
	Roy's Largest Root	.050	1.044[b]	4.000	84.000	.389	.047	4.177	.316
Load * Ligament	Pillai's Trace	.682	1.625	44.000	348.000	.010	.170	71.516	.999
	Wilks' Lambda	.465	1.629	44.000	323.318	.010	.174	68.246	.998
	Hotelling's Trace	.866	1.624	44.000	330.000	.010	.178	71.465	.999
	Roy's Largest Root	.358	2.831[c]	11.000	87.000	.003	.264	31.140	.970

a. Design: Intercept + Ligament
Within Subjects Design: Load
b. Exact statistic
c. The statistic is an upper bound on F that yields a lower bound on the significance level.
d. Computed using alpha = .05

From table 18, it is evident the Load's interaction with the various Ligaments is statistically significant ($p<0.05$) and highlights the efficiency of the various aspects of the experimental design for the study. The load increments were successful in gauging the strain response highlighting the extensions &contractions of the ligaments. Moreover, the Partial Eta Squared (η^2) is the **proportion of variance accounted for** by some effect. In this study, about 17% of the extension/contraction of a ligament can be attributed to the load (Van den berg, 2017), and is a "large" effect size (Watson, 2017). Table 19 presents the Mauchly's Test of Sphericity (Leard Statistics n.d.).

Table 19: Mauchly's Test of Sphericity[a]

Within Subjects Effect	Mauchly's W	Approx. Chi-Square	df	Sig.	Epsilon[b]		
					Greenhouse-Geisser	Huynh-Feldt	Lower-bound
Load	.021	329.527	9	.000	.367	.419	.250

Tests the null hypothesis that the error covariance matrix of the ortho-normalized transformed dependent variables is proportional to an identity matrix.
a. Design: Intercept + Ligament
Within Subjects Design: Load
b. May be used to adjust the degrees of freedom for the averaged tests of significance. Corrected tests are displayed in the Tests of Within-Subjects Effects table.

From Table 19, test above is significant ($p<0.05$) so the assumption of Sphericity has not been met. Since Sphericity cannot be assumed, the Greenhouse-Geisser statistics was used which makes an adjustment to the degrees of freedom of the repeated measures ANOVA (Leard Statistics n.d.). Table 20 highlights that Greenhouse-Geisser correction was applied to the degrees of freedom and provides evidence that a significant ($p<0.05$) difference in ligament extension/contraction between the various loading conditions exists. The ANOVA findings are expressed in the following form: Load*Ligament interaction [$F(df_{Load*Ligament}, df_{Error(Load*Ligament)} = \text{Test statistic F}, p = \ldots]$

Table 20: Tests of Within-Subjects Effects

Source		Type III Sum of Squares	df	Mean Square	F	Sig.	Partial Eta Squared	Noncent. Parameter	Observed Power[a]
Load	Sphericity Assumed	.010	4	.003	1.937	.104	.022	7.748	.582
	Greenhouse-Geisser	.010	1.469	.007	1.937	.160	.022	2.846	.338
	Huynh-Feldt	.010	1.677	.006	1.937	.155	.022	3.248	.362
	Lower-bound	.010	1.000	.010	1.937	.168	.022	1.937	.280
Load * Ligament	Sphericity Assumed	.123	44	.003	2.115	.000	.211	93.040	1.000
	Greenhouse-Geisser	.123	16.160	.008	2.115	.011	.211	34.171	.967
	Huynh-Feldt	.123	18.448	.007	2.115	.007	.211	39.009	.980
	Lower-bound	.123	11.000	.011	2.115	.027	.211	23.260	.894
Error(Load)	Sphericity Assumed	.459	348	.001					
	Greenhouse-Geisser	.459	127.812	.004					
	Huynh-Feldt	.459	145.905	.003					
	Lower-bound	.459	87.000	.005					

a. Computed using alpha = .05

Hence, a repeated measures two-way ANOVA with a Greenhouse-Geisser correction showed that mean ligament extension/contraction differed significantly between load/condition points [$F(16.160, 127.812) = 2.115$, $p<0.05$].

Table 21 presents the mean extension/contraction of each ligament in the study for the four loads/conditions applied, and the corresponding Lower and Upper Bound of this mean. The 'Relative Change' was extrapolated from the Lower and Upper Bound values, and indicates the plausible extension/contraction which occurred in each ligament over the four loads/conditions. Clearly, ligament L10 (Plantar cuneometatarsal ligament) had the maximum relative change.

Table 21: Estimated Marginal Means

Ligament	Mean	Std. Error	95% Confidence Interval		Relative Change
			Lower Bound	Upper Bound	
L0 - Achilles Tendon	.020	.013	-.005	.046	0.051
L1 - Deltoid: Anterior Tibiotalar Pt.	-.014	.013	-.039	.012	0.051
L2 - Deltoid: Posterior Tibiotalar Pt.	.025	.013	.000	.051	0.051
L3 - Deltoid: Tibiocalcaneal Pt.	.040	.013	.015	.066	0.051
L4 - Deltoid: Tibionavicular Pt.	.022	.013	-.004	.047	0.051
L5 - Deltoid: Tibiospring Pt.	.020	.013	-.006	.045	0.051
L6 - Spring Ligament: Superomedial Calcaneonavicular	.003	.013	-.023	.029	0.052
L7 - Spring Ligament: Inferior Calcaneonavicular	-.014	.013	-.039	.012	0.051
L8 - Medial Talocalcaneal Ligament	.006	.013	-.020	.031	0.051
L9 - Plantar cuneonavicular ligament	-.005	.016	-.036	.026	0.062
L10 - Plantar cuneometatarsal ligament	-.038	.022	-.083	.006	0.089
L11 - Interosseous Indirect	.006	.013	-.019	.032	0.051

Moreover Table 22 further supports the use of linear increments of load and its effects on the various ligaments.

Table 22: Tests of Within-Subjects Contrasts

Source	Load	Type III Sum of Squares	df	Mean Square	F	Sig.	Partial Eta Squared	Noncent. Parameter	Observed Power[a]
Load	Linear	.009	1	.009	2.205	.141	.025	2.205	.312
Load * Ligament	Linear	.101	11	.009	2.197	.022	.217	24.166	.907
Error(Load)	Linear	.365	87	.004					

a. Computed using alpha = .05

Levene's test (Levene 1960)is used to test if the samples have equal variances. Equal variance across samples is called homogeneity of variance. Some statistical tests, for example the analysis of variance, assume that variances are equal across groups or samples(National Institute of Standards and Technology: U.S. Department of Commerce, n.d.).

Table 23 provides information to the Levene's Test of Equality Error Variances.

Table 23: Levene's Test of Equality of Error Variances[a]

	F	df1	df2	Sig.
F100_000N	.	11	87	.
F100_230N	2.851	11	87	.003
F100_460N	4.122	11	87	.000
F100_690N	3.343	11	87	.001
F100_920N	4.492	11	87	.000

Tests the null hypothesis that the error variance of the dependent v
a. Design: Intercept + Ligament
Within Subjects Design: Load

A value $p<0.05$ means that the variability in any two loads/conditions is NOT the same. That the extensions caused by one load/condition do vary significantly much more than the extensions with the second load/condition. This means that the variability in the two conditions is significantly different (thus, equal variance not assumed).

Table 24 presents the various ligaments and the extensions caused by the various loads/conditions. The values in this table are similar to the ones used to respond to Specific Research Questions 1 and 2.

Table 24: Ligament * Load

Ligament	Load	Mean	Std. Error	95% Confidence Interval	
				Lower Bound	Upper Bound
L0 - Achilles Tendon	1	.000	.000	.000	.000
	2	.010	.007	-.004	.023
	3	.012	.016	-.019	.043
	4	.029	.022	-.015	.072
	5	.050	.026	.000	.101
L1 - Deltoid: Anterior Tibiotalar Pt.	1	.000	.000	.000	.000
	2	.001	.007	-.012	.015
	3	-.009	.016	-.040	.022
	4	-.023	.022	-.066	.020
	5	-.038	.026	-.089	.013
L10 - Plantar cuneometatarsal ligament	1	.000	.000	.000	.000
	2	-.012	.012	-.035	.012
	3	-.045	.027	-.099	.009
	4	-.065	.038	-.140	.010
	5	-.071	.044	-.159	.017
L11 - Interosseous Indirect	1	.000	.000	.000	.000
	2	.002	.007	-.012	.015
	3	.005	.016	-.026	.036
	4	.014	.022	-.029	.057
	5	.011	.026	-.040	.062
L2 - Deltoid: Posterior Tibiotalar Pt.	1	.000	.000	.000	.000
	2	.009	.007	-.004	.023
	3	.026	.016	-.005	.057
	4	.042	.022	-.001	.085
	5	.049	.026	-.001	.100
L3 - Deltoid: Tibiocalcaneal Pt.	1	.000	.000	.000	.000
	2	.015	.007	.002	.029
	3	.053	.016	.022	.084
	4	.070	.022	.027	.113
	5	.063	.026	.012	.113
L4 - Deltoid: Tibionavicular Pt.	1	.000	.000	.000	.000
	2	-9.211E-5	.007	-.014	.013

	3	.018	.016	-.013	.049
	4	.039	.022	-.004	.082
	5	.051	.026	.000	.102
L5 - Deltoid: Tibiospring Pt.	1	.000	.000	.000	.000
	2	.005	.007	-.008	.019
	3	.020	.016	-.011	.051
	4	.026	.022	-.017	.069
	5	.047	.026	-.004	.098
L6 - Spring Ligament: Superomedial Calcaneonavicular	1	.000	.000	.000	.000
	2	.015	.007	.001	.028
	3	.017	.016	-.014	.048
	4	.002	.022	-.041	.046
	5	-.019	.026	-.069	.032
L7 - Spring Ligament: Inferior Calcaneonavicular	1	.000	.000	.000	.000
	2	-.001	.007	-.014	.013
	3	-.009	.016	-.040	.022
	4	-.026	.022	-.069	.017
	5	-.032	.026	-.082	.019
L8 - Medial Talocalcaneal Ligament	1	.000	.000	.000	.000
	2	-.005	.007	-.019	.008
	3	-.001	.016	-.032	.030
	4	.016	.022	-.027	.059
	5	.018	.026	-.033	.069
L9 - Plantar cuneonavicular ligament	1	.000	.000	.000	.000
	2	-.019	.008	-.036	-.003
	3	-.024	.019	-.062	.014
	4	.017	.027	-.036	.070
	5	.001	.031	-.061	.063

7.5.2 RQ4: How are the various ligaments clustered and respond in a similar manner?

To answer Specific Research Question 4, a Cluster (Hierarchical) Analysis was undertaken. Table 25 provides the dissimilarity matrix, which is the degree of dissimilarity (or similarity) determined from the recorded values for one or multiple characteristics for the cases/ligaments. For example ligament L1 (Deltoid: Anterior Tibiotalar Pt.) is relatively dissimilar to ligament L3 (Deltoid: Tibiocalcaneal Pt.) compared to ligament L7 (Spring Ligament: Inferior Calcaneonavicular).

Table 25: Proximity Matrix (**dissimilarity matrix)**

	Squared Euclidean Distance											
Case	1:L0	2:L1	3:L2	4:L3	5:L4	6:L5	7:L6	8:L7	9:L8	10:L9	11:L10	12:L11
1:L0 - Achilles Tendon	.000	.011	.000	.004	.000	.000	.006	.010	.002	.005	.027	.002
2:L1 - Deltoid: Anterior Tibiotalar Pt.	.011	.000	.013	.023	.013	.011	.002	.000	.005	.004	.004	.004
3:L2 - Deltoid: Posterior Tibiotalar Pt.	.000	.013	.000	.002	.000	.000	.006	.012	.003	.006	.031	.003
4:L3 - Deltoid: Tibiocalcaneal Pt.	.004	.023	.002	.000	.003	.003	.012	.022	.008	.014	.046	.008
5:L4 - Deltoid: Tibionavicular Pt.	.000	.013	.000	.003	.000	.000	.006	.012	.002	.005	.030	.002
6:L5 - Deltoid: Tibiospring Pt.	.000	.011	.000	.003	.000	.000	.005	.010	.001	.005	.027	.002
7:L6 - Spring Ligament: Superomedial Calcaneonavicular	.006	.002	.006	.012	.006	.005	.000	.002	.002	.003	.012	.001
8:L7 - Spring Ligament: Inferior Calcaneonavicular	.010	.000	.012	.022	.012	.010	.002	.000	.004	.003	.004	.004
9:L8 - Medial Talocalcaneal Ligament	.002	.005	.003	.008	.002	.001	.002	.004	.000	.001	.016	.000
10:L9 - Plantar cuneonavicular ligament	.005	.004	.006	.014	.005	.005	.003	.003	.001	.000	.012	.001
11:L10 - Plantar cuneometatarsal ligament	.027	.004	.031	.046	.030	.027	.012	.004	.016	.012	.000	.016
12:L11 - Interosseous Indirect	.002	.004	.003	.008	.002	.002	.001	.004	.000	.001	.016	.000

As recommended by (Mooi & Sarstedt 2011, p.253), a dendogram provides the visual representation of the similarity/dissimilarity matrix. Figure 57 is the dendogram of the average linkage between groups, and which displays the distance level at which there was a combination of objects/ligaments and clusters.

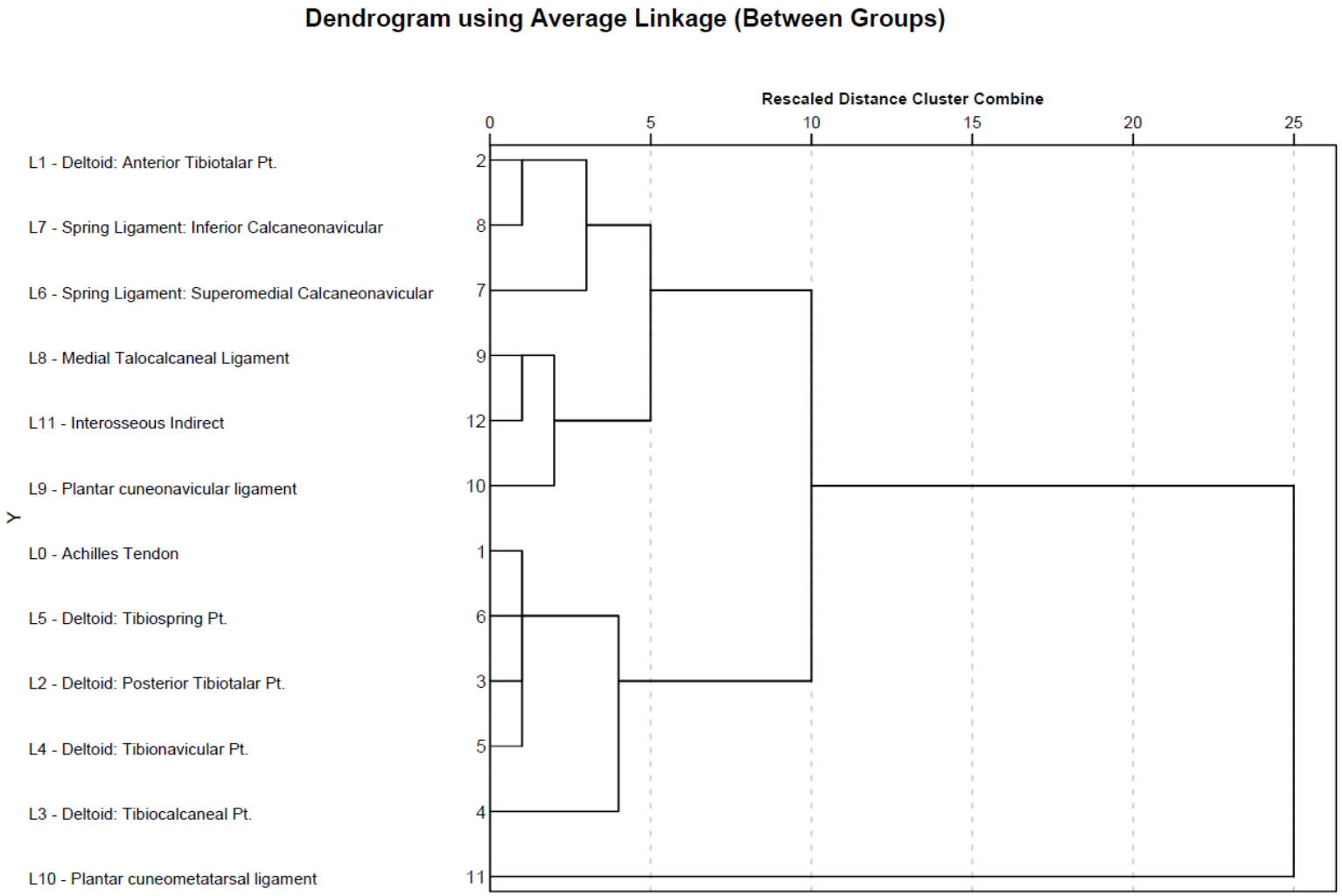

Figure 57: Dendogram of the average linkage between ligaments and groups

The dendogram illustrates the average arrangement of clusters between the and groups them based on the similarity of their strain response. This provides a valuable description of the association between the ligaments and their functional interdependence. As depicted in the dendogram, ligament L1 (Deltoid: Anterior Tibiotalar Pt.) is grouped with L7 (Spring Ligament: Inferior Calcaneonavicular) at the first level. Upon reference to the graph displaying the average strain response at the incremental loads (Figure 56), it can be observed that there is a similarity in the strain response exhibited for these two ligaments. This clustering of the associated ligaments based on their strain response can be identified for other ligaments as well and related to the average strain response graphs (Figure 56).
From the dendogram can also be identified that the Achilles tendon has an association with all of the ligaments of the medial column.

7.6 Summary of Findings

From the stereoradiographs captured through the progressive simulation of the physical characteristics of AAFD, the positions of the tantalum markers at the attachment sites of the ligaments of the medial column were able to be digitally tracked in 3 dimensional spaces. Furthermore, the displacements of the markers occurring between the incremental loads were calculated, from which a 3 dimensional vector map was generated to illustrate this. Moreover, from this sequential displacement data, the average strain response along the length of the ligament could be calculated at the incremental loads applied, through the progression of the physical characteristics of AAFD. These results give an indication into the sequential involvement of the medial column ligaments during the progression of the physical deformity.

Through conducting a repeated measures 2-way analysis of variance (ANOVA), it was identified that the loads interaction with the various ligaments was statistically significant ($p<0.05$), which highlights the efficiency of the various aspects of the experimental design.

In addition, the Greenhouse-Geisser correction obtained from the ANOVA highlighted that there was a statistical difference between the mean strain response of the ligaments and the different loading conditions applied.

From Levene's test of equality of Error Variances, the value of ($p<0.05$) at each incremental loading condition indicated that the variance was statistically significant, hence highlighting that the strain response of the ligaments varied significantly between the loads applied.

The cluster analysis undertaken assessed the similarity between each ligaments strain response. The dendogram produced from the results illustrated the average arrangement of clusters between the ligaments and grouped them based on the similarity of their strain response. From the dendogram, associations between the different ligaments could be identified. Additionally, from the results obtained, the displayed association between the achilles tendon and all of the medial column ligaments was supportive of literature describing the functional physiologic mechanics of the foot during gait. This further highlighted the association and interdependent nature of the ligaments within the foot.

Chapter 8: Discussion

8.1 Discussion of Results – Theoretical explanations

8.1.1 3D Vector Map of Simulation Displacements

From the vector map, clinical characteristics of AAFD could be identified through comparison of the displacements occurring at the key anatomical landmarks and structures within the foot (i.e. flattening of the longitudinal arch, hindfoot valgus and forefoot abduction)

It should be noted that in the experimental set up, the base of the foot was not constrained to the base plate in order to allow the foot to naturally and freely splay out. Due to this, as the physical deformity was induced, there was some small translation of the foot along the base plate (recorded as ~2mm from the hexapod‘s real time system position feedback) towards the medial side of the ankle. When comparing the positions of the markers to one another and plotting the displacement vector map, this can be identified by a majority of the vectors having a considerable component in the positive Y direction.

In considering the small degree of sliding of the foot specimen, the component of the markers displacement existing as a result of the sliding would be uniform among all of the markers.

When calculating the strain response of the ligaments, pairs of beads corresponding to a particular ligament (or portion of a ligament) were matched together by the MATLAB program. In doing so, the contractions and elongations of a ligament could be calculated without the influence of the slight slip of the foot along the base plate.

8.1.2 RQ1

From the strain responses of the medial column ligaments, it was identified that some of the ligaments were elongating, while others were contracting, hence demonstrating that the ligaments are not independent of one another and play interrelated roles in the attempt to maintain effective overall function and stability of the foot and ankle.

From table 17, at each applied load, the recorded strains can be compared with normal stress strain behavior for ligaments. With reference to the stress strain curve for ligaments introduced in the literature review (Chapter 3, Section 3.17), the toe region of the curve represents the "un crimping" of collagen fibrils and ends at approximately 2% ($\varepsilon = 0.02$), where all crimpled fibers straighten (Hammer 2007). Following this, the linear elastic region describes strain of the collagen fibers which can be recovered and is in effect when the strain is less than 4% ($\varepsilon < 0.04$). When the strain of the ligaments collagen fires are between 4%-8% ($0.04 < \varepsilon < 0.08$)(Robi et al. 2013), the collagen fibers begin to slide past one another as the cross links existing between the fibers begin to fail, resulting in microtears (microscopic failure) within the ligament. After this point, if the strain is above 8% ($\varepsilon > 0.08$), macroscopic failure of the ligament is imminent (Hammer 2007).

From the recorded values, the strain response of the ligaments at each load can be compared to the general strain values of the stress strain response curve for ligaments. It can be noted that at the 2nd loadstep applied (460N), the tibiocalcaneal portion of the deltoid ligament (L3) is experiencing an average strain response across the ligament of $\varepsilon = 0.0526974$. As described by Robi et al, this lies within the linear region of the stress strain response curve for ligaments. Furthermore, as the recorded strain is above 4% ($\varepsilon > 0.04$), it is suggested that at this point, the natural crimp of the collagen fibrils have been permanently lost and as the collagen fibers slide past one another, the cross links between fibers begin to fail (i.e. microtears within the ligament) (Robi et al. 2013).

As the loads are increased, there is a general increase in the strain response of the ligaments. At a load of 690N, where the physical AAFD was more pronounced, the strain of L3 continued to increase ($\varepsilon = 0.06996989$), approaching the "progressive failure" region ($\varepsilon > 0.08$) described by Hammer et al (2017), where micro-failure of the collagen fibres begin to occur, and unrecoverable elongation of the ligament begins to occur. It can also be noted that

at this loadstep, the posterior tibiotalar portion of the deltoid (L2) experiences a strain response of ε = 0.04192411, just above a strain of 4%.

Similarly, as the load was increased further to 920N and the physical characteristics observable in a stage IV flatfoot was simulated; more ligaments recorded a strain exceeding the 4% point of the linear region of the stress strain curve. These ligaments included the posterior tibiotalar, tibiocalcaneal, tibionavicular and tibiospring portions of the deltoid ligament.

8.1.3 RQ2

A plot of the average strains of the medial column ligaments at the incremental loads, illustrated the strain response behavior of the ligaments as the deformity was produced (Figure 56).

From the accumulative strain responses displayed, the similarity and association between the strain response of the tibiocalcaneal portion of the deltoid ligament (ligament 3) and the plantar cuneometatarsal ligament (ligament 10) was noted. This trend could also be observed between other ligaments (i.e. the tibionavicular portion of the deltoid and the anterior tibiotalar portion of the deltoid). This extension of some ligaments and contraction of others, reiterates that the ligaments are not independent of one another and are collectively involved in maintaining the overall structure, function and stability of the foot and ankle.

When the plots were subjected to the spline curve function in SPSS to highlight the non-linearity of the strain response of soft tissue (Holzapfel, 2000), similarities in the shape of the accumulative strain response curve could be drawn to the biomechanical stress strain response of ligaments and tendons illustrated below in figure 58. This observation is an interesting display as it illustrates a typical strain response behavior of connective tissues/ligaments.

[Figure has been removed due to copyright restrictions]

Figure 58: Stress Strain Response for Ligament and Tendons
Retrieved from Robi, K. et al., 2013. The Physiology of Sports Injuries and Repair Processes. In Current Issues in Sports and Exercise Medicine. Intech, pp. 43–77. Available at:

8.1.4 RQ3

The data collected during the experiment was obtained from the implementation of the RSA technique. In this project, the technique involved various stages, all of which were imperative for the collection and analysis of data. These stages included; the design and fabrication of the RSA base plate calibration frame, the calibration of the frame itself, the post processing of the stereoradiographs, as well as the digitization & 3D transformation methods and algorithms implemented within the RSA MATLAB script.

Upon reference to Table 7.4 obtained from the ANOVA, it is evident that the loads interaction with the various ligaments was statistically significant ($p<0.05$), which highlights the efficiency of the various aspects of the experimental design.

Furthermore, the Greenhouse-Geisser correction obtained from the ANOVA highlighted that there was a statistical difference between the mean strain response of the ligaments and the different loading conditions applied. Moreover, Levene's test of equality of Error Variances highlighted that the variance at each incremental loading condition was not the same ($p<0.05$). This demonstrates that the strain response of the ligaments varied significantly between the loads applied, thus providing a statistical validation of the sequential recruitment patterns observable from the strain response curves of the ligaments in Figure 56

8.1.5 RQ4

From the produced dendogram, a statistical and illustrative description is provided of the association between the ligaments and their functional interdependence to collectively maintain stability the foot and ankle. An important observation from the displayed associated ligaments is that that the Achilles tendon is recorded to have an association with all of the ligaments. From the literature, it is understood that during normal gait, tension within the Achilles tendon during dorsiflexion allows the plantar fascia to tighten, shortening the distance between the metatarsals and the calcaneus thus elevating the medial longitudinal arch of the foot (i.e. the windlass mechanism)(Bolgla & Malone 2004; Bonnefoy-Mazure & Armand 2015) Considering this, the association between the Achilles tendon and the other ligaments of the medial column described by the dendogram is supportive this aspect of the physiological

behavior of ligaments within the foot and further highlights the association and interdependent nature of the ligaments within the foot.

8.2 Limitations

Through this project, there were several limitations present. One of these limitations involved the tension applied to the achilles tendon. As mentioned in Chapter 4, section 4.6, due to time constraints involving the duration of the project, the design and fabrication of a mechanical system to apply a constant vertical tension to the achilles tendon (similar to that which is physiologically experienced within the body) was not feasible. As a result, a nominal tension was applied to the achilles tendon via fixation to the same top cup used across the specimens and the strain response of the tendon simultaneously tracked alongside the ligaments of the medial column. This would have resulted in some variability between the initial tension within the Achilles tendon between specimens and may have impacted the accuracy of the strain response values recorded.

Upon capturing the stereoradiographs during testing, as the medial longitudinal arch was progressively flattened and foot splayed out, for larger specimens and at higher loadsteps, it was not possible to capture the markers located most proximal of the foot specimen (closest to the x-ray collimator) within the field of view. This was due to the small distance from these markers to the x-ray collimator and the angle at which the x-rays were taken.

As explained in Chapter 4, section 4.4.1, the conceptualization of the base plate design was based on a similar design implemented by Bass (2014) & Garcia (2015) to measure the strain within the ACL of sheep knee specimens (Bass 2014; Garcia 2015). Although the general conception of the calibration rods was adapted from Bass & Garcia's study, for foot and ankle testing, the base plate had to be redesigned to fit feet specimens, resulting in a larger base plate calibration frame.

For the fabrication of the design, the base plate calibration frame was 3D printed (Ultimaker 2+) in ABS due to the consideration that the slight surface roughness of the printed material would minimize excessive slip of the foot specimen upon the base plate. As the Ultimaker 2+ consists of a build platform smaller than that of the base plate design, the base plate had to be 3D printed in parts and attached together via nylon screws and high strength plastic adhesive.

While this seemed to provide structural strength and stiffness of the base plate during early testing of the specimens, upon testing the last few specimens, a slight amount of bending was observed at the front of the base plate (supporting the forefoot).

The bending resulted in a deviation of the front RSA calibration rod (calibration rod X; refer to figure 33) away from the vertical axis and was observable from the stereoradiographs of the last few specimens at the last 2 loadsteps (690 N, 920 N). Although this was digitally corrected in post processing via Adobe Photoshops calibrated measurement and alignment tools, the bending of the front of the base plate may have introduced some error in the accuracy of the coordinate positions extracted from the stereoradiographs at the higher loads for some of the specimens.

For the experiments conducted in this project, each fresh frozen specimen was thawed prior to dissecting and implanting the tantalum markers within the foot. The prepared specimens were then frozen again, only to be thawed when testing was to be conducted.

From a review of fresh frozen cadaver studies, it has been concluded that the one-time freezing of human cadaveric tissue maintains the integrity of the biological tissue and in that respect is virtually harmless (Klop et al, 2017). With increasing freeze-thaw cycles however, there is a decline in the integrity of the biological soft tissue.

In a study conducted by Huang et al (2011), investigating the effects of repetitive freeze thaw cycles on the biomechanical properties of tendons within the body, it was found that an increase in the number of freeze cycles resulted in a decrease in the overall biomechanical integrity of the soft tissues. For freeze thaw cycles under 3, the biomechanical properties were similar to the group of fresh specimens (Hung et at, 2011).

In this study, the number of freeze-thaw cycles were to be minimized in order to preserve the structural and biomechanical integrity of the soft tissue structures. As each specimen required considerable time in the dissection and implantation of the specimens, the specimens had to be thawed once prior to their preparation, and once again prior to testing.

It is possible that this may influence the resulting ligament strains, however, the effects of this were minimized by using a low number of freeze-thaw cycles. Evidence of this is supported in literature (Hung et al, 2011; Klop et al, 2017, Jung et al, 2011).

To further increase reliability of results, one may dissect and implant the markers within the specimen on the day of testing. This however would take considerable time and was a limitation of this project, given the time constraints.

Additionally, the reliability of the results obtained can be improved by increases the sample size of the specimens tested. Standard deviations and standard errors are sample-size dependent (Hoffman 2015; Johnson 2018; Levene 1960; Peck, Olsen & Devore, 2016)). This study acknowledges the small sample size (n=9), and the time constraints of a nine-month project is a limitation. An important recommendation for future research is to increase the sample size (perhaps n=30) which will impact on the standard deviation and/or standard error of measurement.

Another limitation of the experiment arises from the measurement techniques available and the anatomical complexity of the foot and ankle.

With the ligaments of the foot and ankle, there are numerous soft tissue structures which interconnect with one another. In anatomy textbooks, the ligamentous structures of the foot and ankle are clearly defined, however within the body, there are some interconnections and wrapping of the fibres of different ligaments to one another. This presents a complex anatomical structure to analyze, and whilst care was taken by orthopaedic foot and ankle specialists during the implantation of the tantalum markers at the ligament attachment sites within the foot, the ligament wrapping that is present in the anatomical foot may influence the mechanics of measuring the strains across individual ligaments as defined by textbook anatomy.

Furthermore, in the cadaveric specimens, the ligaments within the foot and ankle are under some degree of initial tension to hold the structures of the foot in its position. As such, the ligaments exhibit a residual strain even when no loads have been applied yet. To measure the absolute strain of each ligament in their resting positions, the ligaments must be dissected such that their initial resting lengths can be measured and used as an initial stain value. This experiment was designed to be as minimally obstructive to the structures of the foot and ankle complex as possible, such that the movements of the foot and ankle could be simulated as closely as possible as to a living anatomical case. To do this, care was taken to not damage the ligaments of the foot during dissection. Due to this, the ligaments were not dissected to record original lengths, and the changes in length under the applied loads were measured. Hence, the

relative strain of the ligaments was measured as opposed to measuring the absolute strains. This project may be further developed in future experiments by dissecting the ligaments of separate cadaveric specimens and measuring the original resting lengths, which can be used as initial strain values.

Chapter 9: Conclusions

9.1 Future Work

As displayed in the results section of the dissertation, the lines of work involved in this dissertation successfully demonstrated feasibility of the developed experimental design, which was validated by the statistical significance of the results obtained. The physical characteristics of AAFD were successfully progressively produced in cadaveric models and the strain recruitment patterns of the medial column ligaments measured as well as evaluated during progression of the physical deformity. Furthermore, the associations between the strain responses of different ligaments were highlighted through the cluster analysis performed.

In spite of this, further research is still required to improve upon the systems implemented in this dissertation, thus evaluating the orthopaedic biomechanics of the foot and ankle with increased accuracy and reliability.

A key area for further research includes increasing the accuracy and reliability of the strain response data obtained. This could be achieved through the design of a mechanical pulley system that applies a constant tension to the Achilles tendon within a physiological range, independent of the hexapods control system. This would better simulate the physiological conditions within the body and thus allow for the specimens to behave in a manner that more closely resembles the anatomical movements that occur in living physiological conditions.

Another aspect of the project which could be investigated in future work is the influence of scaling applied loadsteps for each specimen. In the project undertaken, as the base plate calibration frame was constructed out of a plastic (radiopaque) material, the forces exerted upon the base plate were not to be high enough that the plate would risk mechanical fracture. As a preliminary investigation, the scaling of the loadsteps to each specimen may have resulted in unpredictable mechanical behavior of the designed base plate and hexapod robot.

Moreover, It was noted during pilot tests that under a load of 920N (maximum load applied), the encoder legs of the hexapod robot became exceedingly close to the x-ray cassettes during image capture, to the point where increasing the loadsteps further would have resulted in insufficient space for the x-ray cassette to fit in the designed cassette holder.

Additionally, the investigation was around the degree of influence that the induced physical deformity had on the strains of the medial column ligament. In this respect, the applied load steps were held constant among specimens and not scaled. Due to the preliminary method of applying the nominal tension to the Achilles tendon, scaling the loads to each specimen, used in conjunction with the preliminary method of Achilles tension implemented in this experiment, would have introduced another complexity and thus unreliability of the results obtained. To counteract this, a full Achilles tension system with a real time measurement system (via load cell) was to be designed, however, due to the time constraints of a nine month project, this was unfeasible on top of the substantial experimental design already devised. As such, this is an identified area for future work.

9.2 Clinical relevance

An understanding of the contribution of the ligaments during the onset of AAFD is essential for optimizing the management of symptomatic AAFD. Based on the strain response findings from this study, it is suggested that more attention be given to the deltoid ligament during all stages of AAFD. Based on this, another key area for further research includes assessing the effectiveness of various procedures used to correct the deformity, particularly ligament augmentation reconstructions of the medial column ligaments.

9.3 Summary

The research aims of this dissertation were to investigate the ‘sequential biomechanical involvement of the medial column ligaments in Adult Acquired Flatfoot Deformity’. This involved the successful formulation and validation of the experimental design in its constituent stages and subsequent testing protocols developed.

The simulation of the physical characteristics of the deformity was successfully progressively induced through application of incremental loading conditions from which the strain response of the medial column ligaments and Achilles tendon could be calculated and statistically analyzed. The efficiency of the various aspects of the experimental design was highlighted by

the high statistical significance ($P<0.05$) of the interactions between the strain response of the ligaments and the incremental loads applied.

Upon the collection of data from the designed experimental system, the research was investigated through addressing 4 specific research questions. From the analysis of these results, the sequential involvement of the medial column ligaments during the progression of the physical deformity was successfully evaluated and the association between the various ligaments investigated.

The results provided information on the behavior and operation of the ligaments during the progression of AAFD which were not previously known.

The new found information suggests that the deltoid ligament experiences a reduction in its mechanical integrity before the spring ligament.

Currently, little attention is given to the deltoid ligament during the early stages of AAFD however, and the spring ligament is much more commonly addressed. The findings from the study are aligned with newer literature that the deltoid ligament does play an important and underrated role in the progression of AAFD.

The outcomes from this study require further investigation, however, the findings may potentially aid in improving the outcomes of clinical treatments for AAFD.

References

Abousayed, M. et al., 2017. Adult-Acquired Flatfoot Deformity: Etiology, Diagnosis, and Management. *JBJS Reviews*, 5(8), p.e7l; p1-9.

Abousayed, M.M. et al., 2016. Classifications in Brief: Johnson and Strom Classification of Adult-acquired Flatfoot Deformity. *Clinical Orthopaedics and Related Research*, 474(2), pp.588–593.

Acevedo, J. & Beskin, J., 1998. Complications of Plantar Fascia Rupture Associated with Corticosteroid Injection. *Foot & Ankle International*, 19(2), pp.91–97.

American Orthopaedic Foot & Ankle Society, Acquired Adult Flatfoot Deformity. Available at: http://www.aofas.org/footcaremd/conditions/ailments-of-the-midfoot/Pages/Acquired-Adult-Flatfoot-Deformity.aspx [Accessed June 28, 2017].

Aquino, A. & Payne, C., 2001. Function of the Windlass Mechanism in Excessively Pronated Feet. *Journal of the American Podiatric Medical Association*, 91(5), pp.245–250.

Arms, S.W. et al., 1984. The biomechanics of anterior cruciate ligament rehabilitation and reconstruction. *The American journal of sports medicine*, 12(1), pp.8–18.

Barber Foss, K.D. et al., 2009. Generalized joint laxity associated with increased medial foot loading in female athletes. *Journal of Athletic Training*, 44(4), pp.356–362.

Bass, D., 2014. *Replication Of Knee Joint Motions Using A State Of The Art 6 Degrees Of Freedom Hexapod Robot To Test Anterior Cruciate Ligament Loading*. Flinders University, South Australia.

Bates, N. et al., 2015. A Novel Methodology for the Simulation of Athletic Tasks on Cadaveric Knee Joints with Respect to In Vivo Kinematics. *Ann Biomed Eng*, 43(10), pp.2456–2466.

Baxter, J.R. et al., 2015. Reconstruction of the medial talonavicular joint in simulated flatfoot deformity. *Foot & ankle international*, 36(4), pp.424–429.

Betsch, M. et al., 2011. Influence of foot positions on the spine and pelvis. *Arthritis Care & Research*, 63(12), pp.1758–1765.

Blann, A., 2015. *Data Handling and Analysis: Fundamentals of Biomedical Science*, London:

Oxford University Press.

Bluman, E. & Myerson, M., 2007. Stage IV Posterior Tibial Tendon Rupture. *Foot & Ankle Clinics*, 12(2), pp.341–362.

Bolgla, L.A. & Malone, T.R., 2004. Plantar Fasciitis and the Windlass Mechanism: A Biomechanical Link to Clinical Practice. *Journal of Athletic Training*, 39(1), pp.77–82.

Bonnefoy-Mazure, A. & Armand, S., 2015. Normal Gait. In F. Canavese & J. Deslandes, eds. *Orthopedic Management of Children with Cerebral Palsy*. Nova Science Publishers, Inc.

Bonnel, F. et al., 2010. Chronic ankle instability: Biomechanics and pathomechanics of ligaments injury and associated lesions. *Orthopaedics and Traumatology: Surgery and Research*, 96(4), pp.424–432.

Borzage, M. et al., 2017. Measuring Stroke Volume: Impedance Cardiography vs Phase-Contrast Magnetic Resonance Imaging. *American Journal of Critical Care*, 26(5), pp.408–415.

Bottner, F. et al., 2005. Radiostereometric Analysis: The Hip. *HSS Journal*, 1(1), pp.94–99. Available at: http://link.springer.com/10.1007/s11420-005-0114-2.

Bragdon, C., O'Keefe, M. & Harris, W., 2003. Radiostereometric Analysis (RSA) Studies at Massachusetts General Hospital. *Orthopaedic Biomechanics and Biomaterials Laboratory, Massachusetts General Hospital, Boston MA*, pp.104–107. Available at: http://orthojournalhms.org/volume5/manuscripts/ms12.htm.

Braito, M. et al., 2016. Comparison of preoperative MRI and intraoperative findings of posterior tibial tendon insufficiency. *SpringerPlus*, 5(1), p.1414. Available at: http://springerplus.springeropen.com/articles/10.1186/s40064-016-3114-4.

Brockett, C.L. & Chapman, G.J., 2016. Biomechanics of the ankle. *Orthopaedics and Trauma*, 30(3), pp.232–238. Available at: http://dx.doi.org/10.1016/j.mporth.2016.04.015.

Butler, D.L. et al., 1992. Location-dependent variations in the material properties of the anterior cruciate ligament. *Journal of Biomechanics*, 25(5), pp.511–518.

Carmody, D. et al., 2015. Posterior tibial tendon dysfunction: An overlooked cause of foot deformity. *Journal of Family Medicine and Primary Care*, 4(1), p.26. Available at:

http://www.jfmpc.com/text.asp?2015/4/1/26/152245.

Carr, J.B., Yang, S. & Lather, L.A., 2016. Pediatric Pes Planus: A State-of-the-Art Review. *Pediatrics*, 137(3), pp.e20151230–e20151230. Available at: http://pediatrics.aappublications.org/cgi/doi/10.1542/peds.2015-1230.

Chinn, L. & Hertel, J., 2010. Rehabilitation of Foot and Ankle Injuries in Athletes. *Clinical sports medicine*, 29(1), pp.157–167. Available at: http://europepmc.org/abstract/MED/9257040.

Chu, I. et al., 2001. Experimental flatfoot model: The contribution of dynamic loading. *Foot & Ankle International*, 22, pp.220–225.

Crary, J.L., Hollis, J.M. & Manoli, A., 2003. The effect of plantar fascia release on strain in the spring and long plantar ligaments. *Foot & ankle international / American Orthopaedic Foot and Ankle Society [and] Swiss Foot and Ankle Society*, 24(3), pp.245–50. Available at: http://www.ncbi.nlm.nih.gov/pubmed/12793488.

Dasgupta, B. & Mruthyunjaya, T.S., 2000. Stewart platform manipulator: A review. *Mechanism and Machine Theory*, 35(1), pp.15–40.

Deland, J.T. et al., 2005. Posterior tibial tendon insufficiency: which ligaments are involved? *Foot & ankle international / American Orthopaedic Foot and Ankle Society [and] Swiss Foot and Ankle Society*, 26(6), pp.427–435.

Deland, J.T. et al., 2006. Posterior tibial tendon insufficiency results at different stages. *HSS journal : the musculoskeletal journal of Hospital for Special Surgery*, 2(2), pp.157–160.

Denise, L., Moreira, F. & Oliveira, M.L. De, 2014. Physical exercise and osteoporosis: effects of different types of exercises on bone and physical function of postmenopausal women. , 58(5).

DiGiovanni, C. & Greisberg, J., 2007. Adult Acquired Flatfoot. In *Core Knowledge in Orthopaedics: Foot and Ankle*. Mosby, Elsevier, pp. 42–44.

Ding, B., 2014. *A Study of a Gough-Stewart Platform- based Manipulator for Applications in Biomechanical Testing*. The University of Adelaide. Available at: PhD Thesis.

Ding, B. et al., 2011. Real-time FPGA Control of a Hexapod Robot for 6- DOF Biomechanical

Testing. *IECON 2011 - 37th Annual Conference on IEEE Industrial Electronics Society*, pp.252–257. Available at: http://ieeexplore.ieee.org/stamp/stamp.jsp?tp=&arnumber=6119320&isnumber=6119266

Dinov, I.D., 2016. Methodological challenges and analytic opportunities for modeling and interpreting Big Healthcare Data. *GigaScience*, 5(12), pp.1–15.

Donatelli, R. a, 1985. Normal biomechanics of the foot and ankle. *The Journal of orthopaedic and sports physical therapy*, 7(3), pp.91–95.

Erol, K. et al., 2015. An important cause of pes planus: the posterior tibial tendon dysfunction. *Clinics and Practice*, 5(1), pp.2–4. Available at: http://www.clinicsandpractice.org/index.php/cp/article/view/699.

Fleming, B.C. & Beynnon, B.D., 2004. In vivo measurement of ligament/tendon strains and forces: A review. *Annals of Biomedical Engineering*, 32(3), pp.318–328.

Fraser, J.J., Feger, M.A. & Hertel, J., 2016. Midfoot and Forefoot Involvement in Lateral Ankle Sprains and Chronic Ankle Instability. Part 1: Anatomy and Biomechanics. *International journal of sports physical therapy*, 11(6), pp.992–1005. Available at: http://www.ncbi.nlm.nih.gov/pubmed/27904801%5Cnhttp://www.pubmedcentral.nih.gov/articlerender.fcgi?artid=PMC5095951.

Frost, H.M., 1994. Wolff's Law and bone's structural adaptations to mechanical usage: an overview for clinicians. *Angle Orthodontist*, 64(3), pp.175–188.

Garcia, M., 2015. *Identification of ACL strain during complex movements*. Flinders University, South Australia.

Geideman, W.M., 2000. Posterior Tibial Tendon Dysfunction. , (2), pp.68–77.

Van Gestel, L., Van Bouwel, S. & Somville, J., 2015. Surgical treatment of the adult acquired flexible flatfoot. *Acta Orthopaedica Belgica*, 81(2), pp.172–183.

Gillen, C., 2014. Form Follows Function. In *The Hidden Mechanics of Exercise*. Harvard University Press, p. 24.

Goldsmith, M.T. et al., 2015. Validation of a six degree-of-freedom robotic system for hip in vitro biomechanical testing. *Journal of Biomechanics*, 48(15), pp.4093–4100. Available

at: http://dx.doi.org/10.1016/j.jbiomech.2015.10.009.

Griffin, M. et al., 2016. Biomechanical Characterization of Human Soft Tissues Using Indentation and Tensile Testing. *Journal of Visualized Experiments*, (118), pp.1–8. Available at: http://www.jove.com/video/54872/biomechanical-characterization-human-soft-tissues-using-indentation.

Guelfi, M. et al., 2017. Anatomy , pathophysiology and classification of posterior tibial tendon dysfunction. *European Review for Medical and Pharmacological Sciences*, 21, pp.13–19.

Guo, Y. et al., 2013. Selecting a sample size for studies with repeated measures. *BMC Medical Research Methodology*, 13(100), pp.1–8.

Halabchi, F. et al., 2013. Pediatric flexible flatfoot; Clinical aspects and algorithmic approach. *Iranian Journal of Pediatrics*, 23(3), pp.247–260.

Hammer, W., 2007. The Effect of Mechanical Load on Soft Connective Tissues. In *Functional Soft-tissue Examination and Treatment by Manual Methods*. Massachusetts, USA: Jones & Bartlett Learning, pp. 16–20.

Henning, C.E., Lynch, M. a & Glick, K.R., 1985. An in vivo strain gage study of elongation of the anterior cruciate ligament. *The American journal of sports medicine*, 13, pp.22–26.

Hiller, L. & Pinney, S.J., 2003. Surgical treatment of acquired flatfoot deformity: what is the state of practice among academic foot and ankle surgeons in 2002? *Foot & ankle international*, 24(9), pp.701–705.

Hodler, J. et al., 2017. Musculoskeletal Diseases. In pp. 25–31.

Hoffman, J.I.., 2015. *Biostatistics for Medical and Biomedial Practitioners*, Amsterdam: Elsevier.

Holzapfel, G., 2000. Biomechanics of Soft Tissue. *Graz University of Technology: Institute for Structural Analysis - Computational Biomechanics*, (7), pp.1–9.

Houglum, P. & Bertoli, D., 2012. *Brunnstrom's clinical kinesiology*, F.A. Davis Company.

Huang, C.K. et al., 1993. Biomechanical evaluation of longitudinal arch stability. *Foot & ankle*, 14, pp.353–357.

Huang, H. et al., 2011. Effects of repetitive multiple freeze-thaw cycles on the biomechanical properties of human flexor digitorum superficialis and flexor pollicis longus tendons. *Clinical Biomechanics*, 26(4), pp.419–423. Available at: http://dx.doi.org/10.1016/j.clinbiomech.2010.12.006.

Ilango, V., Subramanian, R. & Vasudevan, V., 2011. Cluster Analysis Research Design model, problems, issues, challenges, trends and tools. *International Journal on Computer Science and Engineering (IJCSE)*, 3(8), pp.3064–3070.

Imhauser, C.W. et al., 2002. Biomechanical evaluation of the efficacy of external stabilizers in the conservative treatment of acquired flatfoot deformity. *Foot & ankle international / American Orthopaedic Foot and Ankle Society [and] Swiss Foot and Ankle Society*, 23(8), pp.727–737.

Jarvis, H., 2014. Investigation of the Podiatric Model of Foot Biomechanics. *PHD Thesis*.

Jennings, M.M. & Christensen, J.C., 2008. The Effects of Sectioning the Spring Ligament on Rearfoot Stability and Posterior Tibial Tendon Efficiency. *Journal of Foot and Ankle Surgery*, 47(3), pp.219–224.

Johanson, M.A. et al., 2006. Heel lifts and the stance phase of gait in subjects with limited ankle dorsiflexion. *Journal of Athletic Training*, 41(2), pp.159–165.

Johnson, K.A. & Strom, D.E., 1989. Tibialis posterior tendon dysfunction. *Clin Orthop Relat Res.*, 239, pp.196–206.

Johnson, R.A., 2018. *Probability and Statistics for Engineers* 9th ed., Boston: Pearson.

Jung, H.-J. et al., 2011. The effects of multiple freeze-thaw cycles on the biomechanical properties of the human bone-patellar tendon-bone allograft. *Journal of Orthopaedic Research*, 29(8), pp.1193–1198. Available at: http://doi.wiley.com/10.1002/jor.21373.

Kärrholm, J., Gill, R.H.S. & Valstar, E.R., 2006. The history and future of radiostereometric analysis. *Clinical Orthopaedics and Related Research*, (448), pp.10–21.

Khamis, S. & Yizhar, Z., 2007. Effect of feet hyperpronation on pelvic alignment in a standing position. *Gait & Posture*, 25(1), pp.127–135.

Kido, M. et al., 2013a. Load response of the medial longitudinal arch in patients with fl atfoot

deformity : in vivo 3D study. *JCLB*, 28(5), pp.568–573. Available at: http://dx.doi.org/10.1016/j.clinbiomech.2013.04.004.

Kido, M. et al., 2013b. Load response of the medial longitudinal arch in patients with flatfoot deformity: In vivo 3D study. *Clinical Biomechanics*, 28(5), pp.568–573. Available at: http://dx.doi.org/10.1016/j.clinbiomech.2013.04.004.

Klop, A.C. et al., 2017. The effect of repeated freeze-thaw cycles on human muscle tissue visualized by postmortem computed tomography (PMCT). *Clinical Anatomy*, 30(6), pp.799–804.

Knight, R., 2015. The Joy of Walking. , 9, p.1.

Kohls-Gatzoulis, J. et al., 2004. Tibialis posterior dysfunction: a common and treatable cause of adult acquired flatfoot. *Bmj*, 329(7478), pp.1328–1333.

Kovaleski, J.E. et al., 2008. Stiffness of the Ankle Complex. *Journal of Athletic Training*, 43(3), pp.242–248.

Kreighbaum, E. & Barthels, K., 1981. *Biomechanics: A Qualitative Approach for Studying Human Movement*, Burgess Publishing Company.

Kulig, K. et al., 2011. Women With Posterior Tibial Tendon Dysfunction Have Diminished Ankle and Hip Muscle Performance. *Journal of Orthopaedic & Sports Physical Therapy*, 41(9), pp.687–694. Available at: http://www.jospt.org/doi/10.2519/jospt.2011.3427.

Leard Statistics, Testing for Sphericity: Mauchly's Test of Sphericity. Available at: https://statistics.laerd.com/statistical-guides/sphericity-statistical-guide.php [Accessed September 30, 2017].

Levangie, P. & Norkin, C., 2005. *Joint Structure & Function: A Comprehensive Analysis* 4th ed., United States of America: F.A. Davis Company.

Levene, H., 1960. *Contributions to Probability and Statistics*, CA: Stanford University Press.

Lever, C.J. & Hennessy, M.S., 2016. Adult flat foot deformity. *Orthopaedics and Trauma*, 30(1), pp.41–50. Available at: http://dx.doi.org/10.1016/j.mporth.2016.02.005.

Levinger, P. et al., 2010. A comparison of foot kinematics in people with normal- and flat-arched feet using the Oxford Foot Model. *Gait and Posture*, 32(4), pp.519–523.

Available at: http://dx.doi.org/10.1016/j.gaitpost.2010.07.013.

Lhoste-Trouilloud, A., 2012. The tibialis posterior tendon. *Journal of Ultrasound*, 15(1), pp.2–6. Available at: http://dx.doi.org/10.1016/j.jus.2012.02.001.

Liao, S. & Padera, T.P., 2013. Lymphatic Function and Immune Regulation in Health and Disease. , 11(3), pp.136–143.

Lin, Y.C. et al., 2015. Imaging of adult flatfoot: Correlation of radiographic measurements with MRI. *American Journal of Roentgenology*, 204(2), pp.354–359.

Little, R.J. et al., 2012. The Prevention and Treatment of Missing Data in Clinical Trials. *The New England Journal of Medicine, Special Report*, 367(14), pp.1355–1360.

Little, R.J. & Rubin, D.., 2014. *Statistical analysis with missing data*, New York: John Wiley & Sons.

Lotke, A., Abboud, J. & Ende, J., 2008. *Lippincott's Primary Care Orthopaedics*, Philadelphia: Lippincott Williams & Wilkins Health.

Marasovič, T., Cecič, M. & Zanchi, V., 2009. Analysis and interpretation of ground reaction forces in normal gait. *WSEAS Transactions on Systems*, 8(9), pp.1105–1114.

Marron, M.M. & Wahed, A.S., 2016. Teaching Missing Data Methodology to Undergraduates Using a Group-Based Project Within a Six-Week Summer Program. *Journal of Statistics Education*, 24(1), pp.8–15.

Mitchell, L.C.J. et al., 2008. Medial Foot Loading on Ankle and Knee Biomechanics. *North American journal of sports physical therapy: NAJSPT*, 3(3), pp.133–140. Available at: http://www.ncbi.nlm.nih.gov/pubmed/20379384%5Cnhttp://www.pubmedcentral.nih.gov/articlerender.fcgi?artid=PMC2850544.

Mooi, E. & Sarstedt, M., 2011. *A Concise Guide to Market Research*, Berlin-Hiedelberg: Springer-Verlag.

Morgan, T.M. & Case, L.D., 2013. Conservative Sample Size Determination for Repeated Measures Analysis of Covariance. *Annals of Biometrics & Biostatistics*, 1(1002), pp.1–6.

Nallamshetty, L. et al., 2005. Evaluation of posterior tibial pathology: Comparison of sonography and MR imaging. *Skeletal Radiology*, 34(7), pp.375–380.

National Institute of Standards and Technology: U.S. Department of Commerce, Engineering Statistics Handbook. Available at: http://www.itl.nist.gov/div898/handbook/eda/section3/eda35a.htm [Accessed October 1, 2017].

Neville, C., Flemister, A.S. & Houck, J.R., 2010. NIH Public Access. *Foot Ankle Int*, 31(4), pp.320–328.

Novacheck, T., 1998. The biomechanics of running. *Gait and Posture*, 7, pp.77–95.

NPD Group: National Foot Health Assessment, 2012. National Foot Health Assessment 2012. Available at: http://www.ipfh.org/images/research_materials/2012_National_Foot_Health_Assessment_June_2012.pdf.

Oh, I.C. et al., 2016. Spring Ligament Tear Decreases the Ankle and Talonavicular Joint Reaction Forces: Biomechanical Study of the Tibiocalcaneonavicular Ligament Reconstruction. , pp.1–2.

Özkaya, N. et al., 2012. Degree of Freedom. In *Fundamentals of Biomechanics*. New York: Springer-Verlag, p. 224.

Patterson, R.M. et al., 2003. FOOT / ANKLE KINEMATICS : COMPARATIVE ANALYSIS OF NORMAL FOOT VS . FLAT FOOT DEFORMITY Department of Orthopaedics and Rehabilitation Orthopaedic Biomechanics Laboratory The University of Texas Medical Branch at Galveston Galveston , Texas.

Peck, R., Olsen, C. & Devore, J.L., 2016. *Introduction to Statistics and Data Analysis* 5th ed., Boston: Cengage Learning.

Perry, J., 2002. Orthotics & Prosthetics Virtual Library Project. In *Atlas of Limb Prosthetics: Surgical, Prosthetic, and Rehabilitation Principles*. pp. 1–14.

Petersen, W. et al., 2013. Treatment of acute ankle ligament injuries: A systematic review. *Archives of Orthopaedic and Trauma Surgery*, 133(8), pp.1129–1141.

Pinney, S.J. & Lin, S.S., 2006. Current Concept Review: Acquired Adult Flatfoot Deformity. *Foot & Ankle International*, 27(1), pp.66–75. Available at:

http://journals.sagepub.com/doi/10.1177/107110070602700113.

Provenzano, P.P. et al., 2002. Subfailure damage in ligament: a structural and cellular evaluation. *Journal of applied physiology (Bethesda, Md. : 1985)*, 92(1), pp.362–71. Available at: http://www.ncbi.nlm.nih.gov/pubmed/11744679.

Raikin, S.M., Winters, B.S. & Daniel, J.N., 2012. The RAM Classification. A Novel, Systematic Approach to the Adult-Acquired Flatfoot. *Foot and Ankle Clinics*, 17(2), pp.169–181.

Raj, M. & Bhimji, S., 2017. Pes Planus. *StatPearls*, pp.1–4. Available at: http://www.ncbi.nlm.nih.gov/pubmed/28613553.

Rao, S., Riskowski, J. & Hannan, M., 2013. Musculoskeletal Conditions of the Foot and Ankle: Assessments and Treatment Options. , 26(3), pp.345–368.

Ren, L. et al., 2008. A Phase-Dependent Hypothesis for Locomotor Functions of Human Foot Complex. *Journal of Bionic Engineering*, 5(3), pp.175–180.

Resende, R. et al., 2015. Increased unilateral foot pronation affects lower limbs and pelvic biomechanics during walking. *Gait & Posture*, 41(2), pp.395–401.

Resnick, R., Melvin, J. & Choueka, J., 1995. Deltoid ligament forces after tibialis posterior tendon rupture: effects of triple arthrodesis and calcaneal displacement osteotomies. *Foot & Ankle International*, 16(1), pp.14–20.

Richie, D.H., 2007. Biomechanics and Clinical Analysis of??the Adult Acquired Flatfoot. *Clinics in Podiatric Medicine and Surgery*, 24(4), pp.617–644.

Robi, K. et al., 2013. The Physiology of Sports Injuries and Repair Processes. In *Current Issues in Sports and Exercise Medicine*. Intech, pp. 43–77.

Scott, S.H. & Winter, D.A., 1993. Biomechanical model of the human foot: Kinematics and kinetics during the stance phase of walking. *Journal of Biomechanics*, 26(9), pp.1091–1104.

Sellman, J., 1994. Plantar Fascia Rupture Associated with Corticosteroid Injection. *Foot & Ankle International*, 15(7), pp.376–381.

Shanb, A.A. & Youssef, E.F., 2014. The impact of adding weight-bearing exercise versus

nonweight bearing programs to the medical treatment of elderly patients with osteoporosis. *Journal of family & community medicine*, 21(3), pp.176–81. Available at: http://www.ncbi.nlm.nih.gov/pubmed/25374469%0Ahttp://www.pubmedcentral.nih.gov/articlerender.fcgi?artid=PMC4214007.

Sharir, A., Barak, M.M. & Shahar, R., 2008. Whole bone mechanics and mechanical testing. *Veterinary Journal*, 177(1), pp.8–17.

Singh, V., Rana, R.K. & Singhal, R., 2013. Analysis of repeated measurement data in the clinical trials. *J Ayurveda Integr Med.*, 4(2), pp.77–81.

Smith, J.T. & Bluman, E.M., 2012. Update on Stage IV Acquired Adult Flatfoot Disorder. When the Deltoid Ligament Becomes Dysfunctional. *Foot and Ankle Clinics*, 17(2), pp.351–360. Available at: http://dx.doi.org/10.1016/j.fcl.2012.03.011.

Smyth, N.A. et al., 2017. Adult-acquired flatfoot deformity. *European Journal of Orthopaedic Surgery and Traumatology*, 27(4), pp.433–439.

Snell, R.S., 2011. *Clincal Anatomy by Regions* 9th ed., Baltimore: Lippincott Williams & Wilkins Health.

Tashman, S. & Anderst, W., 2003. In-vivo measurement of dynamic joint motion using high speed biplane radiography and CT: application to canine ACL deficiency. *J Biomech Eng*, 125(2), pp.238–245.

Teichtahl, A.J. et al., 2015. Wolff ' s law in action : a mechanism for early knee osteoarthritis. *Arthritis Research & Therapy*, pp.1–9. Available at: http://dx.doi.org/10.1186/s13075-015-0738-7.

The University of Auckland, 2015. The Response of Viscoelastic Materials. In *Solid Mechanics Part I [ebook]*. Auckland: The University of Auckland: Engineering Open Source Books, pp. 285–288. Available at: http://homepages.engineering.auckland.ac.nz/~pkel015/SolidMechanicsBooks/Part_I/BookSM_Part_I/10_Viscoelasticity/10_Viscoelasticity_01_Intro.pdf.

Toullec, E., 2015. Adult flatfoot. *Orthopaedics & Traumatology: Surgery & Research*, 101(1), pp.S11–S17. Available at: http://dx.doi.org/10.1016/j.otsr.2014.07.030.

Trnka, H.-J., 2004. Dysfunction of the tendon of tibialis posterior. *The Journal of Bone and Joint Surgery*, 86(7), pp.939–946. Available at: http://www.bjj.boneandjoint.org.uk/cgi/doi/10.1302/0301-620X.86B7.15084.

US Census Bureau, 2017. International Data Base: World Population. , 2017, pp.9–10. Available at: http://www.census.gov/population/international/data/idb/worldpopgraph.php.

Van den berg, R., 2017. How to Get (Partial) Eta Squared from SPSS? *SPSS Tutorials*. Available at: https://www.spss-tutorials.com/spss-partial-eta-squared/ [Accessed September 28, 2017].

Vulcano, E., Deland, J.T. & Ellis, S.J., 2013. Approach and treatment of the adult acquired flatfoot deformity. *Current Reviews in Musculoskeletal Medicine*, 6(4), pp.294–303.

Watson, P., 2017. Rules of thumb on magnitudes of effect sizes. *MRC Cognition and Brain Sciences Unit*. Available at: http://imaging.mrc-cbu.cam.ac.uk/statswiki/FAQ/effectSize [Accessed September 28, 2017].

Williams, G. et al., 2014. Could Failure of the Spring Ligament Complex Be the Driving Force behind the Development of the Adult Flatfoot Deformity? *Journal of Foot and Ankle Surgery*, 53(2), pp.152–155. Available at: http://dx.doi.org/10.1053/j.jfas.2013.12.011.

Williamson, E.R.C. et al., 2014. New Radiographic Parameter Assessing Hindfoot Alignment in Stage II Adult-Acquired Flatfoot Deformity. *Foot & ankle international*, p.1071100714558846. Available at: http://fai.sagepub.com/content/early/2014/11/06/1071100714558846.full.

Wolff, J., 1986. *The Law of Bone Remodeling*, Berlin, Germany: Springer-Verlag.

Woolston, B.C., 2017. Exercise and Osteoporosis : How to Strengthen Weak Bones. *HealthDay: Exercise & Fitness Health Library*, pp.10–12.

Xin, Z., 2014. *Development of an Integrated System for Human Spine Deformity Measurement*. National University of Singapore. Available at: http://scholarbank.nus.sg/bitstream/handle/10635/119263/Thesis_ZhengXin_HT090563Y.pdf?sequence=2.

Xu, R. & Wunsch, D.C., 2010. Clustering algorithms in biomedical research: a review. *IEEE Reviews in Biomedical Engineering*, 3, pp.120–154.

Yeap, J.S., Singh, D. & Birch, R., 2001. Tibialis posterior tendon dysfunction: a primary or secondary problem? *Foot & Ankle International*, 22(1), pp.51–55.

Yi, J., 2016. The effects of increased unilateral and bilateral calcaneal eversion on pelvic and trunk alignment in standing position. *Physical Therapy Rehabilitation Science*, 5, pp.84–88.

Zhang, Y. et al., 2015. Clinical Biomechanics Correlation between hindfoot joint three-dimensional kinematics and the changes of the medial arch angle in stage II posterior tibial tendon dysfunction fl atfoot ☆. *JCLB*, 30(2), pp.153–158. Available at: http://dx.doi.org/10.1016/j.clinbiomech.2014.12.007.

Zhao, W., Zou, W. & Chen, J.J., 2014. Topic modeling for cluster analysis of largebiological and medical datasets. *BMC Bioinformatics*, 15(Suppl 11: S11), pp.1–11.

Zhou, H. et al., 2017. Biomechanical Analysis of Cuboid Osteotomy Lateral Column Lengthening for Stage II B Adult-Acquired Flatfoot Deformity: A Cadaveric Study. *BioMed Research International*, 2017(Apr 10.).

APPENDICES

APPENDIX A – Ethics Approval Letter

APPENDIX B – Full Base Pillar RSA Frame CAD Drawing

APPENDIX C– RSA Frame Calibration Rods CAD Drawing

APPENDIX D – Base Pillar X-Ray Cassette Mounting Bar CAD Drawing

APPENDIX E – Specimen Preparation-Potting Protocol

APPENDIX F – Hexapod Control Protocol for Foot & Ankle Testing

APPENDIX G – Ligament Strain Response at Each Loadstep (Box and Whisper Plots)

APPENDIX H – Cadaveric Specimen Demographic Data

APPENDIX A – Ethics Approval Letter

Office for Research
Flinders Medical Centre / Ward 6C Room 6A219
Flinders Drive, Bedford Park SA 5042
Tel: (08) 8204 6453
E: Health.SALHNOfficeforResearch@sa.gov.au

Government of South Australia
SA Health
Southern Adelaide Local Health Network

Dr John Costi
School of Computer Science, Engineering and Mathematics
Flinders University
GPO Box 2100
ADELAIDE SA 5001

13 October 2017

RE: SAC HREC ethics application approval: Biomechanical involvement of the ankle's medial column ligaments: flatfoot deformity

To whom it may concern

The Low and Negligible risk application form submitted to the SAC HREC was reviewed and approved on the 17 August 2017.

Please retain this letter for your records, and a formal approval letter will follow in due course.

Kind regards

Petrina Kasperski
Executive Officer, SAC HREC

APPENDIX B – Full Base Pillar RSA Frame CAD Drawing

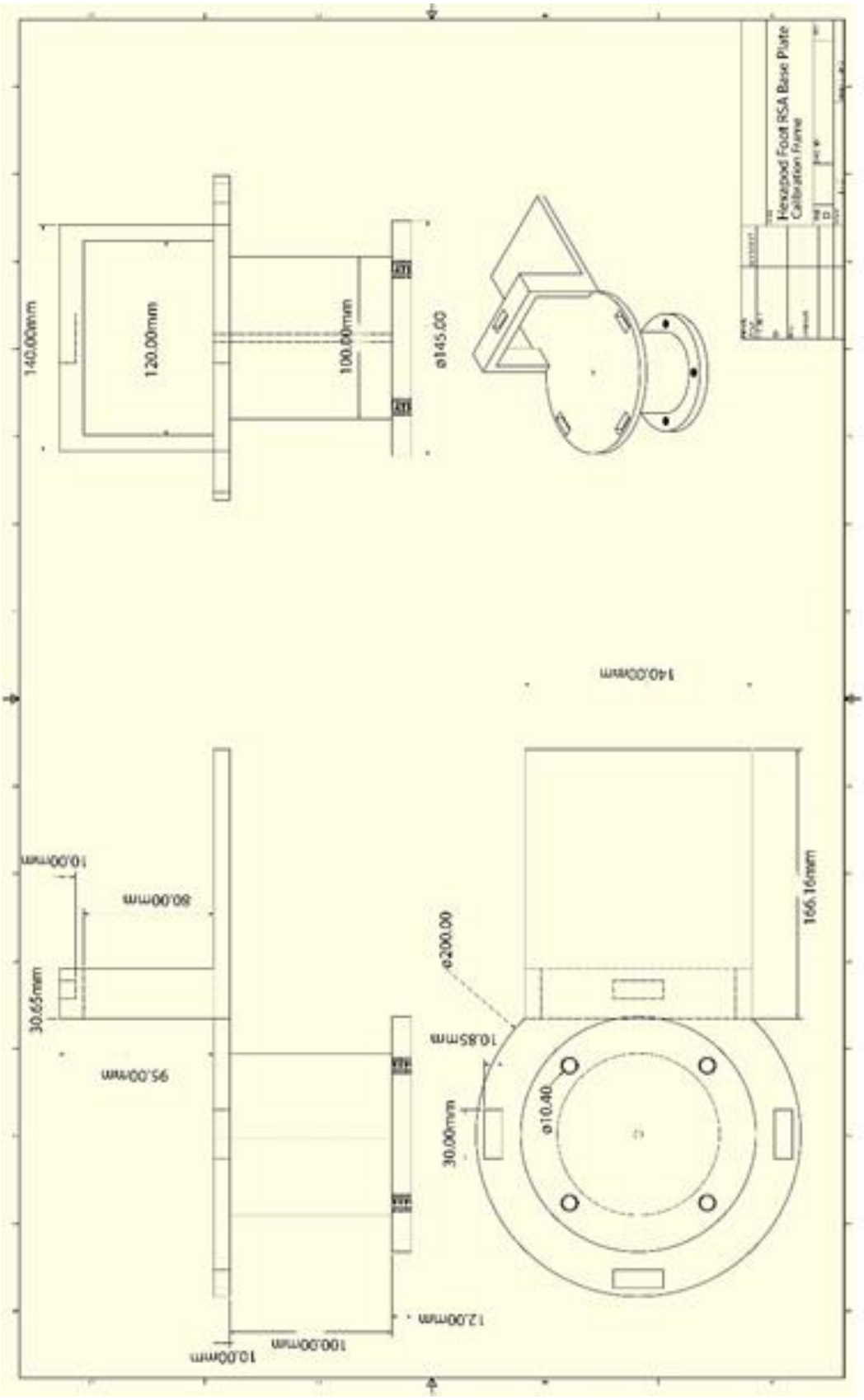

APPENDIX C –RSA Frame Calibration Rods CAD Drawing

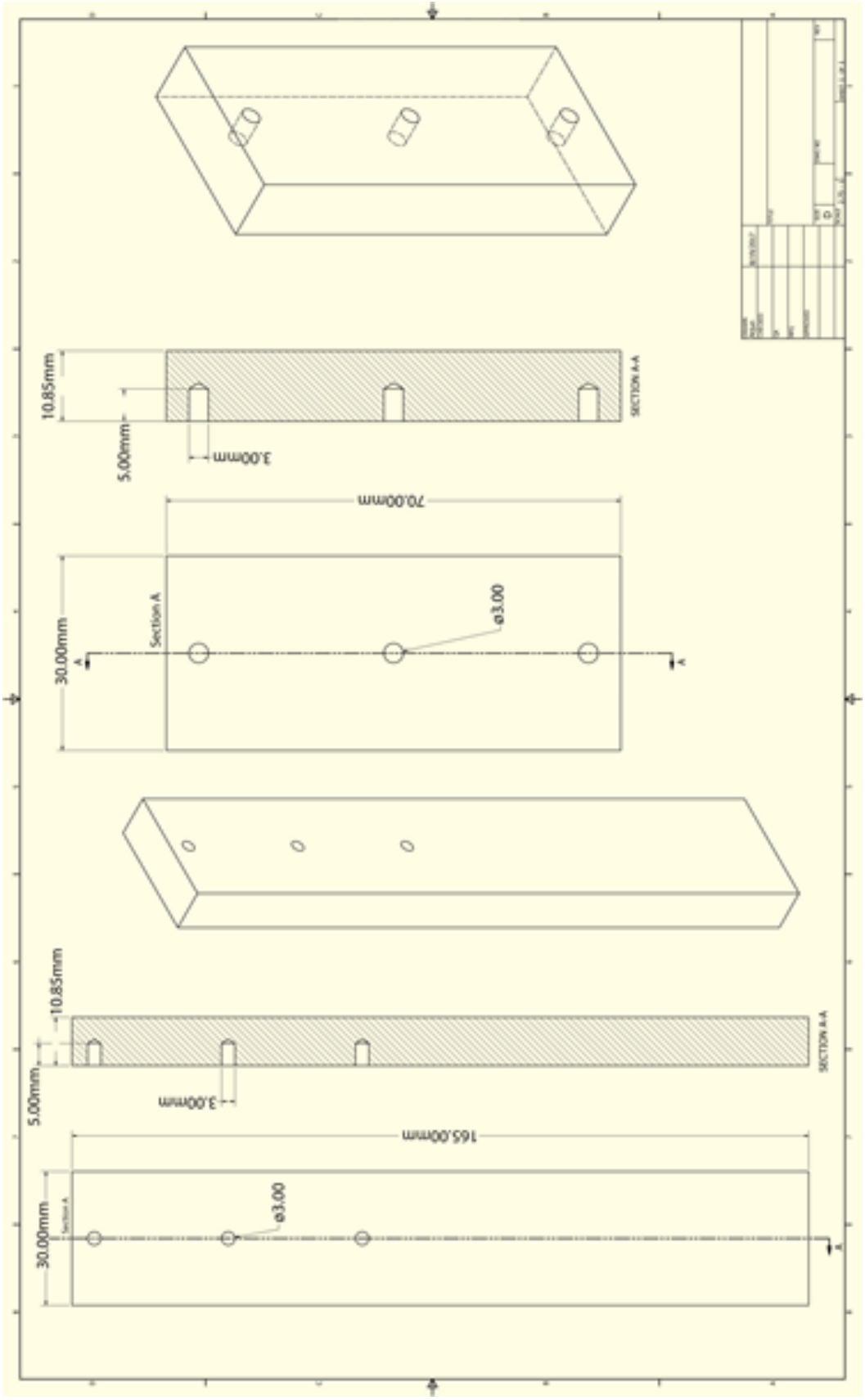

APPENDIX D – Base Pillar X-Ray Cassette Mounting bar CAD Drawing

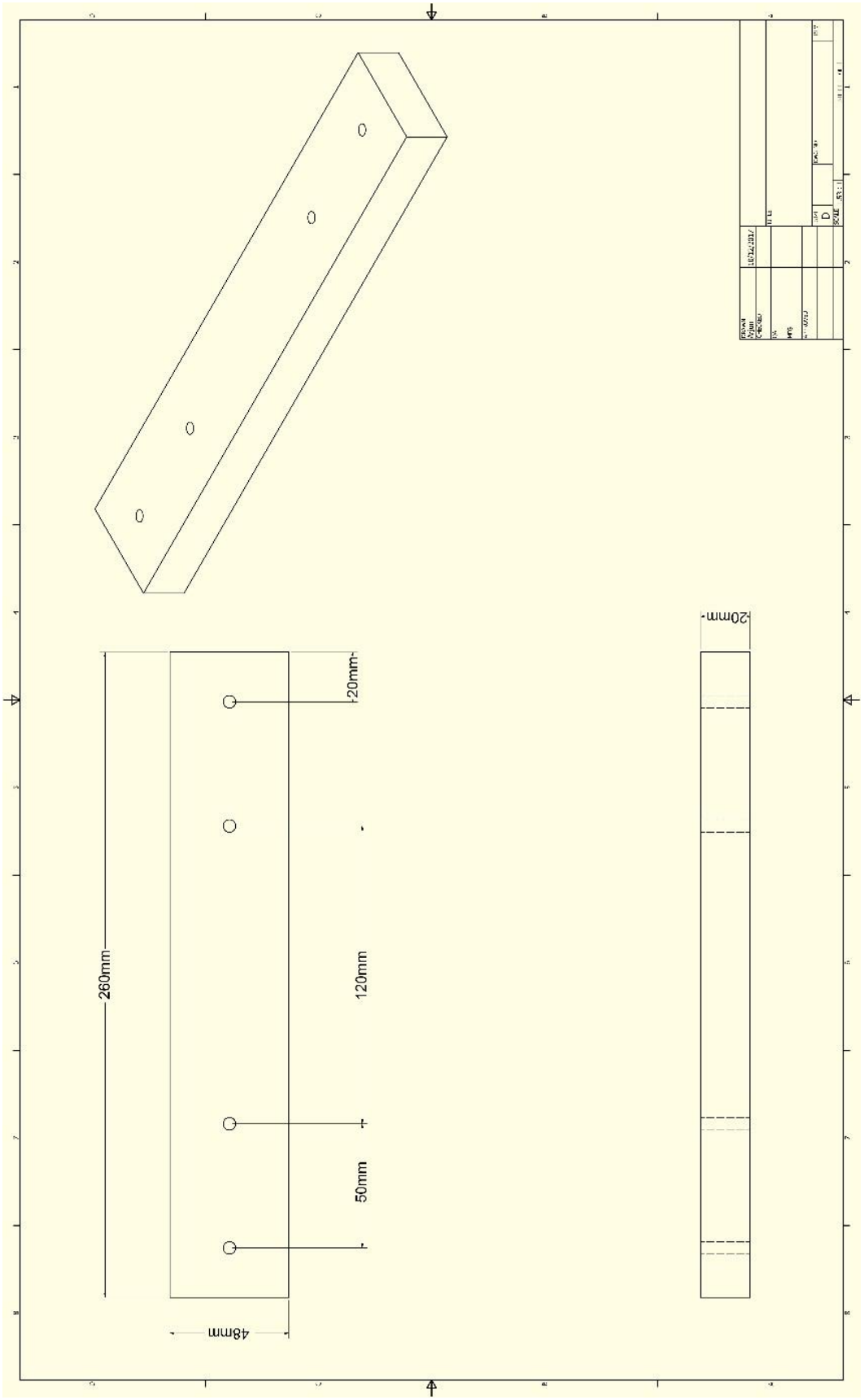

APPENDIX E – Specimen Preparation-Potting Protocol

Preparation

1. ☐ Ensure all the above items are present, as well as a thin plate to lay at the bottom of the cup prior to potting.
2. ☐ Insert a thin aluminium plate/circle into the bottom of the cup, so the PMMA is easier to knock out from the top hole when de-potting the specimen.
3. ☐ Cover the base with Kapton tape (heat resistant, 280C). Also tape the holes that won't be used (makes removal easier). *Remember to clean attaching surface properly with alcohol*
4. ☐ Grease the bolts and lightly thread them into the holes.

Potting

1. Ensure all soft tissue is off the proximal end of tibia & fibula using a scalpel. Ensure there is enough bone exposed to fit within the top cup (30-40mm).
2. Move specimen to the Fume hood. Ensure the top cup and alignment rig are in the fume hood, ready for potting with PMMA. Also need 2 retort stands with clamps to hold the foot in the correct alignment when potting.
3. For PMMA potting: Need PMMA powder, Monomer agent, measuring cups, mixing cup, and mixing tool.
4. Check alignment of the top cup with the top of the coupling plate. Invert the cup and attach to the top cup coupling plate. Attach the plate to the alignment rig base with the central screw holes facing towards the back.
5. Attach bottom cup with plate to rig base. Make sure it is aligned correctly. *There is only way to fix the bottom cup to the alignment plate so there is no chance of wrong orientation.*
6. Invert the specimen and place the proximal tibia into the top cup. Make sure the tibia & centre of rotation of the ankle joint is lined up with the centre of the top cup.
7. Ensure the Specimen is not rotated and make sure the forefoot is positioned forward, with the back of the heel (Achilles tendon) lined up vertically with the back screw of the top cup. Is the back of the Achilles lined up with the back screw? Is the forefoot positioned directly forward? Is the tibia & ankle joint lined up with the centre of the top cup? (with the foot flat).
8. Use one retort stand to hold the tibia in place (centrally with the middle of the cup)
9. Use another retort stand to hold the forefoot flat. (*Refer to diagram).*

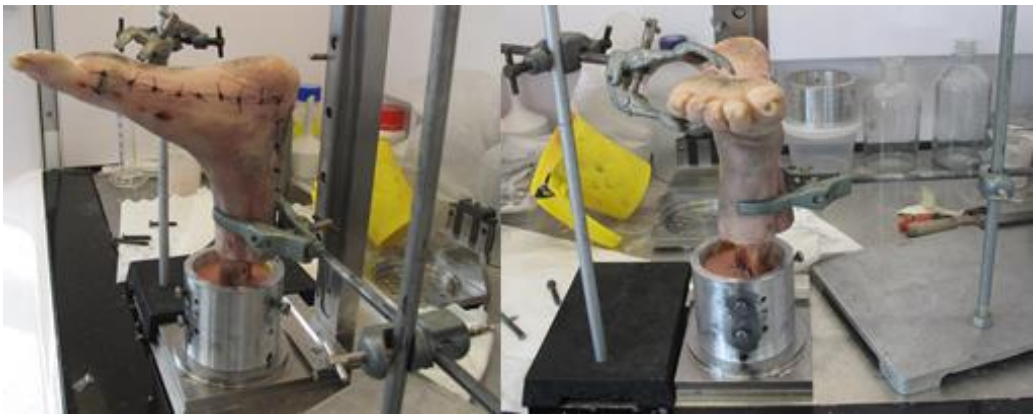

10. Mix PMMA at a ratio of: 2.5 mL Powder to 1 mL liquid. Make sure it is liquidy in nature. To accomplish the liquidy feel of PMMA add about 5 mL more of liquid to the mixture.

Top Cup: Volume→ ~(pi x r^2 x Depth) = _____mL;
Therefore Ratio → ((2.5/3.5) x volume) Powder & Volume mL – Powder mL of liquid
For the large top cups, shown in diagram: 220mL Powder to 88.36mL Liquid

11. Pour PMMA into the top cup. **Make sure PMMA covers the screws. Continuously pour the PMMA or the PMMA will not harden as a whole unit.**
12. Allow PMMA to harden for about 15-20 minutes.
13. *When top cup is potted, Need to take offsets for IAR calculation & and record them on data sheet. (X-Ray)*
14. Detach top cup from rig base
15. Return back to Biomechanics Facility.
16. Take X-Rays to measure offsets (with a metal strip of known length for calibration (30mm aluminium piece)). *Record on Axis Offset Sheet - Attached*

Take a Lateral X-Ray to find the Z-offset and Y-offset
Take an AP X-Ray to measure the X-Offset *(if ankle joint is centrally aligned when potting, the Y offset should be should be very close to 0).*

17. Hook Load Cell to the Achilles tendon Sutured Hook
18. Connect the Load Cell to the Data Acquisition System and monitor the Force (Tension)
19. With wire, pull to a tension of ~150N and firmly wrap the wire around the top cup bolt to maintain tension.
20. Attach the RSA Base Pillar for Foot & Ankle testing.
21. Mount Specimen to Hexapod.

Unpotting

1. Remove the Screws from the Top cup
2. With one person holding on to the potted specimen and the top cup, hit out the PMMA from the top cup using a pin punch and hammer (until PMMA lifts away from the top cup)
3. Once the PMMA is remove from the top cup, remove the PMMA from the Specimen. This is best done using the clamp on the bench top and a hammer to cause cracks in the PMMA. Crack PMMA and remove with Pliers
4. Clean the top cup thoroughly with alcohol.

APPENDIX F– Hexapod Control Protocol for Foot & Ankle Testing

STEP 1: Setting up Hexapod and VI

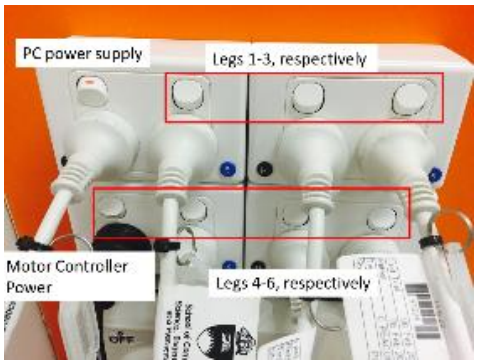

1. Check if all power points are switched off
2. Check if door is closed.
3. Power on Lab Host PC
4. Switch on the 7 power switches:
   4.1. Bottom left power point (Motor Controller)
   4.2. 6 power points for the actuators/legs
5. Walk to hexapod and check:
   5.1. Red light on each of the actuator arms
   5.2. Each actuator motion controller has one green light on
   5.3. Real Time Controller & Load Cell amplifier lights all turn on
6. Logon to the PC
7. Open LabVIEW 2013
   7.1. Select **'Biomechanics-lab-hexapod.lvproj'** (pinned to the top)

Select File → Recent Projects → "Biomechanics-lab-hexapod.lvproj" to open the hexapod project. If project is not there: File→Open→Drive:D→Portable Hexapod→Host Target→Biomechanics-lab-hexapod

   7.2. In the project explorer window, Under 'My Computer' (this is the Host Computer VI/GUI Computer)
      7.2.1. Open **'host-computer_Dhara_VI.vi'**
   7.3. In the project explorer window, Under Hexapod PXI (this is the real time system)
      7.3.1. Open **'Hexapod_Dhara_VI.vi'**.

Run Host Computer VI

1. On the Host Computer VI, click the white arrow button in the top left corner (series of files will load). White Arrow will turn black once system files have loaded.

Run Real Time VI

1. On the Hexapod VI, click the same 'Run' button in the top left corner.
2. Wait until Real Time VI comes online – Force and moment graphs should be smooth and reading some forces and moments.

3. **IF** mode home/ jogging/ joint space/ kinematics/ load control are enabled >> encoders are very sensitive and it is dangerous to work within the hexapod.

Enable Soloist Controllers

1. On the Host Computer VI, Under Soloist Controller, Click "enable" (Top left corner of GUI)
2. Watch the 2nd light appear on each soloist controller (Six soloist controllers) - CHECK

MODE 1: Home – H*exapod moves into home position: Calibration for each leg, finds leg length, origin of counts (initial values) & incremental encoder so that the hexapod is aware of its absolute position.*

Real Time VI

1. Enable home mode
2. Select home-tab (Other modes disabled)

   2.1. Click *start homing* (Hexapod starts homing each leg from 1 to 6; where leg number 6 is represented by the purple line. Homing is finished when the graph is stable, home index shows 2 last lights on green)

Watch end of homing for each leg on the leg command graph. **If** no steady state at about -6000 is reached quickly, quickly disable process by clicking ***stop motion*** button.

3. Disable home-mode by clicking home-button

MODE 2: Joint Space

Levels the top plate and moves it back to the centre

Real Time VI

1. Enable joint-space mode
2. Click the joint-space tab
3. Click level-the-top-plate
4. Click move-to-center
5. Click start-ramp (bottom left corner)

Watch the graphs – the leg motions command should approach zero

6. Disable the 2 buttons (level-the-top-plate & move-to center)
7. Disable Joint space mode

Note: The graphs will change again due to motor friction

MODE 3: Level Load Cell

Zeros the load cell

Real Time VI

1. On the hexapod VI – top middle under general settings
2. Enable 'Zero load cell' button.

Watch the forces approach zero.

STEP 2: Setting Data Path

Use Host Computer VI

Under General Settings, set the:

Specimen Axis Offset

Take an AP X-Ray to find the X offset (with a metal strip of known length for calibration)

Take a Lateral X-Ray to find the Y offset (if ankle joint is centrally aligned when potted, should be very close to 0).

Z Offset also found from the Lateral X-Ray.

Data Saving Path

a. D:\data\Arj\FS**XX**\FS**XX**_loadstep**N**_P.txt
b. D:\data\Arj\FS**XX**\FS**XX**_loadstep**N**_L.txt

Where **XX** refers to the specimen number being tested, and **N** refers to the load step being applied (rename with new load step for each load being tested).

Click 'Upload to Hexapod VI'

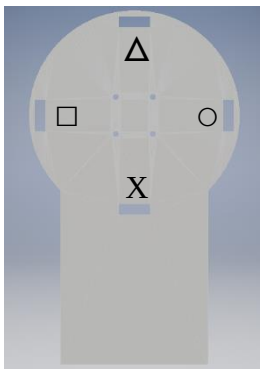

STEP 3: Mount the Base Pillar & Specimen to hexapod

Attaching the Base Pillar to the Hexapod

1. Attach the Radiopaque Base pillar to the hexapod with the correct orientation & Calibration Rods in their corresponding location (*Refer to diagram)*
2. Screw in four M10 socket head screws into the bottom of the pillar (using an 8mm allen key).

Attaching the Specimen Coupling Plate to the Specimen (Top Cup) **Front of**

3. Put the specimen into the hexapod (carefully from the side – *Do not touch the encoders*).
4. Place specimen on the base plate and roughly align top cup holes with the top plate (still up).
5. Lower the Specimen Coupling Plate (Slowly).
6. Bring the top cup of the specimen to the Specimen Coupling plate.
7. Insert four M6 countersunk socket head screws into the top cup.
8. Push the Specimen Coupling plate (attached to specimen) up towards the Load Cell Plate.
9. Insert four M8 socket head screws through the specimen coupling plate to the load cell plate.
10. Foot should be 'hanging' slightly. Need to ***Jog*** downwards until some force is seen (~-20N).

Jogging the Hexapod

Lowers the Specimen Coupling Plate so the specimen is on the base pillar.

Hexapod Real Time VI

1. Select jogging-tab- check that nothing is enabled
2. Enable axis jogging
3. Enable axis jogging

3.1. Choose axis (to jog down, select 3 (Tz)

1	Tx	2	Ty	3	Tz
4	Rx	5	Ry	6	Rz

3.2. Using the jogging bar:

Click and hold it to change speed (counts/ half a micron per second) or

Click once and maintain speed

Press STOP-BUTTON to stop motion

Negative (left) is down

Positive (right) is up

4. Move (jog) downwards until the foot just touches the base plate & hexapod hits 0 force (go up until ~20N), then stop. (Slowly – **DO NOT** hit anything at speed!).

Use a speed of -600 at first, then drop down to -200 as it gets closer, and then stop jogging once specimen touches base pillar (Forces ~20N).

5. Disable axis-jogging-button/disable jogging mode.

SCREWS CAN BE ADJUSTED/HANDS IN HEXAPOD

6. Check Normal Foot alignment.
7. **Place the 2 Cassette Holders on the Cassette Holder Bar!**
8. Ready to Begin Load Step.

STEP 4: Load Control

1. Check Offsets are entered correctly. (Entered in both Specimen Axis Offset **AND** Extension Specimen Offset)
2. ***Double Check Data Path is set.***

Data Saving Path

a. D:\data\Arj\FS**XX**\FS**XX**_**loadstepN**_P.txt

b. D:\data\Arj\FS**XX**\FS**XX**_**loadstepN**_L.txt

3. In the Host VI click '**Upload to Hexapod VI**'

In the Hexapod Real Time VI

4. Set Sample number to a very large arbitrary number (5 000 000 000)
5. **Set sampling frequency** to: Sample Rate (Hz) = 100, time (s) = 60
6. Select the Load-Control tab
7. **Testing Axis**: Set to **Primary Axis only** (Should be default)
8. **Primary Axis:** Set to **2**, **Secondary Axis:** Set to **2**
9. Constrain Rx, Ry and Rz (Enable last 3 constrain-buttons) (*Doesn't need to be any rotation externally applied to the tibia*)
10. **Set Specimen Stiffness:**

75	75	800	15	15	15

11. Enable Load Control mode (outside the tab).

Real Time Graphs

Red	My Fy
Green	Mz Fz
White	Mx Fx

Simulating Acquired Flatfoot Deformity in Load Control

STEP 5: Simulating dorsiflexion

1. To apply 10 degrees of dorsiflexion, set the constrain values as:

0	0	0	- 10	0	0

2. Hexapod will begin to move, applying 10 degrees of dorsiflexion to the foot.

STEP 6: Applying Load to Dorsiflexed foot

1. Enable Load-Control button within the load control tab (to transition to force targeting. Target force is set to initial force)
2. Begin initial load step – 100N

Set Absolute Forces and Moments Command

0	0	-100	0	0	0
Fx	Fy	Fz	Mx	My	Mz

3. **Click 'Collecting' button**. **(CHECK Button has been clicked!)**
4. Click Start Ramp in the bottom left hand corner
5. The forces will approach the entered load. Watch the specimen position in the bottom of the tab.
6. Once forces have reached its value (100N), wait for data 'Collection' button to complete (go off).
7. Once Collecting light is off, Press 'Read Raw Data' and 'Output Data'.
8. Disable load control mode
    1. Un-Click Load Control button inside the tab
    2. Un-Click Load Control button outside the tab
9. **Take 2 X-Rays** - **Left & Right** (for RadioStereometric Transformation)

STEP 7: Taking Stereometric X-Rays – X-Ray Positioning & Operation

X-Ray Positioning/Operation.

Green button enables translation along **Green Rail Track**

Blue button enables translation along **Blue Rail Track**

Purple button enables **rotational** adjustment of the X-Ray head

Black button enables angular adjustment of the X-Ray Collimator

Take Left X-Ray Image

1. Insert X-Ray cassette into the Right X-Ray Holder (Align the tape marker on the cassette with the cassette holder)

Right Cassette holder For left X-Ray image, Left Cassette holder for Right X-Ray image (with respect to the front of the hexapod)

2. Move the X-Ray head along the Green Rail (While holding the Green button)
3. Stop & align at the first tape marker on the Green rail.
4. Adjust the rotation of the X Ray head to align the tape marker lines together (While holding the purple button)
5. Adjust the X Ray Collimator Angle to 56° (While holding the black button)
6. Turn on the display light and ensure the light covers the X-Ray plate. Adjust the focus of the beam using the two knobs on either side of the X-Ray head such that the crosshairs are well aligned with the lines on the Cassette. This dictates the field of view on the X-Ray image.
7. Take the X-Ray image (Exit the room and close door)
8. Check image (14 beads visible & 12 Calibration beads)

Check carefully! It is likely that an actuators may block visibility of some beads.

If so, adjust the brightness & contrast and check if beads are somewhat identifiable/visible THROUGH the actuators). *These beads can be enhanced in Image Post Processing.*

9. If Okay – Save (put text on each X-Ray) and continue to take Right X-Ray.

(*LEFT Image: FS**XX**_loadstep**N**_L*)

(*Refer to X-Ray File naming convention below)*

Take Right X-Ray Image

1. Insert X-Ray cassette into the Left X-Ray Holder

(With respect to the front of the hexapod)

2. Reposition X Ray along the Green rail to the Right (Stop & align at the marked line)
3. Rotate X-Ray head counterclockwise and align marked vertical lines together
4. Adjust the X-Ray Collimator Angle to 56°
5. Turn on the display light and ensure the light covers the X-Ray plate with the crosshairs aligned with the plate
6. Take the X-Ray image (Exit the room and close door)
7. As for the Left image previously taken, Check the image (14 beads visible & 12 Calibration beads) (**May need to Adjust brightness to identify beads through actuators**)
8. If Okay – Save (*RIGHT Image: FS**XX**_loadstep**N**_R*)

(*Refer to X-Ray File naming convention below)*

X-Ray File Naming Convention

LEFT Image: FS**XX**_loadstep**N**_L

RIGHT Image: FS**XX**_loadstep**N**_R

Where **XX** refers to the specimen number being tested, and **N** refers to the load step being applied

9. Remove X-Ray Cassette from Base Pillar Cassette Holder.
10. Return to Hexapod Control

STEP 8: Applying Load to Dorsiflexed foot – Continue Hexapod Load Increments

First Load Step – 230N

1. **Change files names for new Load Step**

Data Saving Path

a. D:\data\Arj\FS**XX**\FS**XX_loadstepN**_P.txt

b. D:\data\Arj\FS**XX**\FS**XX_loadstepN**_L.txt

i.e for the first load step of 230N, rename the files by changing both data paths to:

(Example) Data Saving Path for Load Step of 230N

a. D:\data\Arj\FS**XX**\FS**XX_loadstep230**_P.txt

b. D:\data\Arj\FS**XX**\FS**XX_loadstep230**_L.txt

2. In the Host VI click '**Upload to Hexapod VI**'

3. **Check the forces –** ***Notice that the Fz force has reduced. (Need to bring the foot back to the last applied load first, and then increment to the new load).***

4. Select the Load Control tab

5. Enable the Load Control mode

6. Set the Load to the last applied load – (e.g. the initial load applied previously was 100N)

Set Absolute Forces and Moments Command

0	0	-100	0	0	0
Fx	Fy	Fz	Mx	My	Mz

7. Click Start Ramp in the bottom left hand corner

8. The forces will approach the entered load.

9. Once forces have reached its previous value (100N), we can now increase the load to the desired loadstep.

10. Set the Load to the desired load step – (Loadstep1: 230N)

Set Absolute Forces and Moments Command

0	0	-230	0	0	0
Fx	Fy	Fz	Mx	My	Mz

11. **Click 'Collecting' button on the right side of the Real Time VI. (CHECK Button has been clicked!)**

12. Click Start Ramp in the bottom left hand corner

13. The forces will approach the entered load. Watch the Real Time Force graph.

14. Once forces have reached its value (230N), wait for data 'Collection' button to complete (go off).
15. Once Collecting light is off, Press 'Read Raw Data' and 'Output Data'.
16. Disable load control mode
    a. Un-Click Load Control button inside the tab
    b. Un-Click Load Control button outside the tab
17. **Take 2 X-Rays - Left & Right** (for RadioStereometric Transformation)

As in STEP 7: Taking Stereometric X-Rays – X-Ray Positioning & Operation (Refer to *Page 5*)

STEP 9: Continuing Hexapod Load Increments (Repeat for all Incremental Load Steps)

Continue Applying Load Steps *(Loadstep 1: 230N, Loadstep 2: 460N, Loadstep 3: 690N, Loadstep 4: 920N)*

18. **Change files names for new Load Step**

Data Saving Path

19. D:\data\Arj\FS**XX**\FS**XX_loadstepN**_P.txt
20. D:\data\Arj\FS**XX**\FS**XX_loadstepN**_L.txt

*Where **XX** refers to the specimen number being tested, and **N** refers to the load step being applied (rename with new load step for each load being tested).*

21. In the Host VI click '**Upload to Hexapod VI**'
22. **Check the forces – *Notice that the Fz force has reduced. (Need to bring the foot back to the last applied load first, and then increment to the new load).***
23. Select the Load Control tab
24. Enable the Load Control mode
25. **Set the Load to the last applied load**

Set Absolute Forces and Moments Command

0	0	**(Last load)**	0	0	0
Fx	Fy	Fz	Mx	My	Mz

26. Click Start Ramp in the bottom left hand corner

27. The forces will approach the previous load (entered load).
28. Once forces have reached its previous value, we can now increase the load to the next loadstep.
29. Set the Load to the desired load step – (i.e. for Loadstep2, Fz = -460N)

Set Absolute Forces and Moments Command

0	0	**New Load**	0	0	0
Fx	Fy	Fz	Mx	My	Mz

30. **Click 'Collecting' button**. **(CHECK Button has been clicked!)**
31. Click Start Ramp in the bottom left hand corner
32. The forces will approach the entered load. Watch the Real Time Force graph.
33. Once forces have reached and steadied at this loadstep, wait for data 'Collection' button to complete (go off).
34. Once Collecting light is off, Press 'Read Raw Data' and 'Output Data'.
35. Disable load control mode
    a. Un-Click Load Control button inside the tab
    b. Un-Click Load Control button outside the tab
36. **Take 2 X-Rays** - **Left & Right** (for RadioStereometric Transformation)

As in STEP 7: Taking Stereometric X-Rays – X-Ray Positioning & Operation (Refer to *Page 5*)

Repeat for All incremental load steps (50 (initial), 230, 460, 690, 920) with X-Rays for each load step

37. Remove X-Ray Cassette from Base Pillar Cassette Holder.

38. Return to Hexapod Control

Step 11: Reduce Load to -50N

1. Once all tests are complete and data has been collected for each loadstep
2. Select the Load Control tab
3. Enable the Load Control mode outside the tab
4. Enable the load control button inside the tab
5. Set the Load to -50N

Set Absolute Forces and Moments Command

0	0	-50	0	0	0
Fx	Fy	Fz	Mx	My	Mz

6. Click Start Ramp in the bottom left hand corner
7. The forces will approach -50, some load will be taken off the specimen.
8. Once forces have reached -50, we can remove the dorsiflexion

Step 10: Remove Dorsiflexion from specimen

1. The Load-Control button within the load control tab should still be enabled
2. Remove dorsiflexion by changing the constrain value from -10 to 0

Constrain values should read:

0	0	0	0	0	0

3. Hexapod will move back to neutral vertical position

Step 11: Remove Loading from Specimen

9. Select the Load Control tab
10. Enable the Load Control mode
11. Set the Load to 0N

Set Absolute Forces and Moments Command

0	0	0	0	0	0
Fx	Fy	Fz	Mx	My	Mz

12. Click Start Ramp in the bottom left hand corner
13. The forces will approach 0, load will be taken off the specimen.
14. Once forces have reached 0, we can remove the specimen
15. Disable load control mode when ready to remove the specimen
    a. Un-Click load control in the tab
    b. Un- click load control outside of the tab

Step 12: Remove Specimen

16. Undo screws attaching the Specimen Coupling Plate and load cell plate
17. Enable jogging mode
    a. Enable axis jogging
    b. Jog up (Positive using a speed of 1000) (*Jog up until the white plugs are ~10mm above the housing - leg position should be around 630*)
    c. Undo screws attaching Specimen Coupling Plate to top cup
    d. Remove Specimen
    e. Push Specimen Coupling Plate back up to Load Cell Plate & Bolt in
    f. Jogging mode (axis: 3), go +Tz until one leg reaches 643
18. Follow **MODE 2: Joint Space** (*Centres in the global coordinate system*)

Joint Space

a. Enable joint-space mode
b. Within the joint-space tab, Enable the 2 buttons (level-the-top-plate & move-to-center)
c. Click Start Ramp
d. Disable the 2 buttons and joint space mode

Step 11: Logging off

1. Jogging all 6 legs to max length of 644 (upper limit 645)
2. Disable all modes
3. Stop Real Time VI: "VI Stop"
4. Stop Host VI: "Stop"
5. Exit LabVIEW (click OK when notification tells you it is disconnected and save whatever the program offers you)
6. Close both control tool windows
7. Copy test folder from desktop to C:data and USB-Stick
8. Switch off socket switches on the wall (6+1, right side of desk)
9. Switch off load cell amplifier
10. Log off computer

APPENDIX G –Ligament Strain Response at Each Loadstep (Box and Whisper Plots)

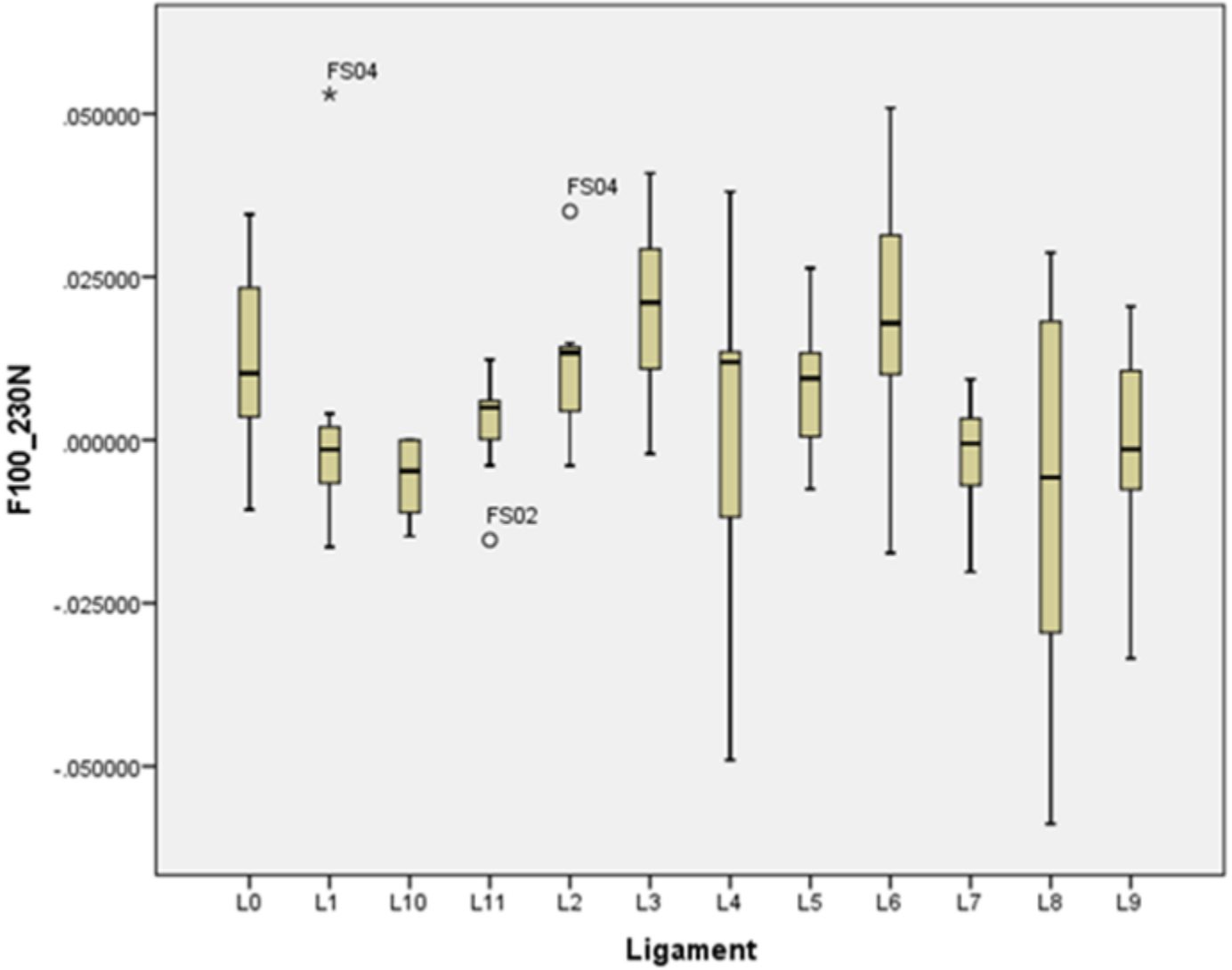

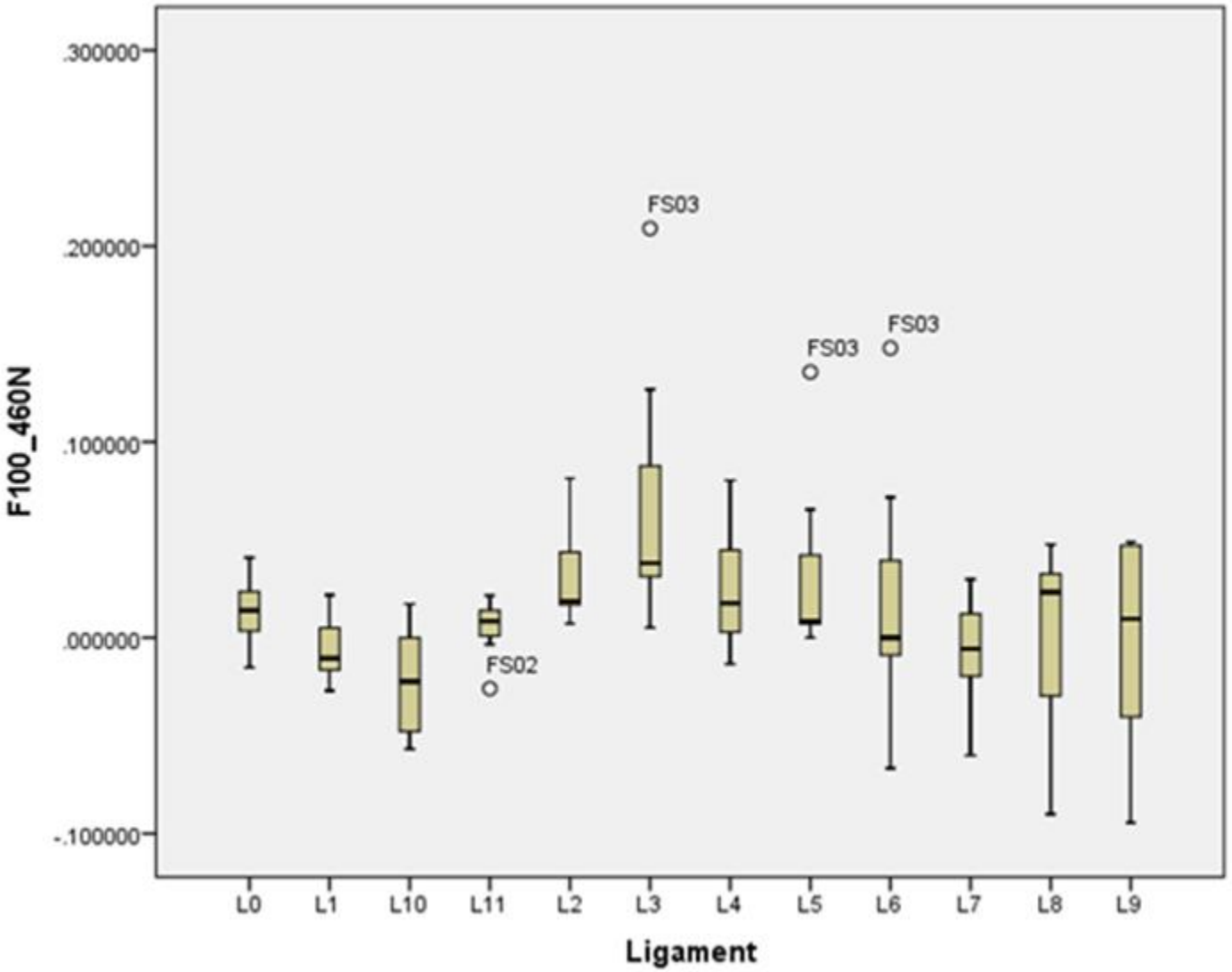
F100_460N
.300000
.200000
.100000
.000000
-.100000
FS03
FS03
FS03
FS02
L0
L1
L10
L11
L2
L3
L4
L5
L6
L7
L8
L9
Ligament

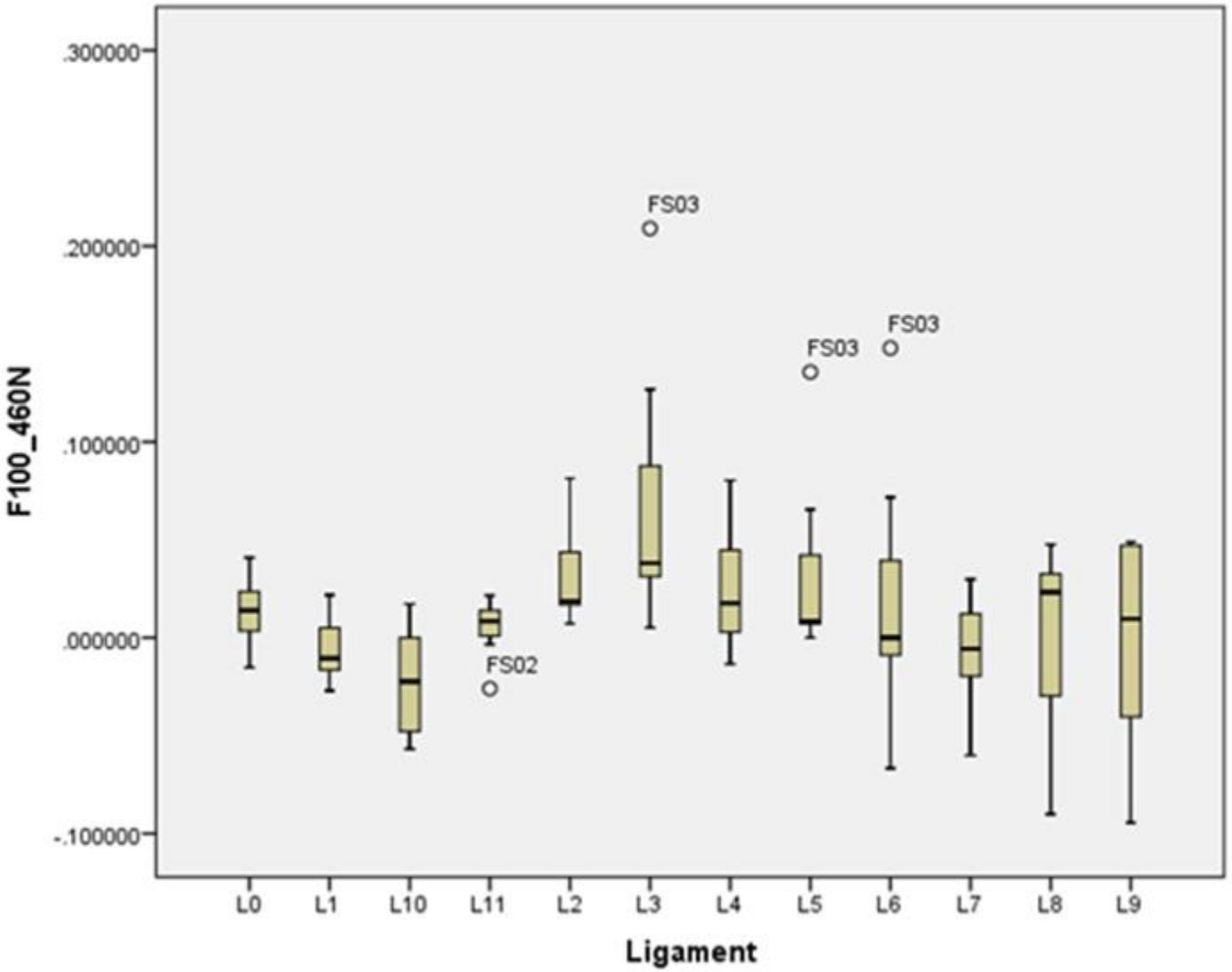
F100_460N
.300000
.200000
.100000
.000000
-.100000
FS03
FS03
FS03
FS02
L0
L1
L10
L11
L2
L3
L4
L5
L6
L7
L8
L9
Ligament

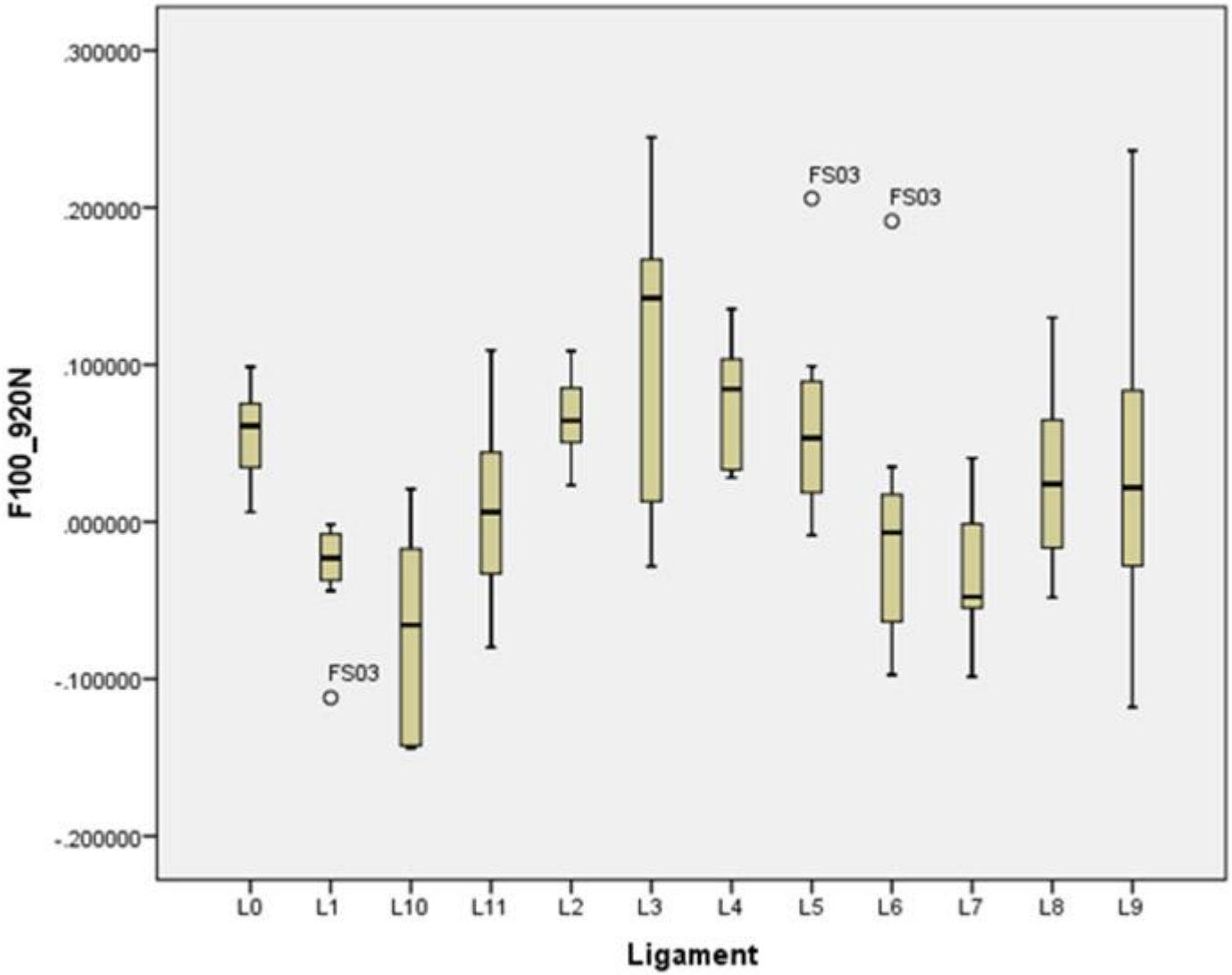
F100_920N
.300000
.200000
.100000
.000000
-.100000
-.200000
FS03
FS03
FS03
L0
L1
L10
L11
L2
L3
L4
L5
L6
L7
L8
L9
Ligament

APPENDIX H – Cadaveric Specimen Demographic Data

Cadaver Ankle Specimen List

SPECIMEN NO.	IDENTIFICATION	USE	CADAVERS:	
#	ID		11	(2 Pilot, 9 Test)

Specimen No.	Donor ID	Pilot/Study	Sex	Age	Height	Weight	BMI	Side	Notes
P1	GL1705913	Pilot Sim	Female	63	-	100	-	Left	-
P2	GL1403388	Pilot Sim	Female	80	-	70	-	Left	Large bunion surgery
FS00	GL1705848	Study	Female	67	65	204	33.9	Right	Sepsis
FS01	GL1705985	Study	Female	84	66	92	14.8	Right	Sepsis Gastroenteritis Chrohns Disease
FS02	GL1706052	Study	Female	80	66	150	24.2	Right	COD Unknown
FS03	GL1706060	Study	Male	58	73	195	25.7	Right	Sepsis. Lung Cancer sequela
FS04	GL1706203	Study	Male	62	70	235	33.7	Right	Stage 4 lung cancer sequela
FS05	GL1705980	Study	Female	77	64	145	24.9	Right	Lung Cancer - Bone Metastasis
FS06	GL1706352	Study	Male	74	69	190	28.1	Right	COD Unknown
FS07	GL1706339	Study	Male	65	69	149	22	Right	COD Unknown
FS08	GL1706362	Study	Male	58	65	110	18.3	Right	COD Unknown